UNIVERSITY OF TURKU

# Data Analysis for Emerging Materials in Hybrid Perovskite Photovoltaics

Department of Mechanical and Materials Engineering
Master of Science in Technology Thesis

Author:
Ruslan Hasanov

Supervisors:
Jovana V. Milić, Department of Chemistry
Mohammad Reza Golobostanfard, Department of Chemistry
Mahboubeh Hadadian, Department of Mechanical and Materials Engineering

04.07.2025
Turku

Master of Science in Technology thesis

**Subject**: Materials Engineering
**Author**: Ruslan Hasanov
**Title**: Data Analysis for Emerging Materials in Hybrid Perovskite Photovoltaics
**Supervisors**: Jovana V. Milić, Mohammad Reza Golobostanfard, Mahboubeh Hadadian.
**Number of pages**: 88 pages
**Date**: 04.07.2025

**Abstract**.

Perovskite solar cells have garnered significant attention in the field of photovoltaics due to their low production costs and high efficiency. Device instability and the transition to multi-pixel device configurations underscore the critical need for standardised high-throughput characterisation and robust data analysis. Currently, the lack of automated workflows for analysing large-scale and repetitive current-voltage measurements leads to inconsistencies and inefficiencies in data processing, hindering research progress.

This thesis addresses the gap by presenting an open-source Python-based analytical software tool that automates the analysis and reporting of current-voltage data from 2- and 8-pixel perovskite solar cell devices, allowing for standardised performance evaluation. The developed tool features input handling, automatic extraction of essential performance parameters, such as fill factor and power conversion efficiency, as well as the generation of plots and comprehensive PDF reports.

Applied to real experimental datasets, the software demonstrates its ability to process data from devices with both 2-pixel and 8-pixel configurations. The proposed solution is built with a modular design, which allows for the customisation and integration of functionalities to meet the evolving research demands. The tool provides reproducible, high-quality reports, significantly reducing manual workload. The structure of generated reports consists of the current density-voltage graphs, performance tables, and box plots. The produced reports are aimed at providing researchers with immediate insights into device performance and variability, while offering better comparison across experimental conditions.

The tool enhances research efficiency, ensures consistent results, and supports scalable workflows by streamlining data analysis. These features make the tool a highly valuable asset for advancing perovskite solar cell research and development.

AI-based language assistance tools (e.g., ChatGPT) were utilized exclusively to improve grammar, structure, and clarity during the writing of this thesis. The technical content, analysis, and interpretations were developed independently by the author.

**Key words**: perovskite solar cell, photovoltaic data analysis, current-voltage characteristic automation, report generation, multi-pixel devices.

# Table of contents

# 1 Introduction

## 1.1 Challenges in global energy and the role of solar power

The considerable growth in population worldwide and the rapid rate of industrialisation and technological advancements have resulted in the expansion of global energy requirements, creating a significant challenge in the 21st century. The conventional energy sources, specifically, hydrocarbon fuels, which are recognised as the primary energy resource, accounting for approximately 84% of the global energy consumption in 2021 (Augusta Heavens Ikevuje et al., 2024), have been greatly influenced by this surge in energy demand (Afroz et al., 2025). However, detrimental ecological impacts, including serious depletion of resources, air pollution, and global warming, could be caused by excessive dependence on hydrocarbon-based fuels (Martins et al., 2019). With the motivation to combat these environmental challenges, worldwide efforts have been made to develop climate and energy strategies to create incentives to boost the utilization of environmentally friendly energy systems with the purpose of ensuring energy security. For example, the European Union's (EU's) 2030 Climate and Energy Policy Framework has been established to ensure a sustainable, competitive, and secure system of energy across the members of the EU. The targets include achieving a minimum 40% decline in greenhouse gas (GHG) discharge relative to levels recorded in 1990 and renewable energy consumption of a minimum of 27% across the EU (Kulovesi and Oberthür, 2020). In Finland, one of the world's most ambitious climate goals has been set, with a target of accomplishing carbon neutrality by 2035 (International Energy Agency, 2023).

Solar power is widely recognized as a highly compelling and robust alternative to the present inadequate energy infrastructure, as its energy source – the Sun is abundant and nearly inexhaustible. According to recent estimations, the overall global demand for energy could be satisfied by solar energy hourly received by the Earth – a fact that stimulates a staggering number of scientists and engineers to drive the photovoltaic progress (Hayat et al., 2019). Many scientific and engineering communities recognize solar photovoltaics (PVs) as a mature technology. Substantial contributions to minimizing overreliance on fossil fuels could be made by deploying solar power plants at a multi-terawatt scale. A notably steep progression till 2020 has been observed in the global electricity generated via solar PVs (Figure 1). Despite the recent advancements, this technology accounted for merely 6.9% of the global energy generation in 2024 (Graham et al., 2025).

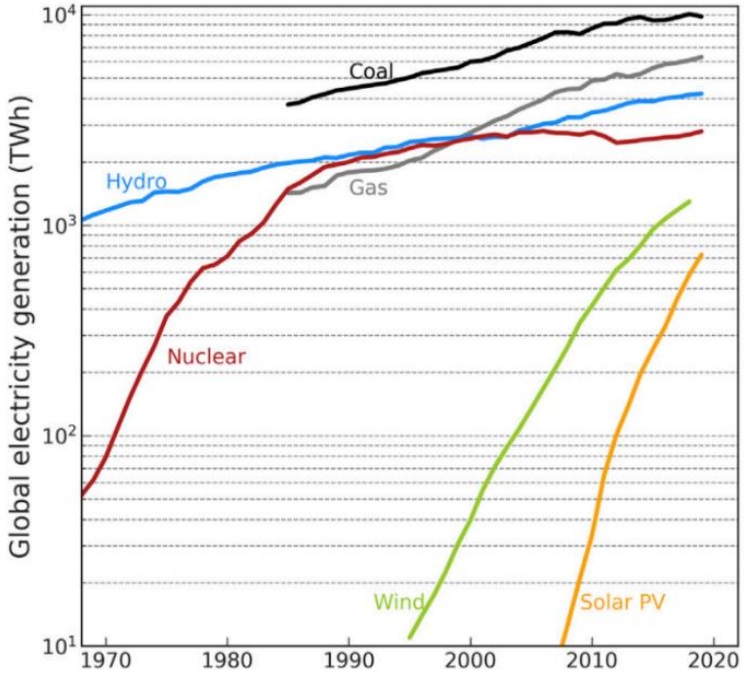


Figure 1. Historical growth of electricity production methods. Reprinted from (Victoria et al., 2021) © 2021 Elsevier, with permission from the publisher.

The most widely commercialized, mature, and leading technology in the current solar PVs is the conventional crystalline silicon (Si)-based solar cells, representing nearly 95% of the total PV market (Di Sabatino et al., 2024). The material's abundance, established processes of manufacturing, and well-recognized long-term stability are the main factors retaining its dominance in the market (Kant and Singh, 2022). However, there are certain limitations that push researchers to explore alternative options to substitute crystalline Si solar cells. Extensive research has been performed to improve the performance of the Si-based solar cells, with the present efficiencies reaching 26.7% and 24.4% for monocrystalline and multicrystalline solar cells in laboratory settings. Researchers have notably reached a 26.81% power conversion efficiency in silicon heterojunction cells by refining the electrical properties of nanocrystalline-silicon hole contacts (Lin et al., 2023). With the Si PV cells slowly advancing toward the 29.4% theoretical thermodynamic efficiency barrier, known as the Shockley-Queisser limit, the scope for further significant performance improvement narrows. Additionally, considerably high manufacturing costs and environmental concerns arise from the energy-intensive production of high-quality silicon, with a temperature demand above 1500 °C (Wong et al., 2016). Stimulated by the previously mentioned limitations, the research into new generation PV technologies has been accelerated to overcome constraints associated with Si solar cells.

## 1.2 Perovskite Solar Cells

The progress in PV technology has been carried through several distinct generations. Each generation is characterized by its performance levels, materials, and fabrication processes. Traditional Si-based PVs belong to the group of first-generation solar cells, primarily produced from wafers of highly purified crystals (Kant and Singh, 2022). Thin-film solar cells, encompassing copper indium gallium selenide, cadmium telluride, and amorphous Si, constitute the second-generation PVs, distinguished by their lower manufacturing costs and relatively low performance in comparison with the first-generation devices (Aamir Iqbal et al., 2022). The solution-processed PVs fall under the category of third-generation solar cells that incorporate perovskite solar cells (PSCs), dye-sensitized solar cells (DSSCs), quantum dot solar cells (QDSCs), and organic photovoltaics (OPVs). The solar devices in this category stand out based on their notably low cost of production and superior PV efficiency. This generation of solar cells can be manufactured with inkjet printing, spray coating, blade coating, and spin coating – scalable methods of fabrication that support low-cost and low-temperature manufacturing (Shah et al., 2023). Among third-generation solar devices, PSCs stand out as one of the most promising technologies, attracting significant research interest over the past few years. Power conversion efficiency (PCE) of PSCs has experienced a dramatic rise since their initial appearance in the research community in 2009, increasing from 3.8% to an impressive 26.1% (Miah et al., 2024). Beyond their notably superior performance, one of the main strengths of PSCs is their low-cost manufacturing enabled by low-cost methods of fabrication. While the more capital-intensive and sophisticated process of manufacturing with a demand for high temperatures is required in the production of Si cells, the fabrication of PSCs could be performed with simpler methods at lower temperatures, contributing to its commercial potential in the PV market. A low recombination rate, high carrier mobility, high diffusion length, long carrier lifetimes, and strong light absorption rate are other outstanding characteristics that make PSCs stand out among other alternatives in their generation (You et al., 2019). Moreover, the bandgap tunability in PSCs allows for their integration in tandem configurations to achieve efficient absorption of sunlight, thereby reaching higher PCE (Tong et al., 2021). Although remarkably high PCE values are obtained in the current PSCs under laboratory conditions, their commercial prospects are constrained by their undesirable instability under environmental stressors, including oxygen, humidity, light, and heat (Nur-E-Alam et al., 2025). Their performance is also difficult to evaluate due to the current-voltage hysteresis, another major challenge posed by their poor stability (Liu et al., 2019). Furthermore,

given the prevalent presence of Pb in PSCs, their commercial usage raises major health and environmental concerns, as the $Pb^{2+}$ ions are released from the decomposition of PSCs (Kim et al., 2023).

The current research directions in the field of PSCs include combating the challenges related to environmental impact, scalability, and stability to realize the commercial deployment of perovskite PVs. Lead-free alternatives to traditional PSCs have been proposed to mitigate the environmental and public health concerns. Germanium, bismuth, and antimony have been suggested as non-toxic candidates to replace lead in PSCs despite exhibiting comparatively inferior PV efficiency to lead-containing PSCs. Given their comparable ionic radius and similar ionic electronic configuration (Wang et al., 2024), one of the most extensively studied low-toxic candidates is tin (Sn)-based perovskites with a record PCE of more than 17% (He et al., 2025). It is widely recognized that Sn-based perovskites offer a notable promise to solve the toxicity issue in Pb-based PSCs, which could be a significant development of highly efficient solar cells. Nonetheless, their stability is limited by the rapid oxidation of $Sn^{2+}$ to $Sn^{4+}$, which is a significant limitation constraining their reproducibility and PV performance (Konstantakou and Stergiopoulos, 2017). Partial substitution, additive engineering, deoxidizer introduction, and reduced dimensions are the possible strategies to support the stability of tin-based PSCs (Yao et al., 2020). $MAPbI_3$ is a popular example among hybrid perovskite solar cells, which combine both inorganic and organic cations. After 5 years of research, an efficiency of more than 20% was achieved with the utilization of low-temperature solution-based techniques in hybrid organic-inorganic perovskites (HOIPs), which possessed an initial efficiency of 4%. The low monetary cost and the composition of Earth-abundant materials are the primary advantages of HOIPs (Brenner et al., 2016). However, the commercialization of such perovskites is restricted by their inferior chemical and thermal stability. For instance, exposure to light, heat, and humidity accelerates the deterioration of hybrid perovskite materials. Additionally, the formation of undesired perovskite hydrates occurs when exposed to water (Valadi et al., 2021). The key source accounting for the HOIP instability has been attributed to the methylammonium cations, as they possess significant hygroscopic properties. Based on this, materials with relatively inferior hygroscopic cation materials, especially caesium and formamidinium have been proposed to respond to this critical barrier (Marimuthu et al., 2022).

## 1.3 Motivation

Addressing the device instability, as one of the key bottlenecks, is critical as it hampers the development and progress in both HOIPs and lead-free PSCs (Y.-Y. Zhang et al., 2018) (Zhang

et al., 2021). In the context of PVs, the term ‘device stability’ denotes a solar cell’s resilience in sustaining high efficiency over time under stress conditions, including temperature, moisture, and oxygen. As the previously standardized protocols for solar cells were tailored for the qualification tests of Si wafer-based solar panels, new testing protocols have been established with the purpose of successfully evaluating the long-term reliability and performance of the device architectures based on PSCs. A series of protocols has been established to set a framework for systematic stability experiments under various stress conditions in the International Summit on Organic PV Stability held in Roskilde, Denmark, in 2020 (Khenkin et al., 2020). These protocols are intended to support the reproducibility of results across different laboratories and encourage researchers to adapt to consistent experimental procedures, making it easy to evaluate results across studies.

Repetitive characterization is required to achieve the accurate assessment of perovskite device performance, as single-point measurements could be misleading due to the unstable chemistry of PSCs. Repeated experiments also ensure statistical reliability in the case of inconsistency in film quality. Driven by the burden of repetitive testing, multi-pixel device architectures, such as 8-pixel PV design, have been introduced, contributing to high-throughput experimentation in the PSC research. These device architectures enable scientists and researchers to perform simultaneous characterization of multiple solar devices under identical conditions, thus minimizing variability among individual measurements. Parallel current-voltage and stability testing across multiple devices is established by various platforms to adjust to the multi-pixel architectures, Fluxim’s Litos Lite being a popular example (Vidani, 2025). However, it should be mentioned that although intensive labour associated with device characterization could be reduced with the measurements based on multi-pixel device architectures, the problem of data analysis remains a crucial challenge, as a significant amount of data is generated by this approach. Errors and inconsistencies are commonly observed in the manual analysis of such extensive datasets. These issues become more serious with the absence of standardized tools for structured batch PV analysis, which have the potential to save researchers’ time, creating a need for automated, reproducible, and standardized data workflows. To combat the challenge of manual data analysis in PV research, especially in the frame of PSCs, is the principal motivation of this thesis. This work aims to offer researchers a reliable tool to streamline data processing, facilitating the commercialization and optimization of PSC technologies.

## 1.4 Scope and Objectives

The primary objective of this thesis is the creation of a software application that automates the analysis of current-voltage data generated from the solar devices with the 2 and 8-pixel active areas. The aims of the tool include streamlining the processing, visualization, and reporting of the key performance metrics of the tested samples. The challenges of error-prone manual analysis and data handling are addressed, combating the factors that constrain research progress.

The following research question has been investigated in this thesis:

How can we develop a software solution that enables reproducible, scalable, and automated analysis of current density-voltage measurements in emerging perovskite solar cell architectures, including 2- and 8-pixel designs, with the goal of improving reproducibility, reducing manual workload, and enhancing research throughput?

There are two key use cases for the developed tool. The first use case for this tool is the processing of data from solar devices with a 2-pixel architecture based on the available current-voltage data and active sample area. Processing data from 8-pixel devices generated with the use of Fluxim Litos Lite platform is the second key use case. The data output from this system is parsed by the prepared software, which subsequently calculates the relevant and significant metrics for each pixel and creates aggregated performance plots and reports.

The researchers could achieve important research outputs by referring to this software, as it incorporates the generation of current density-voltage and power-voltage plots. This feature allows for the creation of a visual representation of device performance across a range of voltage values. The developed tool is also capable of a parameter extraction feature, calculating and deriving the valuable performance metrics, which include fill factor (FF), PCE, short-circuit current density ($J_{sc}$), open-circuit voltage ($V_{oc}$), voltage at maximum power ($V_{mp}$) and maximum power point (MPP). Other crucial parameters for effectively evaluating the PSC stability and quality are series resistance ($R_s$), shunt resistance ($R_{sh}$), and the hysteresis index, which are calculated and reported via the proposed software. The generated reports also include boxplot visualizations, which provide a summary of the distribution of essential performance metrics ($J_{sc}$, $V_{oc}$, FF, and PCE) across various samples or measurements. A comprehensive and detailed PDF report for each measurement set or sample is the final output of the developed software. The current density-voltage/power-voltage graphs, calculations of performance parameters, boxplot visualizations, and a summary table of essential metrics are included in the report.

# 2 Review of Materials, Metrics, Methodologies

## 2.1 Perovskite Solar Cells: Materials and Device Architectures

The researchers in Miyasaka's laboratory at Toin University in Yokohma, Japan were the first ones to start the exploration of the PV applications of halide perovskites, popularizing the term 'perovskite solar cell' (Kojima et al., 2009). At that time, the word 'perovskite' was used to describe the metal oxide compounds with a perovskite crystal structure, mainly recognized for their piezoelectric or ferroelectric characteristics. Perovskite typically refers to a particular type of crystal lattice characterized by the chemical formula of $ABX_3$. Cations are denoted by A and B, while X is an anion in the given formula (Figure 2). An octahedron of anions surrounds the cation B, which possesses a 6-fold coordination in an ideal cubic perovskite structure. Concerning the other cation A, it has a 12-fold cub-octahedral coordination. Cation A lying at the body-centred position, B cation occupying the cube corners, and X anion placed at the face-centred positions constitute the cubic unit cell of the perovskites (Jena et al., 2019). A key benefit of the perovskite structure lies in its capacity to accommodate elements with varying valence states. For instance, if oxygen anion is placed in the place of X, the A and B-site cations will typically have valences of +2 and +3, respectively. By contrast, having a halogen anion in the X-site leads to A and B cations generally exhibiting monovalent and divalent states (Park, 2018). This feature allows for the modification of the properties, including the material bandgap, offering an opportunity to enhance the performance. Halide perovskites have ionic crystals with semiconducting properties, unlike traditional semiconductors.

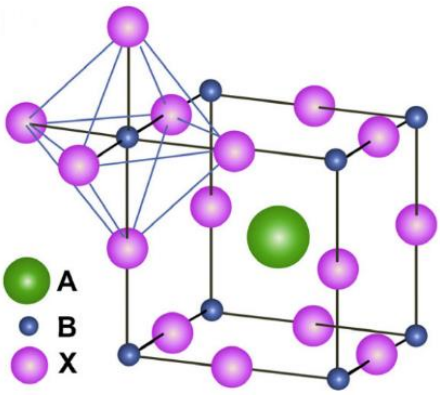


Figure 2. The $ABX_3$ structure of the perovskite crystal. Reprinted from (Park, 2015), which is open access under the CC BY-NC-ND license.

Two empirical parameters, the Goldschmidt tolerance factor (t) and octahedral factor ($\mu$), play a crucial role in the stability of the perovskite crystal structure (Afre and Pugliese, 2024). These parameters are defined as follows:

$$t = \frac{r_A + r_X}{\sqrt{2}(r_B + r_X)} \quad (1)$$

$$\mu = \frac{r_B}{r_X} \quad (2)$$

The parameters, $r_A$, $r_B$, and $r_X$ denote the ionic radii of the A, B, and X ions, respectively. The degree of fit between the A cation and the $BX_6$ octahedron is gauged by the tolerance factor, whereas the octahedral factor measures the distortion degree of the octahedron. In the ideal perovskite structure, both these parameters are equal to 1. Any deviations from these values indicate distortion and structural instability. Structural stability in perovskites is typically observed when the octahedral factor (μ) falls between 0.44 and 0.94, and the tolerance factor (t) lies between 0.8 and 1.1. Generally, most of the perovskites deviate from the ideal structure and exhibit lower symmetries, such as tetragonal, orthorhombic, rhombohedral, or monoclinic, although the t value is 1 in the ideal cubic structure. These distortions lead to the development of ferroelectric or anti-ferroelectric phases, resulting in a periodic alternation of electric polarization and spontaneous polarization, respectively (Mirseraji and Shahraki, 2018).

According to the history of minerals, Prussian mineralogist Gustav Rose was the first one to discover perovskite in a piece of chlorite-rich skarn in 1839 (Katz, 2020). The material discovered was $CaTiO_3$ and was named after the Russian mineralogist Count Lev A. Perovskiy. Followingly, the exploration and recognition of further inorganic metal oxides, such as $BaTiO_3$ and $PbTiO_3$ exhibiting the perovskite structure, followed; hence, the metal oxides with the $ABO_3$ formula are collectively referred to as perovskite compounds. Given their optical absorption and luminescence properties, the early research on these materials was primarily focused on their application in nonlinear optics and electroluminescence devices, such as LEDs (Ema et al., 2006). As the initial 2D perovskites displayed limited light-harvesting capabilities over the broad spectral range of sunlight, the prospect of utilizing these materials in PVs was largely overlooked. The use of an organic-inorganic lead halide perovskite as an absorber to substitute the organic dye in DSSCs marked the first appearance of PSCs in the PV research, with limited awareness of their immense potential in 2005. An important development of PSCs was the research conducted in 2011 at the Henry Snaith group (Lee et al., 2012), a notable milestone supporting the progression of PSCs from an initial PCE of 3.8 to over 25% (Liu et

al., 2022). A significant shift in the development of PV technology was marked by his work, which showcased the use of hybrid organic-inorganic perovskites as efficient light absorbers. A foundational understanding of perovskites and their PV properties led to a surge of interest in research aimed at enhancing the PCE of PSCs. The National Renewable Energy Laboratory (NREL) maintains a record of the highest confirmed research-cell efficiencies across various photovoltaic technologies, charting progress from 1976 to the present. This allows for direct comparison of PSC advancements against competing technologies (Figure 3).

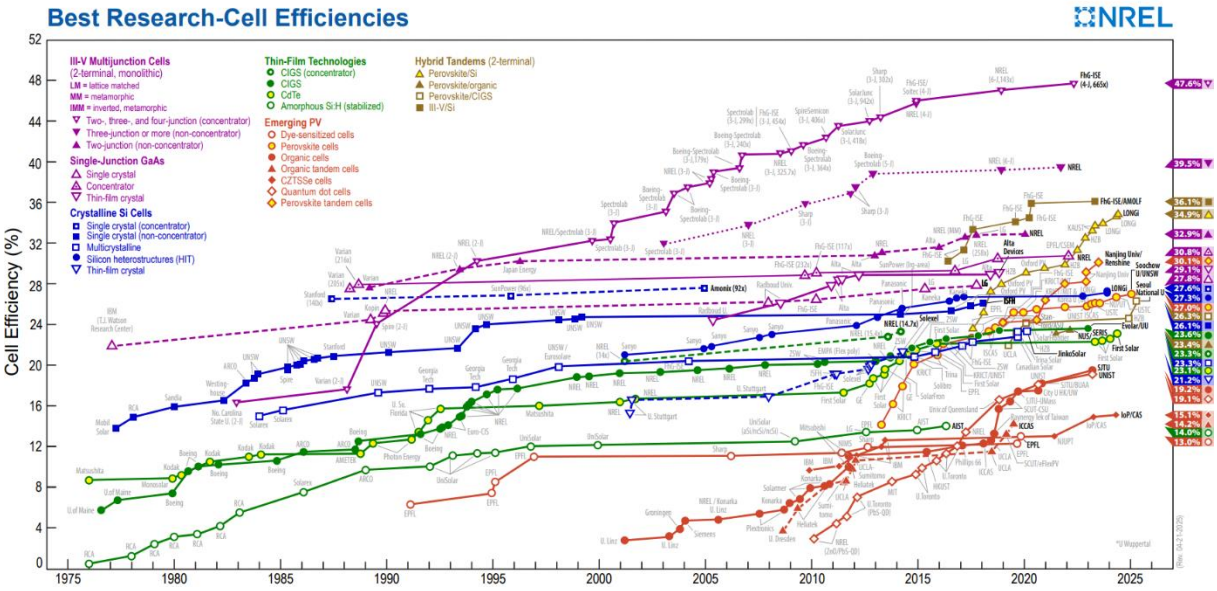


Figure 3. NREL Best Research-Cell Efficiency Chart illustrating the highest confirmed conversion efficiencies for various photovoltaic technologies over time, which is accessible on NREL's official website ("Best Research-Cell Efficiency Chart," 2025).

As the high-quality perovskite film is the requirement for accomplishing high-efficiency cells, the early developments of PSCs focused on the fabrication of high-purity and defect-free perovskite films. The undertaken studies investigating the relationship between cell performance and perovskite film morphology made it evident that the key prerequisite to high energy yield was a dense (pinhole-free) and flat perovskite absorber with superior crystallinity and large domains (Jena et al., 2019). The processes to prepare high-quality perovskite films were developed thanks to a great amount of effort devoted by researchers.

In earlier research activities, the initial hypothesis was that the perovskite solar materials would function similarly to the dye in DSSCs, with a requirement of a mesoporous layer to facilitate electron transport (Miyasaka, 2015). However, further research on perovskite devices with an insulating $Al_2O_3$ mesoporous layer revealed that PSCs can function independently, meaning that the transport of holes and electrons could occur through the film itself without the

requirement of additional semiconducting scaffold, as is commonly needed in the case of sensitized solar cells. This new understanding contributed to further progress in the PSC field, differentiating the operating principle of the perovskite solar cell from the sensitization mechanism. The diversity of device architectures developed later in the field gave sufficient grounds to confirm that the PSCs' operation exhibits similarity to that of the solid-state p-n junction solar cells. The widely recognized understanding today is that the working mechanism of PSCs resembles that of conventional negative-intrinsic-positive (n-i-p) and positive-intrinsic-negative (p-i-n) solar cells, with the perovskite layer functioning as the intrinsic light-absorbing layer positioned between n-type and p-type selective contacts.

In an n-type semiconductor, donor impurities with more valence electrons than the host semiconductor (e.g., phosphorus in silicon) are introduced to generate excess free electrons, which become the majority charge carriers. In contrast, a p-type semiconductor is formed by introducing acceptor impurities with fewer valence electrons (e.g., boron in silicon), resulting in the formation of holes as the majority charge carriers. When p-type and n-type semiconductors are brought into contact, electrons diffuse from the n-type region into the p-type region and recombine with holes, and vice versa. This mutual diffusion creates a depletion region near the junction, where mobile carriers are absent due to recombination. The immobile ionized dopants left behind establish an internal electric field, giving rise to a built-in potential that inhibits further diffusion and enables efficient charge separation under illumination. In PSCs, the intrinsic perovskite layer (denoted as 'i' in n-i-p and p-i-n architectures) functions as the active light-absorbing material, where photon absorption generates electron–hole pairs (Sze and Ng, 2006).

The basic device structure of PSCs consists of a metal contact (cathode), a transparent conductive oxide (anode), an electron transport layer (ETL), and a hole transport layer (HTL). The transparent conductive oxide, which is typically either indium tin oxide or fluorine-doped tin oxide, can act as a transparent electrode, allowing light to pass through it while being conductive. Subsequently, electron and hole pairs emerge as a result of the incident radiation absorbed by the perovskite layer. The p-type HTL collects the holes selectively, while the n-type ETL extracts electrons. The charge-collecting contacts enable charge carriers to travel towards the external circuit, generating electricity. The fabrication processes of PSCs differ depending on the deposition order of charge transport layers, specifically whether the ETL or HTL is laid down as the first layer. As a result of this, two categories of device architecture emerged, which are defined as 'standard' (n-i-p type) and 'inverted' architecture (p-i-n type);

(Figure 4). The n-i-p configuration is more common in research due to higher efficiencies, while p-i-n PSCs are recognized for better stability (Zhang and Park, 2024a).

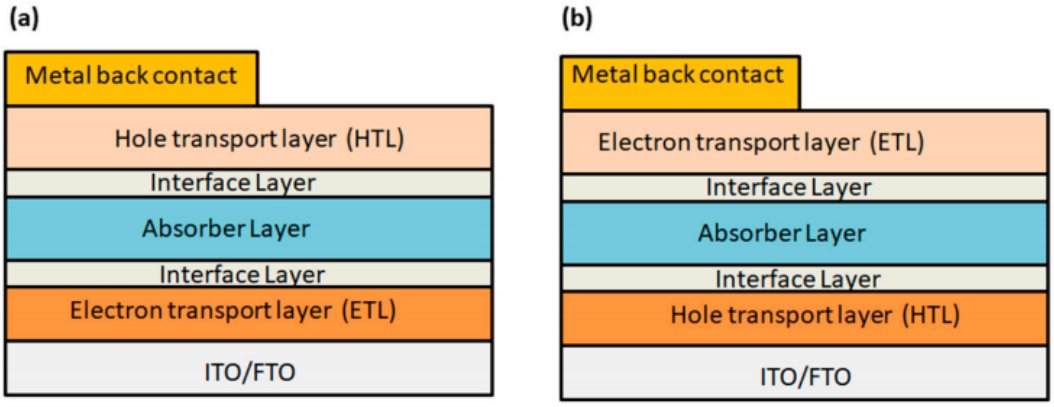


Figure 4. Device architecture of PSCs. (a) n-i-p configuration and (b) p-i-n configuration. Reprinted from (Roy et al., 2022a), which is open access under the CC BY license.

The first proposal of the n-i-p architecture was made in 2009, in which the material of ETL was selected as titanium oxide (TiO2) in comparison with DSSCs (Kojima et al., 2009). The first publication of a p-i-n type device occurred four years later in 2013, where the poly (3,4-ethylene dioxythiophene) doped with poly (styrene-sulfonate) was employed as an organic HTL (Jeng et al., 2013). High PCE values above 20-22% are accomplished in both architectures (Al-Ashouri et al., 2019). However, the reported peak efficiencies for single-junction solar cells are mostly achieved with an n-i-p type structure, whereas the devices with p-i-n type configuration and similar perovskite materials show considerably inferior performance (Zhang and Park, 2024b). The lower open-circuit voltage (Voc) commonly observed in p-i-n type PSCs could be the leading cause of this difference, owing to nonradiative recombination losses at the interface between the perovskite absorber and ETL (Stolterfoht et al., 2019) (Warby et al., 2022). The comparison of n-i-p and p-i-n type architectures with the same materials for charge transfer layers was made by very few authors. As the distinct ETLs and HTLs are suitable for a given architecture due to their process compatibility and ability to enhance performance, the choice of materials frequently varies. `In contrast, the study of C. Momblona et al. stands out, as it offers a direct comparison and in-depth optimization of the two organic interfacial materials across both perovskite solar configurations (Momblona et al., 2016). The conclusion was that high efficiencies could be achieved with both configurations employing the same elaboration process. Significantly, the n-i-p structure demonstrated enhanced efficiency, especially reflected in higher FF and Voc values. The inferior performance attributed to the p-i-n structure could stem from the p-type interface, in which the movement of holes is notably obstructed.

In order to accomplish the optimal charge carrier extraction, materials selected in ETL and HTL must have a favourable band alignment with the absorber (Hussain et al., 2018) (Minemoto and Murata, 2015). It is required to carefully select and fabricate all three material layers to acquire the optimum PCE in PSCs. The results showed that the layer thickness has a critical impact on the quality of the three layers (Roy et al., 2022b). The research indicates that the most favourable transport layers are those with minimal thickness, while maintaining uniform film coverage over the perovskite layer. The optimal thickness of the absorber layer corresponds to the carrier diffusion length of the employed perovskite. The significance and necessity of the energy level alignment at the interfaces of ETL/perovskite and perovskite/HTL are further explained in other studies (Roy and Khare, 2022). Concerning the material selection of charge transport layers, Spiro-OMeTAD (2,2',7,7'-tetrakis (N,N-dimethoxyphenylamine)-9,9'-spirobifluorene) is one of the widely utilized materials for HTLs, costing ten times more than Gold and Platinum. The future improved materials for HTL are anticipated to substantially support the further progression of PSCs, as the instability of PSCs is attributed to the organic HTLs due to their participation in the degradation process. Research direction in this field is currently targeted at inorganic alternatives with low cost. The most popular ETL materials include $TiO_2$ with its superior stability and $SnO_2$ due to its wide bandgap of 3.6-4.1 eV. Among ETL materials, $SnO_2$ appears as a choice with the most potential, owing to its high mobility 240 $cm^2/V$, high optical transmittance, and low temperature fabrication (Raj et al., 2021).

A transparent conductive electrode (TCE) is a key element essential to the functional performance of solar cells, as it both performs the transmission of incident light to the absorber layer and the extraction of photo-generated charge carriers to the external circuit. The important features of TCEs are conductivity and proper transparency (Lavagna et al., 2021). A high-quality and effective TCE requires a necessary balance between transparency and conductivity. The common choices for TCE are ITO and FTO owing to their excellent transparency and conductivity, making them well-established selections. The challenges of these materials include flexibility-limiting brittleness and high cost (especially for ITO) (Xu et al., 2021), leading to the exploration of substitute candidates such as silver nanowires, graphene, and perovskite-based transparent conducting oxides ($SrVO_3$ and $BaSnO_3$) (He et al., 2020).

The effectiveness of PSC devices stems from their unique properties. The long diffusion wavelength (>1 μm) and high electron mobility (800 $cm^2/Vs$) are the primary features of PSCs contributing to their high PV performance (Bhandari et al., 2020a) (Bhandari et al., 2020b). A low exciton binding energy estimated to be less than 10 meV is another worth-mentioning

feature of PSCs, contributing to the migration of excited carriers as free carriers. Moreover, a high absorption coefficient ($10^5$ $cm^{-1}$) is exhibited in these materials, primarily stemming from s-p antibonding coupling (Miyata et al., 2015). The perovskite materials offer a large range of band gaps due to their easy tunability (Table 1). $CH_3NH_3PbI_3$ is among the most frequently employed perovskite materials, where the various perovskite materials could be formed by modifying the X-site anion and cations positioned in the A and B-sites.

Table 1. A summary of the electrical and optical features of PSCs. Reprinted with permission from (Roy et al., 2022a), which is open access under the CC-BY license.

| **Parameters** | **Values** | **Units** |
|---|---|---|
| Absorption coefficient | $10^5$ | $cm^{-1}$ |
| Bandgap | 1.2-2.5 | eV |
| Crystallization energy barrier | 56.6-97.3 | kJ $mol^{-1}$ |
| Charge carrier lifetime | >300 | nm |
| Carrier mobility | 800 | $cm^2/Vs$ |
| Exciton binding energy | <10 | meV |

There have been notable advancements in the investigation of alternative A-site cations to substitute ($MA^+$, $CH_3NH_3^+$) in PSCs, resulting in higher PCEs and better stability. Initial attempts involved the use of ethylammonium ($EA^+$, $CH_3CH_2NH_3^+$), and this resulted in a wider bandgap and a low PCE of 2.4% with limited practicality.

In contrast, formadinium ($FA^+$, $NH{=}CH{-}NH_2^+$) has appeared as a better alternative. This led to a narrower bandgap of nearly 1.43-1.48 eV with superior light absorption properties and PCEs. Up to 26.02% of PCEs have been accomplished in recent studies exploring $FA^+$-based PSCs (Zhao et al., 2025). Higher efficiencies could be attributed to enhanced thermal stability and stronger hydrogen bonding with $PbX_6$ octahedra. Furthermore, researchers have employed mixed-cation perovskites, involving $FA^+$ with $Cs^+$ or other cations, resulting in superior phase stability and suppressed defects. These attempts resulted in PCEs exceeding 25% and operational stability over 1,000 hours under continuous illumination (Elangovan et al., 2024). Based on this progress, it could be said that A-site cation engineering contributes significantly to enhancing PSC performance.

The bandgap can also be tuned with the replacement of the iodide anion ($I^-$) with other halide anions. The bandgap increases by replacing iodide with smaller halides like chloride ($Cl^-$) or bromide ($Br^-$). For example, while $MAPbI_3$ demonstrates a bandgap of ~1.57 eV, the bandgap of $MAPbBr_3$ is ~2.2 eV. The stronger halide-metal bonds and reduced lattice constant could be the causes of this difference (Miah et al., 2024). The widening of the bandgap can lead to

reduced light absorption, negatively influencing PCE. There has been considerable progress in mixed-halide perovskites, such as $FAPb(I_{0.8}Br_{0.2})_3$, yielding ~1.6 eV and PCE up to 21.2% (Elangovan et al., 2024). The mixed halide perovskite $CH_3NH_3Pb_{3-x}Br_x$ was explored to enhance device efficiency and operational durability. This perovskite had a tunable bandgap between 1.6 and 2.3 eV, determined by the composition of bromide (Hu et al., 2016). Lead cation in the PSCs is also targeted to eliminate the challenge of toxicity, most popular alternatives being Sn, Ge, Bi, and Sb. Despite ongoing attempts, replacing the Pb-based PSCs remains a significant challenge since they generally have higher performance compared to the PSCs without lead content (Wu et al., 2021a).

A lack of stability is the most significant challenge experienced in the PSC commercialization, with the primary culprit being the chemical interactions within the perovskite structure. The weak bonds mostly constitute the interactions; for instance, a bonding energy of 142 kJ $mol^{-1}$ has been reported in Pb-I bonding (N. Li et al., 2020). Hydrogen bonding and van der Waals forces are worth mentioning secondary interactions, major reasons behind the soft nature of PSCs (Wu et al., 2021b). The cell of this chemistry could degrade under the most environmental stressors, as the PSCs intrinsically exhibit vulnerability to light, heat, electric fields, oxygen, and moisture (El-Mellouhi et al., 2016). One particular study has reported that perovskites with iodide anions are characterized by a negative standard Gibbs free energy with regard to moisture degradation, making them especially sensitive to moisture and water (Niu et al., 2014). The commercialization of PSCs requires a long operational life, necessitating solutions to address issues of stability. The degradation mechanism of PSCs should be studied further to develop enhanced stabilisation and encapsulation approaches.

The production of perovskite solar cells involves a less intricate fabrication process compared to that of silicon solar cells, as they are comprised of more Earth-abundant and cost-effective elements(H. Li et al., 2020). The manufacturing process of Si-based solar cells is energy-intensive, involving temperatures above 1000°C in a vacuum-sealed chamber (Ansari et al., 2018). In contrast, straightforward solution-based methods could be employed to synthesize perovskite materials, avoiding the complexities of vacuum-based systems. Achieving optimal crystallinity, a determining factor in device efficiency, is heavily dependent on the techniques and conditions used during the PSC fabrication. Solution- and vapor-techniques are the primary methods for the fabrication of perovskite films (Kosasih et al., 2022).

Spin-coating is one of the most common solution-processing methods to synthesize PSC films. In this fabrication technique, centrifugal force is applied to spread a liquid film onto a rotating substrate. This method can be employed to produce small PSCs with sizes ranging from 0.1 $cm^2$ to 1 $cm^2$ (Hamukwaya et al., 2022). Either a one-step approach or a two-step sequential approach is followed in this fabrication method. The one-step approach involves a polar aprotic solvent such as dimethyl sulfoxide (DMSO) and N, N-dimethylformamide (DMF) to dissolve a mixture of $PbX_2$ (X = Cl, I, Br) and AX (A = MA, FA, Cs). Subsequently, the prepared perovskite precursor solution is applied onto the substrate via spin-coating to produce the perovskite film (Xu et al., 2022). The non-uniform film morphology is often observed in the one-step spin-coating method due to the rapid growth of precursor crystals and the low perovskite nucleation rate (Gao et al., 2021). In the initial step of the two-step or 'sequential' deposition method, a thin film of $PbX_2$ is formed by spin-coating a solution dissolved in a polar solvent, typically DMF. In the subsequent step, the substrate is either submerged in an isopropanol solution containing AX, such as MAI, or the AX solution is deposited using spin-coating. The process concludes with the thermal annealing at around 100 °C for a minimum of 30 min to enable the crystallization of the perovskite layer. The two-step technique allows for better control of the press than the one-step approach (Becker and Wark, 2018). Experimental conditions, such as solution concentration, precursor composition, annealing temperature, and annealing time, are factors that could highly impact the quality of perovskite films produced via spin-coating (Bae et al., 2022). The researchers mostly prefer the one-step method over the two-step method, although the latter has assisted in the fabrication of solar cells with higher performance (Roy et al., 2022a). Despite its benefits, the spin-coating may not be very suitable for large-area and large-scale production of PSC films, since the film quality and uniformity deteriorate with increasing cell area (Hamukwaya et al., 2022).

The vapor deposition method was first used in 2013, assisting in the production of $MAPbI_{3-x}Cl_x$ films (Liu et al., 2013). It is one of the most sophisticated and widely adopted industrial methods for producing optoelectronic thin films. There are three main approaches to vapor deposition: (1) single-source technique, (2) co-deposition technique, and (3) layer-by-layer technique. A single-source method involves the deposition of pre-prepared films or powder from a single source. In the co-deposition approach, several individual precursor materials are simultaneously deposited, whereas the individual precursor materials are sequentially deposited in a layer-by-layer method. Among vapor deposition techniques, co-deposition has attracted the most research attention to date, as it allows easy composition tuning with commonly available

laboratory evaporation systems. Using specialized vacuum chamber systems maintained at high vacuum, vapor deposition methods evaporate precursor materials (e.g., organic-inorganic halide pairs) simultaneously or in sequence by raising their vapor pressures above the chamber's ambient pressure. The phase transition from solid precursors to vapor phase is typically achieved through radiative heating, where electrically energized filaments transfer thermal energy to IR-transparent crucibles containing the source materials. The vaporized molecules travel through the vacuum environment and subsequently condense onto a relatively cooler substrate surface, where they undergo nucleation and crystallization to form a high-purity thin film. The commercialization of perovskite PV technology heavily relies on vapor-processed perovskite solar cells due to their scalability and reproducibility (Abzieher et al., 2024).

## 2.2 Lead-free and low-toxicity perovskites

One of the elements of the light-absorbing hybrid perovskite layer is lead (Pb), raising significant worries about the possible risks to both public health and the ecosystem (Wang et al., 2021). Advancing the commercial viability of PSCs has driven research toward the design of low-toxicity and lead-free perovskite compounds. The most investigated perovskite for PV applications is methylammonium lead trihalide ($MAPbX_3$), given its favourable optoelectronic properties, encompassing a long charge carrier diffusion length, a low trap density, a tunable band gap, and a high absorption coefficient (Unger et al., 2017). In contrast, as it can have detrimental effects on the reproductive organs, nervous system, and kidneys, as Pb is considered highly toxic. Lead can enter the human body primarily through three exposure pathways: inhalation, ingestion, and dermal absorption. Once entered the body, lead circulates via the bloodstream, accumulating in soft tissues, such as the liver, kidneys, and nervous system, as well as depositing in the skeletal system, which functions as a long-term storage site for lead (Magdalin et al., 2023). This disrupts enzymatic and receptor functions in soft tissues and interferes with haem activity in the bloodstream (Babayigit et al., 2016). Male and female reproductive systems could also be negatively affected by lead. Lead reduces sperm count in males, while premature birth and miscarriages are caused by toxic levels of lead in females. Lead toxicity also culminates in decreased neuronal growth and interferes with neurotransmission, as the human brain is susceptible to lead deposition in the body (Wani et al., 2015). A wide range of industries also has a high demand for Pb due to its limited availability, contributing to its status as a high-cost and low-abundance material. Encouraged by these issues, several elements and compounds have been explored to substitute lead in the

PSCs aimed at minimizing toxicity and economic burden while preserving device efficiency and operational durability. Most explored alternatives for lead in the PSC fabrication have been metals, including tin (Sn), germanium (Ge), and bismuth (Bi).

Perovskite materials with tin content are the most investigated alternative to lead-containing perovskites (Fu, 2019). Tin, a group 14 element, possesses an electronic configuration of $5s^2$, which closely resembles that of lead with a $6s^2$ configuration. With a comparable valence electron configuration and a compact ionic size, tin is considered a promising and less toxic substitute for lead in PSCs (Q. Zhang et al., 2018), (Wang et al., 2019). Tin-based perovskite solar cells exhibit superior carrier mobility, low exciton binding energy, and a narrow bandgap, which are advantageous properties (Liu et al., 2020). Photons up to 900 nm can be harvested thanks to the low bandgap of Sn-based perovskites. Higher environmental compatibility is observed in Sn-based perovskites compared to their Pb-based counterparts. This is mainly since the degradation byproducts of Sn-based perovskites tend to hydrolyze in water, forming compounds $SnO_2$, $SnI_4$, and $(MA)_2SnI_4$, which are less soluble than the corresponding byproducts produced from Pb-based perovskites (Galve-Lahoz et al., 2024). One notable example of tin-based perovskite materials is $FASnI_3$, whose PCE varied between 4.0 and 15.7% (Shtangeeva et al., 2011) , (Shi et al., 2024). Despite their valuable characteristics and successful application in solar cells, Sn-based perovskites often suffer from the inherent instability of the $Sn_2$ state, leading to excessive conductivity, which in turn results in poor reproducibility and reduced performance (Song et al., 2017). The efficiency of tin-based lead-free PSCs is also limited by the typical rough morphology and high defect concentration. The structural defects in tin-based PSCs facilitate the adsorption of oxygen and water molecules onto the perovskite layer, which, in turn, accelerates the degradation of solar cells, adversely affecting their efficiency (Xie et al., 2019).

An Earth-abundant element of germanium is a group 14 element, and $Ge^{2+}$ has an electronic configuration of $4s^2$ with an ionic radius of 0.73 Å (Yang et al., 2021). The compounds involving germanium, including its organogermanium derivatives, have the advantage of low toxicity, except tetrahydride germane (Gerber and Léonard, 1997). Germanium is considered an alternative option to lead in PSCs, given the more covalent nature and higher electronegativity of $Ge^{2+}$ compared to $Pb^{2+}$ (Kopacic et al., 2018). One particular study compared the properties of $MAGeI_3$ and $MAPbI_3$ and reported that the former possessed a similar bandgap, higher stability, more favourable optical properties, and considerable electron and hole conductive nature (Sun et al., 2016). There are significant challenges with Ge-based

perovskites despite their advantages. Device instability and poor performance are the primary obstacles, limiting the commercial applications of Ge-based PSC in PVs. The oxidation of divalent germanium ($Ge^{2+}$) is the primary challenge in PSCs involving germanium, being the main culprit behind its poor performance. In spite of the current limitations, Ge/Sn-based mixed perovskites hold promise, particularly if further studies accomplish efficiencies of more than 10%. One of the examples of such PSCs with a relatively high efficiency of 7.11% is lead-free inorganic caesium tin-germanium triiodide ($CsSn_{0.5}Ge_{0.5}I_3$). This perovskite solar cell demonstrated excellent stability, with performance degradation remaining below 10% after 500 hours of continuous operation under 1 Sun illumination in a nitrogen environment. The stability of this material is credited to the developed passivating native-oxide layer (Chen et al., 2019). High material costs pose a significant barrier to the broader adoption of germanium-based solar cells. The price average for Ge between 2006 and 2010 has been estimated to be 1172 USD per kg (Schileo and Grancini, 2021).

Bismuth (Bi) is an element placed in group 15. Trivalent bismuth has an electronic configuration of $6s^2$ and is stable. $Bi^{3+}$ has an ionic radius of 1.03 Å, which is close to lead. Compared to lead, bismuth possesses low-toxicity properties. Diverse dimensionality is observed in $BiX_6^{3-}$ octahedron. Notably, bismuth subsalicylate and bismuth subcitrate are utilized as medicinal compounds (Lambert, 1991). Nonetheless, renal failure and encephalopathy could be the result of chronic intake of bismuth. Given the isoelectronic valence shell of bismuth, researchers have dedicated significant attention to Bi-based PSCs (Ganose et al., 2017). Bi-based PSCs exhibit environment-friendly chemistry, remarkable optoelectronic properties, and high stability under moisture, heat, and light, making them a promising alternative to PSCs, including lead. The comparison of the optical properties of lead, antimony, and bismuth-based perovskite films revealed that the latter demonstrated the greatest resilience, maintaining stable optical and structural properties and exhibiting no substantial degradation over three months without the need for surface passivation. One of the famous Bi-based solar cells is methylammonium iodobismuthate ($(CH_3NH_3)_3Bi_2I_9$ which was first fabricated in 2017, demonstrating a PCE of 0.39% and high reproducibility (Ran et al., 2017). Bi-based PSCs are a viable option toward stable and environmentally friendly perovskite solar cells; however, the poor surface morphology and high band-gap energy are the main constraints (Kim et al., 2016).

Double perovskites are structural derivatives of the standard perovskite formula $ABO_3$, in which a different $B^{'}$ cation substitutes half of the B site cation, forming a new compound with a double perovskite structure typically expressed as $A_2BB^{'}O_6$ (Saha-Dasgupta, 2020).

Confinement of double perovskite materials to nanoscale monolayers leads to quantum size effects and enhanced stability, attributed to the elevated surface energy of nanocrystals in metastable phases. Although certain materials, such as $Cs_2AgBiI_6$, are challenging to fabricate in bulk form, they have demonstrated stability when synthesized as nanocrystals. The quaternary nature and the availability of combinatorial compositions in double perovskite materials result in flexible bandgap tunability (Khalfin and Bekenstein, 2019). In comparison to other lead-free structures, lead-free double PSCs exhibit chemical stability, ecologically friendly nature, and remarkable electronic dimensions with substitutional chemistry. The application areas of double perovskites encompass renewable energy and optoelectronics, such as light-emitting diodes (LEDs) and X-ray detectors (Dave et al., 2020). Robust optoelectronic characteristics were observed in the recently fabricated lead-free double perovskites, which include $Cs_2BiAgCl_6$, $Cs_2BiAgBr_6$, and $Cs_2SbAgCl_6$ (Volonakis and Giustino, 2018). Although the lead-free double perovskites are viewed as promising owing to their non-toxic and highly stable nature, their photophysical properties are limited by parity-forbidden absorption, low carrier mobility, and wide electronic bandgaps with indirect characteristics. Consequently, significant research is still required to gain a comprehensive understanding of their structural and photophysical characteristics, as well as to investigate the broad chemical landscape in search of novel lead-free double perovskites exhibiting enhanced optoelectronic properties and improved thermal stability (Zhan et al., 2023).

## 2.3 Essential PV performance metrics

In order to acquire a detailed description of device performance and material quality, I-V curve measurements are typically performed. I-V curves illustrate the current-voltage behaviour of a given PV cell. Engineers refer to I-V curves with the purpose of configuring a solar system operating at the optimal peak power point. These measurements are generally conducted under standardised conditions to ensure comparability and consistency across different products and studies. The spectrum that should be illuminated on the solar cell should be the AM1.5 spectrum according to the standard test conditions (STC). AM1.5 spectrum is also called ‘standard’ spectra, which is essential in evaluating the performance metrics across various PV devices, as solar devices exhibit spectral selectivity, meaning that their performance metrics differ depending on the incident spectrum. Air mass (AM) is defined as the relative distance that the direct solar beam travels through the Earth’s atmosphere. The path length is 1.0 (AM 1.0), when the Sun is directly overhead. Since the Sun is rarely positioned directly overhead at solar noon across most seasons and geographic locations, solar device characterization rarely relies on AM

1.0 conditions. The air mass increases in accordance with the angle of the Sun from zenith, nearly by the secant of the zenith angle. Hence, the air mass is defined as 1.5 when the Sun is positioned at 48 degrees from the vertical (Figure 5).

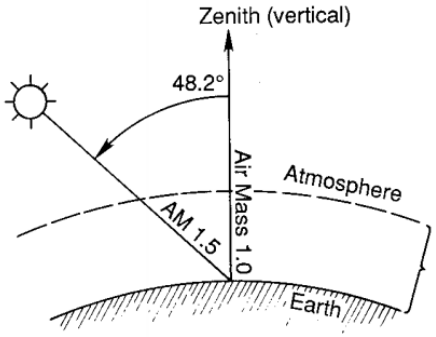


Figure 5. Schematic illustration of solar air mass conditions. Reprinted from (Riordan and Hulstron, 1990), © 1990, IEEE, with permission from the publisher.

AM 1.5 was selected as the standard for testing terrestrial solar cells, as it closely matches the average irradiance conditions observed in most temperate regions with significant input of solar energy, providing a basis for comparing the efficiency of various PV devices under representative and realistic conditions. Furthermore, for measurements performed under STC, the solar cell is required to receive an irradiance level of 1000 W/m$^2$. To achieve comparable results across different solar cells, the standard operating temperature for testing is selected to be 25 °C, as temperature plays a critical role in determining the performance of solar cells (Montes-Romero et al., 2016).

In PV characterization, the orientation of the I-V curve can vary depending on the adopted sign conventions, which are different across laboratories and software platforms. $I_{sc}$ is plotted as positive with the assumption that the solar cell delivers the current to an external load (Figure 6). Short-circuit current can be represented as negative by some researchers and software tools. This is attributed to the passive sign convention commonly used in electrical engineering, where current flowing out of the device is considered negative.

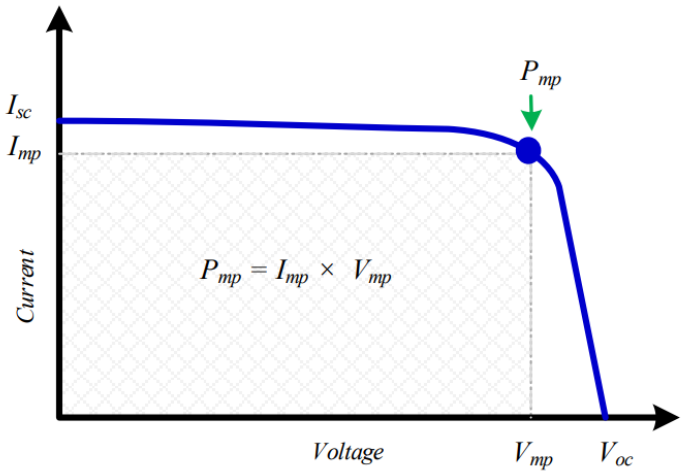


Figure 6. Typical current-voltage (I-V) curve of a solar cell under standard illumination conditions. The key PV parameters – short-circuit current ($I_{sc}$), open-circuit voltage ($V_{oc}$), current at maximum power point ($I_{mp}$), voltage at maximum power point ($V_{mp}$), and maximum power output ($P_{mp}$). Reprinted from (Khunchan and Wiengmoon, 2018) which is under the CC BY license.

The I-V measurements allow researchers to determine the essential PV metrics (Figure 6), which are the maximum power ($P_{mp}$), short-circuit current ($I_{sc}$), open-circuit voltage ($V_{oc}$), and the fill factor (FF). The current measured in the external circuit when the solar cell electrodes are short-circuited is called the short-circuit current $I_{sc}$. The photon flux incident on the solar cell, determined by the spectrum of the incident light, has a major role in the short-circuit current of a solar cell, necessitating the use of the AM 1.5 spectrum to ensure the comparability of PV measurements across laboratories. As poor surface passivation can lead to recombination losses, it is another factor that can adversely affect $I_{sc}$. Furthermore, diffusion lengths in perovskites, which refer to how far charge carriers can travel before recombining, highly impact $I_{sc}$ of solar cells. The active solar cell area, which is responsible for the power generation, is also capable of affecting the $I_{sc}$. The short-circuit current density ($J_{sc}$), defined as the maximum current per unit area generated by a solar cell, is often used instead of $I_{sc}$ to avoid area-related variability. This parameter is essential in efficiency calculations and reflects how effectively the solar cell absorbs light and converts photons into charge carriers. The optical characteristics of the solar cell, including reflection and absorption within the absorber layer, are key determinants of the maximum current output achievable.

The open-circuit voltage is defined as the voltage measured across the solar cell terminals when no current flows through the external circuit (i.e., under open-circuit conditions). It corresponds to the voltage at which there is a balance of the generated photocurrent and recombination current, leading to a net current of zero. The recombination mechanisms within the solar cell have drastic impacts on this parameter. Moreover, an increase in temperature leads to a

reduction in $V_{oc}$. Notably, higher bandgap materials generally yield a higher value for open-circuit voltage. A high value of $V_{oc}$ is a sign of high-quality material with low recombination losses. The solar cell delivers zero power under both conditions corresponding to $V_{oc}$ and $I_{sc}$.

The optimal operating point of a solar cell corresponds to the maximum power point (MPP). The MPP is located at the point where the area of the rectangle under the I-V curve is largest. This point balances trade-offs between voltage and current, as an increase in load resistance increases voltage and decreases current, and vice versa. The corresponding voltage at MPP is called the voltage at maximum power ($V_{mp}$), while the associated current is known as the current at maximum power ($I_{mp}$). The solar cells or PV modules are required to be operated at the MPP to maximize the energy harvest. The following equation helps to calculate the maximum power:

$$P_{mp} = I_{mp} \times V_{mp} \qquad (3)$$

Another key performance metric in solar device characterization is the fill factor (FF). It quantifies the 'squareness' of the I-V curve and reflects how effectively the solar cell converts the available power into usable electrical power. Equation 4 is used for the calculation of FF. There is a common misconception that should be addressed, which is the notion that a perfectly efficient solar cell is expected to exhibit an FF of 100%. The diode-like behaviour of the solar cells makes it fundamentally incorrect. A constant photocurrent is generated within a solar cell during exposure to illumination; however, as the voltage increases, a rise occurs in the internal diode current, which, in turn, limits the net current output. The diode current and photocurrent cancel each other out at the open-circuit voltage, meaning that there is no flow of current. This inherent trade-off between current and voltage, dictated by the physics of recombination and carrier injection, reduces the FF to below 100%, even in ideal conditions (Wang, 2022). The quality of perovskite materials and transport layers plays a significant role in values for FF. For example, higher FF values can be achieved with well-defined grains with fewer grain boundaries, as they improve charge transport and reduce recombination (Kong et al., 2020). Furthermore, FF can be reduced due to the poor interface between the perovskite and transport layers.

$$FF = \frac{V_{mp} \times I_{mp}}{V_{OC} \times I_{SC}} \qquad (4)$$

Power conversion efficiency (PCE) is the most essential metric in evaluating solar cell performance, as it quantifies the effectiveness of converting incident solar energy into electrical power. The calculation of PCE can be performed via equation 5.

$$PCE = \frac{P_{out}}{P_{in}} = \frac{V_{OC} \times I_{SC} \times FF}{P_{in}} \qquad (5)$$

$P_{in}$ denotes the power of the incident light, which is 1000 W/m$^2$ under STC. PCEs are most expressed as a percentage (%). Although a high value of PCE means significant efficiency of a solar cell, it does not guarantee commercial success, as it does not capture the long-term stability, scalability or environmental resilience of the solar device.

The series resistance ($R_s$) is another notable parameter that characterizes the PSC devices, accounting for the resistive losses along the current path. These losses encompass the contributions from the transport layers, transparent conductive oxide (e.g., FTO or ITO), contact interfaces, and perovskite bulk resistance. The value of $R_s$ should be low to accomplish high device efficiency and effective charge extraction. Conversely, high values of series resistance result in drops in voltage within the device, which in turn leads to reduced FF and power output, particularly at high current densities approaching short-circuit conditions. A flattening or rounding of the curve near the maximum power point and short-circuit region in the IV curve is a sign of high series resistance (Figure 7). Material conductivity, layer thickness, and contact resistance are factors influencing $R_s$. Understanding and controlling $R_s$ in device characterization is essential for ensuring the PSC device scalability, reproducibility, and efficiency in both commercial and research applications (Baig et al., 2020).

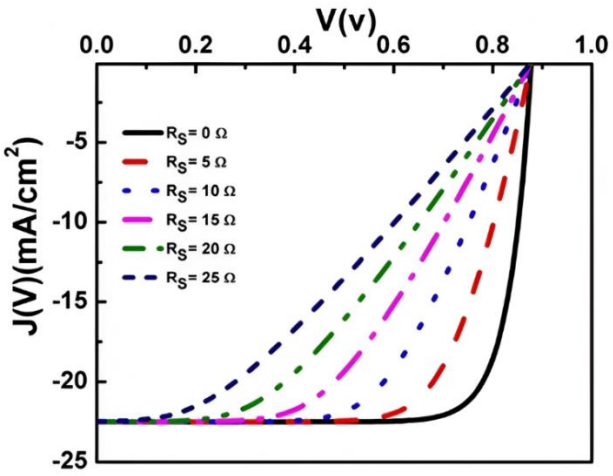


Figure 7. Impact of varying series resistance on the current density-voltage curve of a solar cell. Reprinted from (Ali et al., 2025), with permission from the publisher.

Shunt resistance ($R_{sh}$) corresponds to undesired leakage currents that bypass the active photovoltaic region. Defects such as poor interfacial contacts, pinholes, or contamination in the perovskite layer during fabrication are significant factors contributing to this type of resistance. High shunt resistance is essential, as it signals the minimized leakage pathways. Additionally,

high shunt resistance also means that the photogenerated current is effectively collected at the electrodes. The presence of detrimental leakage paths and poor film quality is indicated by a low shunt resistance. This, in turn, reduces device efficiency by decreasing the FF and reducing the $V_{oc}$, especially under low light or in the presence of high humidity, where the effect of shunt resistance is more severe. The presence of a lower shunt resistance in PV devices is evident as a steeper slope near the $V_{oc}$ in the current-voltage characteristic (Figure 8). Shunt resistance is highly susceptible to layer uniformity, material quality, and fabrication defects. It is a critical parameter in the quality and consistency assessments of PSCs, directly related to overall device performance and reliability (Singh and Ravindra, 2012).

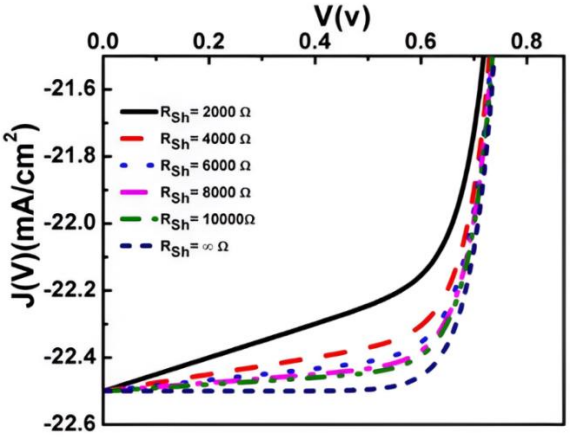


Figure 8. Impact of varying shunt resistance on the current density-voltage curve of a solar cell. Reprinted from (Ali et al., 2025), with permission from the publisher.

A current source connected in parallel with a diode could be presented to visually represent the electrical behaviour of ideal solar cells. The one-diode equivalent circuit (illustrated in Figure 9) as a model allows the impact of each element to be understood and quantified, as it is vital in interpreting the I-V characteristics.

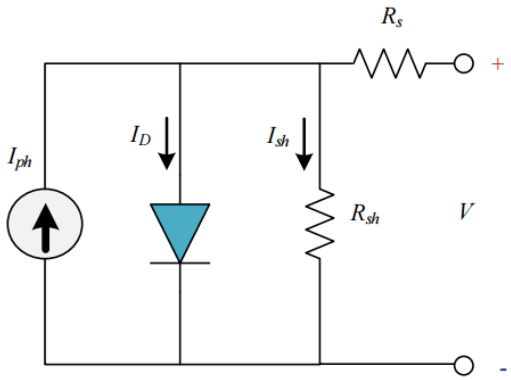


Figure 9. One-diode equivalent circuit model of a solar cell. Reprinted from (Khunchan and Wiengmoon, 2018) which is under the CC BY license.

A current-generating source, a diode, a series resistor, and a parallel (shunt) resistor are incorporated in this model. The current generated by the cell under illumination due to incident photons is symbolized by the photocurrent, $I_{ph}$. The recombination of charge carriers is captured by the diode current, $I_D$, that follows the Shockley diode equation and increases exponentially with the applied voltage. The current that flows through $R_{sh}$ is denoted by the shunt current, $I_{sh}$. The shunt resistance accounts for the leakage pathways across the device due to imperfect insulation or defects. In the case of a low value for $R_{sh}$, the presence of significant power loss is common. The resistive losses experienced by charge carriers as they move through the absorber material, transport layer, and metal contacts contribute to the series resistance. A high $R_s$ results in a reduction in both the FF and overall device efficiency of the solar cell. The externally measured voltage across the device under load is represented by the terminal voltage ($V$). Together, these parameters are essential in understanding the performance-limiting factors in PV devices and form the basis of the I-V equation. Equation 6 is the corresponding I-V equation and is essential in the loss mechanism diagnosis in solar cells. It incorporates the photogenerated current, the diode current, and the shunt current.

$$I = I_{ph} - I_d - I_{sh} = I_{ph} - I_0 \left[\exp\left(\frac{q(V+IR_s)}{nkT}\right) - 1\right] - \frac{V+IR_s}{R_{sh}} \qquad (6)$$

The diode leakage current in the absence of illumination is represented by the reverse saturation current ($I_0$). The Boltzmann constant is denoted by $k$, and $T$ represents the absolute temperature. The exponential diode term also includes the elementary charge ($q$). Finally, the parameter $n$ reflects the ideality factor in the solar cell I-V equation.

Another important method in solar device characterization is a dark I-V measurement, a method that refers to current-voltage characterization of solar cells in the absence of light. Dark I-V measurements reveal the inherent diode nature of the cell in comparison to illuminated I-V measurements. Non-photovoltaic properties that impact stability and efficiency and recombination mechanisms without the presence of light can be diagnosed with this approach, making it a particularly significant type of measurement. Various failure modes, such as degradation of the electrical circuit of the PV device, potential-induced degradation, and mechanical damage to solar cells, can be revealed with this type of characterization technique (Morales-Aragonés et al., 2021). Researchers can extract essential parameters, including shunt and series resistances, by implementing this method. The significance of dark measurements lies in their ability to identify defects in PSCs that contribute to hysteresis, a perennial challenge observed in perovskite materials. The contrast between dark and light I-V curves (illustrated in

Figure 10) suggests that the dark curve demonstrates a diode-like behaviour. Comparing dark and illuminated I-V curves can provide significant insights into how light affects charge generation and transport.

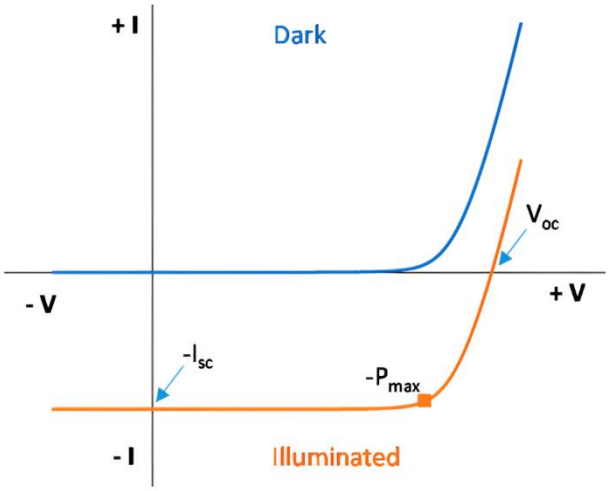


Figure 10. Comparison of dark and illuminated current–voltage (I–V) curves of a solar cell. Reprinted from (Morales-Aragonés et al., 2021) which is under the CC BY license.

## 2.4 Hysteresis Behaviour and Hysteresis Index

One of the serious challenges for the commercialization of PSCs is the phenomenon of hysteresis. This phenomenon is reflected in the I-V characterization, where the measured curve is dependent on the scan rate and direction. There are two common scan directions. In the forward scan, the voltage is swept from short-circuit to open-circuit, while the reverse scan is the voltage sweep from open-circuit to short-circuit. Ambiguities in device performance evaluation, especially in identifying accurate PCE, arise due to this inconsistency in I-V response, whose origins – i.e., whether it is intrinsic or extrinsic remain unclear. Normal and inverse hysteresis are two main types of hysteresis observed in PSCs. The PCE acquired in the reverse scan is higher than that of the forward scan in the normal hysteresis, whereas the opposite trend is observed in the inverse hysteresis (Figure 11) (Wali et al., 2022).

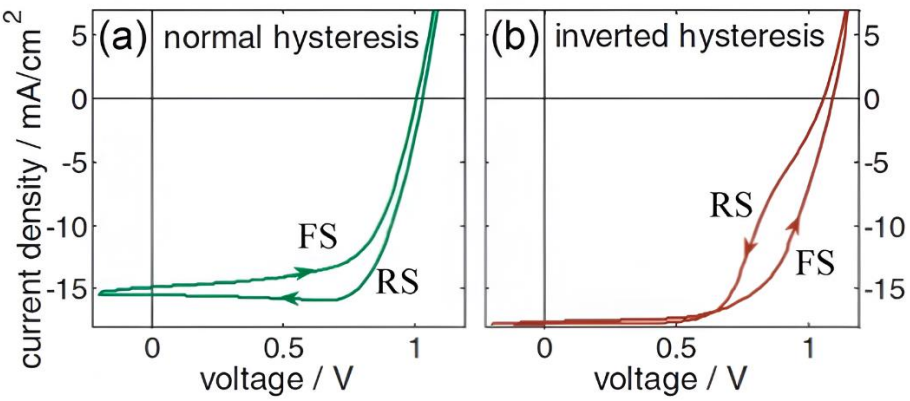


Figure 11. Visual representation of hysteresis behaviour in perovskite solar cells (PSCs) for (a) normal and (b) inverted variations. Reprinted from (Wali et al., 2022), with permission from the publisher.

The observed hysteresis in PSCs is affected considerably by whether the direction of the voltage scan is a forward scan or a reverse scan. Generally, the reverse scan demonstrates a higher current density and PCE in comparison to the forward scan in the case of normal hysteresis (Wali et al., 2022). The impact of the scan rate of the voltage sweep on the hysteresis in the I-V studies has been observed and explored in several studies, (Jacobs et al., 2017), (Rong et al., 2017). One particular study has investigated how the scan rate impacts hysteresis and reported that hysteresis is common within a certain range of scan rates, not being present outside of that specific range (Kim et al., 2017). Another notable study has compared the different scan rates, 10, 700, and 10 000 mV/s, and their impacts on the hysteresis (Huang et al., 2022). The pattern of hysteresis acquired resembled a pattern of a Gaussian distribution as a function of scan rate in the study. Hysteresis was minimal at low scan rates, increasing steadily with higher scan rates, eventually reaching a maximum at nearly 700 mV/s. Researchers reported a decline in hysteresis beyond this point. Weak hysteresis at lower scan rates can be linked to the complete redistribution and accumulation of mobile ions, which allowed for quasi-steady-state conditions at the device. Furthermore, ions failed to dynamically respond to the rapidly changing electric field, thereby minimizing the degree of hysteresis in the I-V measurement.

The perovskite's chemical composition and physical structure also strongly influence the extent of hysteresis. Ion mobility and defect densities can be altered by different cations, such as methylammonium, formamidinium, cesium and halides. For example, $MAPbI_3$ demonstrates stronger ion migration and higher hysteresis compared to triple-cation perovskites (Bulloch et al., 2022). The enhanced phase stability and reduced defect states are credited for this reduction, limiting ion movement and interfacial recombination. The ionic hysteresis is also affected by the physical structure of the perovskite layer, specifically grain size and morphology. The

number of grain boundaries that serve as pathways for ion migration decreases due to the larger grain sizes. This culminates in weaker hysteresis. The activation energy for ionic migration has been increased by an increased grain size in $MAPbI_3$ films in one particular study, achieving a weakened hysteresis (Singh and Parashar, 2020). Hence, the device performance can be improved by optimizing the grain size and morphology of the perovskite layer. The configuration of the solar device also leaves an impact on the degree of hysteresis. The device architecture of p-i-n often leads to lessened interfacial ion accumulation with organic transport layers, thereby achieving negligible hysteresis in comparison to n-i-p structures.

The hysteresis phenomenon in the PSC systems is generally attributed to several factors, such as ferroelectric polarization, ion migration, trapping, and de-trapping of the carriers at the interfacial faces (Minbashi and Yazdani, 2022). Ferroelectric properties of PSCs, which are proposed as a contributing factor to hysteresis anomalies in I-V curves, allow for the spontaneous electric polarization that is reversible by an external electric field. The dipolar methylammonium (MA) cations in PSCs, such as $CH_3NH_3PbI_3$, have an ability to align under an applied electric field, which, in turn, leads to a polarization capable of impacting transport and recombination of charge carriers. The I-V curves for forward and reverse scans could differ due to the scan direction-based reorientation of dipoles, culminating in hysteresis (Li et al., 2021).

Ion migration within the perovskite layer is one of the main contributing factors to the hysteresis in PSCs. As the perovskites belong to the category of mixed ionic-electronic conductors, ions such as halide anions and organic cations freely move under the effect of electric fields. These mobile ions drift towards the interfaces with the transport layers in the duration of I-V characterization measurements. This results in the accumulation of ions at the interfaces between the charge transport layers (electron transport layer and hole transport layer) and the perovskite layer. The internal electric field distribution inside the device is altered by this resulting space charge regions, affecting the extraction and recombination of photogenerated charge carriers. Ultimately, this results in different I-V curves for forward and reverse scans. It has been reported in a particular model to characterize the PSC behaviour that the role of ion migration, along with charge carrier recombination, is significant in the occurrence of hysteresis. According to the simulations, in the absence of recombination, I-V curves have demonstrated hysteresis-free behaviour with mobile ions present. However, the internal electric field is altered by the ion accumulation when the recombination, especially at interfaces, is

significant. This alteration leads to changes in charge carrier dynamics, leading to hysteresis (Yang et al., 2020).

Trapping and de-trapping of charge carriers are another significant contributing factor to the hysteresis anomaly. This typically occurs at the interfaces with charge transport layers, involving ETL and HTL, and at grain boundaries within the perovskite absorber. Charge carriers could get immobilized at trap states positioned at these interfaces. Progressively, this hinders charge extraction and creates space charges that modify the internal electric field, influencing charge transport and recombination, ultimately resulting in hysteresis. Shallow trap states near interfaces are capable of screening electric fields, leading to hysteresis, which has been observed in device simulations by a recent study (Veurman et al., 2024). Experimental studies have also confirmed the role of interfacial and de-trapping in hysteresis. Evidence acquired from infrared optical activation spectroscopy shows a two-step trap-filling behaviour in PSCs. The first step involved rapid filling of bulk traps, which is followed by slower accumulation of high-density traps at the perovskite/HTL interface, highlighting the impact of interface traps on hysteresis (Pan et al., 2023). The significance of trap management is also clear in the lead-free PSCs, as typically observed higher levels of defects and ion mobility exacerbate hysteresis (Dixit et al., 2022). It is feasible to mitigate trap-related hysteresis by following strategies that implement defect passivation with additives (e.g., β-phenylethylammoniumiodide) or interface engineering (Sha et al., 2023).

Researchers have defined several quantitative metrics to assess the degree of hysteresis in the current-voltage characteristics of PSCs. One of such metrics is the Hysteresis Index (HI), enabling comparison across different devices, fabrication methods, or measurement conditions. It can be calculated with Equation 7:

$$HI = \frac{PCE_{rv} - PCE_{fw}}{PCE_{rv}} \qquad (7)$$

In the equation, PCE obtained from the reverse scan is represented by the $PCE_{rv}$, while the $PCE_{fw}$ denotes the PCE from the forward scan. Equation 7 enables the calculation of a standardized metric to evaluate the PCE variation between scan directions, with higher HI values corresponding to more severe hysteresis. A key advantage of using the HI index is its capacity to provide a quantitative comparison, allowing scientists to evaluate hysteresis across different architectures or studies. It should also be mentioned that it is an accessible metric for both theoreticians and experimentalists, as it offers ease of use, being straightforward to

calculate and interpret. Despite it benefits, there are several limitations that come with the use of HI, specifically for lead-free PSCs that demonstrate variable extents of hysteresis. One of the limitations is its inability to provide comprehensive physical insight. It is difficult to identify the underlying causes of hysteresis, as HI only quantifies the difference in PCEs from distinct scan directions. Therefore, its use for understanding device physics is limited, as it is a descriptive metric rather than an explanatory one. The dependency on measurement conditions, including scan rate, light intensity, and pre-bias voltage, is another notable limitation of HI. For example, the scan rate can have a drastic impact on HI, as slower scan rates lead to lower HI, while higher HI values are observed in faster scan rates. It is possible to achieve low HI in a highly hysterestic cell by implementing a very slow scan rate. Therefore, the precise experimental conditions should be reported to ensure the relevance of the HI value. Furthermore, HI does not capture variations in other important parameters, such as FF, $V_{oc,}$ and $J_{sc}$, as it is solely based on the difference in PCE values. Based on these limitations, the HI index has been criticised by the researchers (Habisreutinger et al., 2018).

## 2.5 Role of Automation in PSC Research

The discovery of the enhanced perovskite materials for solar PV applications necessitates the exploration of a large parameter space that covers the possibilities in fabrication methods, surrounding conditions, PSC structures, and compositions. The rate of material discovery can be accelerated with a rapid combinatorial screening of this parameter space. Simple lab-scale deposition methods and characterization techniques have been the most preferred choices in material discoveries and optimization processes associated with PSCs during the last decade. This implementation has substantially slowed the rate of progress in the field of PV due to the time-consuming and labour-intensive nature of these methods, driving the emergence of high-throughput experimentation (HTE) as a transformative alternative. HTE corresponds to the systematic strategy of rapidly synthesizing, processing, and characterizing a broad array of device configurations and material compositions. Automation, robotics, and advanced data analytics have been frequently incorporated into this methodology, which is of great assistance in the discovery and optimization of PSC materials. Experiments can be performed in a parallel way by referring to HTE. This has the potential to drastically reduce the time and effort required from researchers involved in conventional methods.

One particular study has introduced a custom-built, high-throughput system capable of characterizing 16 solar cells simultaneously (Surmiak et al., 2020). The reproducibility and

accuracy have been ensured with the integrated standardized protocols, parallel measurements, and real-time data acquisition. External influences, including temperature and humidity, have been controlled with the use of a motorized stage and precision alignment tools in the setup. A custom sample holder with magnetic lids has been employed to ensure electrical contact with solar cells. This, coupled with automated deposition methods, achieves the required uniformity in device fabrication. Contact resistor errors have been minimized with the implementation of a 4-wire sense measurement technique. Customizable measurement protocols, including dynamic I-V scans and pre-conditioning steps, have been introduced in the study. A major achievement of this study is the time reduction in the measurements by 50 min.

Another research study has introduced a new HTE framework for PSCs (Starkholm et al., 2023). Researchers have leveraged a fully automated robotic system to facilitate the discovery rate of perovskite-based materials. Synthesis, characterization, and solar cell testing have been combined into a single workflow in the proposed framework. The integration of autonomous robots into solar cell characterization is the novel feature of this work. The robot was capable of autonomously performing solution mixing, in-situ Raman spectroscopy, X-ray powder diffraction, and solar cell characterization. The characterization of $MAPbI_3$ performed in the study proves its capabilities to handle materials susceptible to oxygen and moisture. During the experiment, several PSC-based devices have been identified by implementing this framework. The discovered materials were the low-dimensional perovskite [QR][$PbI_3$] and the combination of cationic dye (NIR-Luci) and $PbI_2$. A full screening and characterization cycle of a single sample can take around 35 min, with the use of the robotic system. According to the published study, the robot can perform the assessment of 50 reactions in a single day, which is described as a non-realistic task for a human being.

To address the challenges in the design, prediction, and optimization of new materials, the possibility of integrating machine learning algorithms has been explored. One of the successful integrations of such methods in PSC research has been the inclusion of Bayesian optimization, owing to its effectiveness in high-dimensional spaces. For instance, the composition of $Cs_xMA_yFA_{1-x-y}PbI_3$ has been enhanced, and a new stable halide perovskite has been discovered with the implementation of Bayesian optimization (Sun et al., 2021). It is also common to see the combination of machine learning approaches and robotic systems to accelerate material development in PSCs. One of the studies has integrated an automated spin-coating system with Bayesian optimization to simultaneously optimize the composition of the perovskite precursor solution and process conditions (Eguchi et al., 2025). The concentrations of methylammonium

chloride (MACl) and lead iodide ($PbI_2$) in the precursor solution, the maximum coating speed, and the annealing temperature of the perovskite layer were the parameters that were aimed to be optimized, requiring the exploration of a vast parameter space involving 17,901 possible combinations. During the study, PSCs were prepared by a previously developed spin-coating system. Substrate transport, spin-coating, antisolvent dropping, and substrate heating are automated in this employed system. The human factors that could account for possible variations in device performance were also minimized. The system regulates the timing of the antisolvent drop during spin-coating. It also controls the transition period before the device is transferred to the hot plate for annealing. Reliable datasets with low variability are ensured with this automated approach. This created a perfect environment for training and validating machine learning methods (the fabrication system is illustrated in Figure 12).

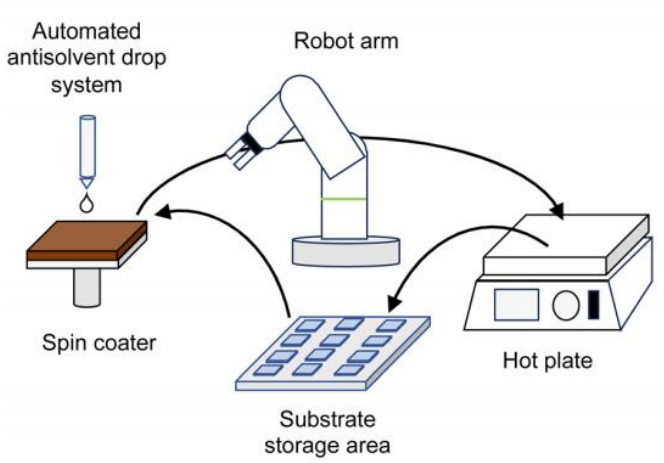


Figure 12. Schematic representation of the automated spin-coating setup used for the PSC film fabrication. Reprinted from (Eguchi et al., 2025), which is under the CC BY license.

The achievement of the employed method was an increase from the manually optimized PCE of 20.5% to 21.4% with the material with the same composition. This was accomplished with 51 combinations, which constituted 0.36% of the total parameter space, showcasing the used approach's ability to quickly reach optimal conditions with minimal repetitions. The optimized device also exhibited a longer carrier lifetime, as revealed by time-resolved photoluminescence spectroscopy. The optimized conditions led to better interface quality and PV performance parameters due to the enhanced film quality. This signifies the capability of machine learning-inspired automated systems to reduce the time involved in conventional characterization methods and accelerate the high-efficiency material development in PSCs.

## 2.6 Existing Data Analysis Tools and Their Limitations

Researchers in PSC research have traditionally relied on manual methods for data analysis. The common tools include Microsoft Excel and Origin, developed by OriginLab. Their flexibility and accessibility are the main reasons behind their popularity among researchers whose tasks include initial solar data processing and visualization. These tools enable researchers without specialized programming skills to evaluate the performance of devices. Data entry, organization, simple calculations, and visualizations are the main tasks that these tools tackle, assisting researchers in performing initial data analysis and making basic statistical analysis.

Excel is a popular tool utilized by researchers in various fields, which is recognized for its capacity to process data in tabular form, make simple calculations, and generate preliminary visualizations. Researchers who are unfamiliar with coding practices can refer to Excel to organize and process raw data to derive essential PV parameters. Excel also allows scientists to create basic plots for the evaluation of device performance. The Perovskite Database Project, compiling data from over 42,400 PSC devices, is a prominent example using Excel software, as it has developed an Excel template to ensure standardized collection of data (Jacobsson et al., 2021). This template ensures consistency across experimental datasets, as it facilitates data entry and reporting, is freely available, easy to use, self-explanatory, and extensible. Excel also offers the use of built-in formulas and macros, which could be used to automatically calculate the PV metrics. Thanks to Excel's flexibility, scientists can perform management and comparison of data acquired for devices, making it particularly significant in PSC research, where multiple measurements are required to overcome stability challenges.

Origin is a specialized visualization and analysis software. It enables scientists and researchers to perform data fitting and generate advanced plots, making it a widely used tool in scientific research. Origin is widely used in materials science and solar cell research, allowing for the generation of high-quality visualizations, such as plots and curves for the assessment of PSC performance. This software tool is a popular option for experimental data analysis for the extraction of essential PV parameters for domain experts lacking programming expertise due to its advanced features, such as curve fitting, statistical analysis, and data smoothing.

In spite of Microsoft Excel and Origin's prevalent use in PSC research, users experience notable limitations when referring to these tools for manual data analysis, which impedes scalability, efficiency, analytical depth, and data integrity. As the worksheets in Microsoft Excel have a limited size with a maximum of 1'048'576 rows and 16'384 columns, it is intrinsically limited

in working with large datasets (“Excel specifications and limits,” 2025). The performance of Excel can drastically degrade in the case of extensive experimental data, which is commonly experienced in high-throughput PSC studies. This decrease in performance can lead to slow data processing and potential system crashes. Researchers also find the manual data entry and analysis in Excel and Origin time-consuming and labour-intensive. Scientists have to dedicate significant manual effort to tasks, such as inputting raw data, making calculations, and generating compelling visualizations, which could become highly burdensome when dealing with numerous datasets originating from stability measurements. This manual approach significantly influences researchers’ ability to quickly iterate and explore various analytical perspectives, slowing down the research process. It is also difficult to achieve an in-depth exploration of complex datasets with Excel and Origin, as they do not incorporate the advanced analytical tools for solar data. The sophisticated statistical analysis techniques for solar data are not supported in these tools, limiting their potential to support researchers in identifying patterns and correlations in PSC research.

The need to deal with large datasets and standardize solar data analysis stimulated the emergence of community scripts with a goal to reduce the burden of manual analysis done by researchers. They are often hosted on platforms such as GitHub, fostering collaboration and reproducibility. These open-source tools is that they enable individuals to use, modify, and contribute to the projects through repositories or collaborative platforms. One such project is the Perovskite Database Project, which was launched in 2021 (Jacobsson et al., 2021). Its design adheres to the FAIR (Findable, Accessible, Interoperable, Reusable) data principles. It has an open-access repository and is a flagship initiative that has compiled extensive data from over 42’400 perovskite-based solar devices and covers up to 100 parameters per device. The metadata, process data, and performance data are included in the data extraction protocol followed in this open-source database (data categories involved in the Perovskite Database are illustrated in Figure 13).

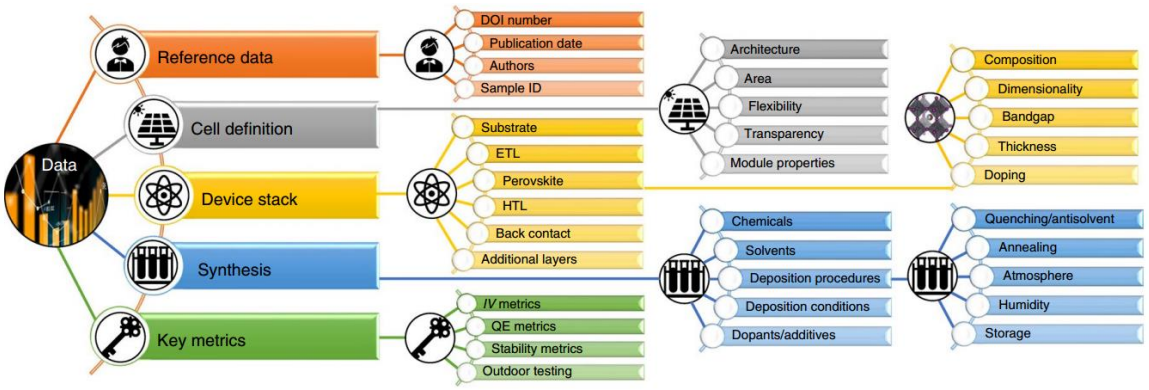


Figure 13. Visual summary of the main data types extracted in the Perovskite Database. Reprinted from (Jacobsson et al., 2021), which is under the CC BY license.

One example use case of this tool is to track the perovskite solar cell development, which is illustrated as a Hexbin plot of PCEs achieved as a function of publication date for devices present in the database (Figure 14). The scripts for data cleaning, statistical analysis, and visualization are provided in the project, encouraging researchers to leverage standardized and reproducible research practices. Customizability is one of the major benefits of using this database. Dynamic filters are integrated in this database, allowing researchers to categorize findings based on specific criteria, such as device configuration, processing technique, or material composition. PSC specialists lacking programming training readily visualize the performance trends under defined constraints, which can then be downloaded and used.

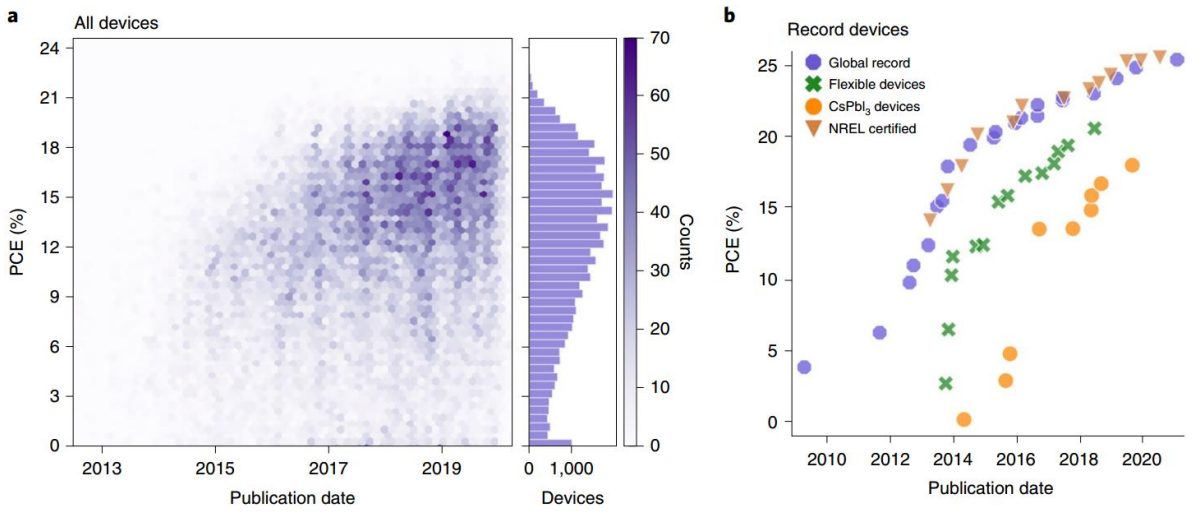


Figure 14. Example uses from the Perovskite Database. (a) Hexbin plot demonstrating the distribution of PCEs acquired under STC over time, with a corresponding efficiency histogram included on the right. (b) Progression of peak efficiency values over time achieved in PSCs, showcasing results for flexible and $CsPbI_3$-based devices, accompanied by NREL data for comparative evaluation. Reprinted from (Jacobsson et al., 2021), which is under the CC BY license.

Perovskite-miner is another worth-mentioning open-source AI-powered tool developed at Helmholtz-Zentrum Berlin (Zeevy and Burmistrov, 2023). Its main aim is to help researchers

extract performance data from perovskite research papers, offering a solution to streamline data collection and database population. Based on the natural language processing techniques, this tool has a goal of keeping the Perovskite Database up to date with the latest scientific findings. The provided continuous input of recent data can assist the Perovskite Database, potentially being the driving force behind its future progress. Furthermore, another community-developed tool is 'pvlib' library developed in Python (Will Holmgren et al., 2025). Providing accessible, reliable, interoperable, benchmark implementations of PV system models is the primary mission of this tool. While not specifically developed for PSCs, the performance of PV energy systems can be stimulated with a set of functions and classes included in this tool. Included functions allow for solar position calculations, irradiance modelling, and system loss modelling. Moreover, an open-source MATLAN-based software introduced in 2022 – IonMonger 2.0 – can be used by researchers (Clarke et al., 2022). It is a drift-diffusion model particularly designed for the simulation of ion migration and charge carrier transport in planar PSCs. ETL, HTL, and perovskite absorber layer can be explicitly modelled in one spatial dimension in this tool. Electric potential, halide ion vacancies within the perovskite layer, electrons within the ETL and perovskite layers, and holes within the perovskite layer and HTL are the model variables. Various experimental protocols can be stimulated in IonMonger 2.0. This includes changes in applied voltage and intensity of illumination over timescales spanning from microseconds to hours. I-V curves can be plotted with the outputted current and voltage data, and the hysteresis occurring due to halide ion movement can be analysed. Impedance spectra can be simulated, and the effects of selected material properties can be analysed. One of the limitations of this tool is that it is particularly tailored to planar PSCs, meaning that it might not be useful for researchers dealing with other PSC architectures. Scope limitation, as observed in IonMonger 2.0, is a major disadvantage of community scripts, as they mostly focus on specific tasks, having limited applicability to broader research areas. Moreover, some researchers, especially specialists unfamiliar with coding practices, may experience limited accessibility if the proposed tool does not have a user-friendly interactive interface. Furthermore, the long-term functionality of community-developed projects is uncertain, as they are dependent on the community's efforts. Inactive maintenance in such projects can lead to compatibility issues.

To support the specialists in solar cell research, several commercial data analysis tools have been developed to handle the complex datasets obtained from experimental measurements. These tools typically provide automated, standardized, and reproducible analysis. These solutions stand out with their professional customer support and sophisticated functionality,

which are valuable across academic and industrial settings, in contrast to open-source or community-developed alternatives. The SETFOS and PVSyst are prominent commercial tools, particularly relevant to data analysis of lead-free PSC data.

SETFOS, which is developed by Fluxim is a commercial software tool that is popular in both academic and industrial settings ("Setfos," 2025). Similarly, PVsyst is a commercial software platform renowned for its accuracy. PVsyst frequently appears in research, analysing both stand-alone and grid-connected systems (Kumar et al., 2021; Mishra et al., 2024). Thanks to its functionalities, PVsyst stands out as a reliable tool to identify performance bottlenecks in PSC-based solar modules, as demonstrated in a recent study of a module of $CH_3NH_3SnI_3$ (Hanif et al., 2024).

Although commercial options have notable benefits, they also present critical limitations that hinder widespread adoption among researchers. One of the constraints is the cost associated with the usage of licensed tools. Moreover, adapting to commercial platforms and working with their advanced features could require additional training. In addition, the developers of such platforms often restrict access to the source code, which limits opportunities for customization or integration of other useful functionalities to adapt to new methodologies. Finally, in the context of PSC research, such tools often lack dedicated models and relevant analysis methods.

## 2.7 Novelty

The progress in the tools and methodologies for analysing PSC-related data still relies on manual or semi-automated processes. Overcoming these challenges is essential for facilitating innovation and attaining the full potential of PSC technologies.

This thesis presents a novel automated software tool. The developed platform is designed to overcome gaps in perovskite-based solar PV cell data analysis workflows. The proposed work bridges this important gap through the development of a robust platform to address the complex demands of PSC research. The unique contribution is the automated data analysis pipeline from importing raw measurement data to acquiring PV performance parameters. Based on the input data, the software is built to generate key visualizations to offer researchers critical insights into the consistency and distribution of device efficiency across samples and architectures. A report is the final product of the data processing framework.

This thesis delivers a new tool to the field of PSC data science by offering an accessible platform developed for PSC research.

# 3 Materials and Methods

## 3.1 Device Architecture Overview

The software was designed to process the data derived from PSCs with n-i-p device configuration. It has a standard layer order, including ETL, perovskite absorber, and HTL (Figure 4). The calculation and analysis methods in the introduced tool were based on this structure.

This involved PSC devices that possess 2 and 8 active areas. The benefit of these multi-pixel configurations is that they help researchers to make simultaneous or independent measurements of multiple sub-cells on a single substrate, delivering insights into PV performance metrics.

A 2-pixel PSC device consisted of a transparent substrate, typically glass, coated with a transparent conductive oxide (TCO) such as fluorine-doped tin oxide (FTO), and two active areas (pixels) (Figure 15). Each pixel area was designed to operate as an independent solar cell for separate measurements. Upon illumination, each pixel would produce a photocurrent based on the incident light intensity and the material properties of that specific area. This enables researchers to evaluate variations in performance within the same substrate of the device.

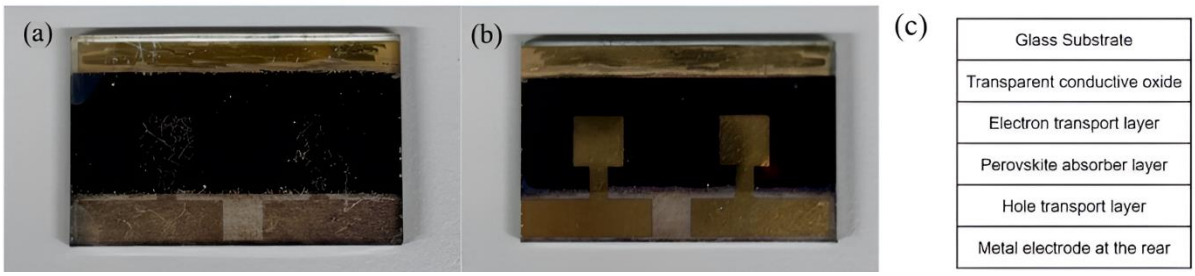


Figure 15. Photograph of a fabricated two-pixel n-i-p structured perovskite solar cell; (a) Front view, (b) Back view, (c) its constituting elements. The dark region in the front view is the perovskite absorber layer stack, which includes transparent conductive oxide, ETL, perovskite layer absorber, and HTL. The current collection is enabled by the gold top contacts that are deposited on top of the HTL. The back view also includes gold contacts. ‘’T’-shaped gold pad in back view connects to each pixel. Each half of the substrate corresponds to an individual pixel.

The 8-pixel PSC device incorporated eight individual active areas on a single substrate to enable efficient high-throughput testing. Its design is similar to that of a 2-pixel device, on an FTO-coated glass substrate. The 8-pixel architecture is especially beneficial when utilized with advanced measurement systems, such as using Fluxim Litos Lite which supports multi-channel measurements. This allows for the simultaneous measurement of 8 pixels in a single run. Robust performance metrics can be obtained by averaging or comparing results across the eight pixels.

## 3.2 Data Acquisition

The I-V data obtained by measuring 2-pixel devices was imported into a standardized Excel template, which was subsequently used for parameter extraction. The data was acquired using the Abet 10500 solar simulator, which incorporates a fast F/1 optical system with a rear reflector to effectively collect radiation from the lamp (Figure 16).

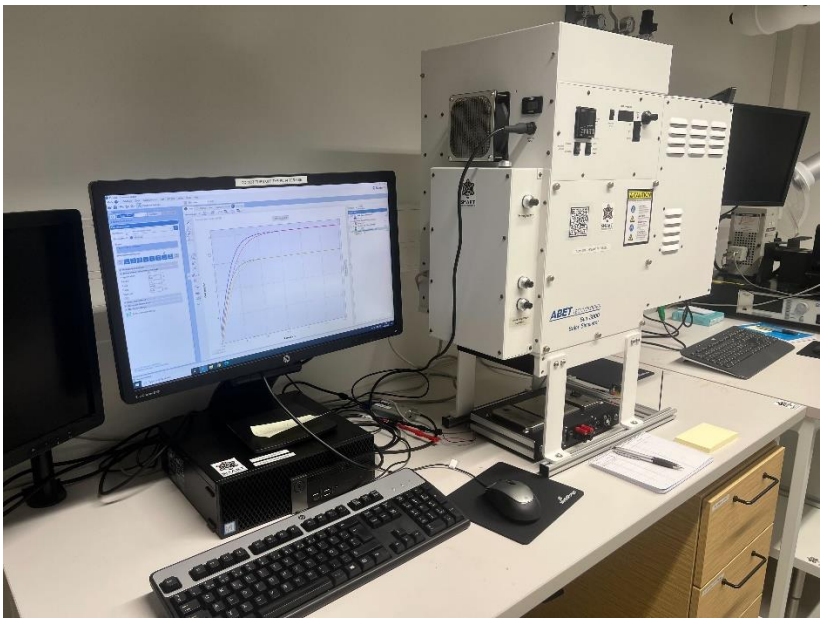

Figure 16. Setup of the Abet 10500 solar simulator utilized for PV characterization.

The instrument also includes a holder with a mask designed for a 2-pixel solar device (Figure 17).

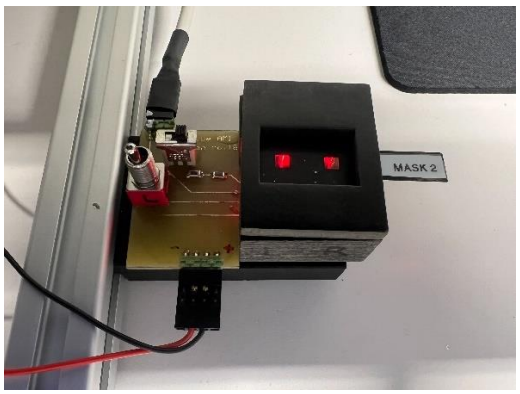


Figure 17. A sample holder with a mask used in I-V measurements of 2-pixel devices under Abet 10500 solar simulator. The exposed windows are marked by the red glowing areas, places where the light from the lamp is directed onto the active area of the solar cell. Regarding the connectors, the red and black wires maintain the connection to the positive and negative terminals of the solar cell, respectively, feeding the current to or from a source-measure unit during measurements. The 'L' label corresponds to the 'left' pixel of a 2-pixel device and indicates a particular test channel.

A solar cell and mask are mounted on the metallic base, holding them in a fixed position under the light source. Only a defined area of the solar cell is exposed to illumination with the incorporated mask, which isolates pixels for sequential testing. As masks limit the exposed area, they ensure the consistent illumination and accurate measurement of the cell's performance.

For the 8-pixel device characterization, the Fluxim Litos Lite was used to perform parallel I-V and stability measurements (Figure 18a). This device is well-suited for high-throughput testing of multiple-pixel devices, as it offers simultaneous I-V and stability measurements of 8-pixel perovskite solar cells. Stability testing in this device is in accordance with the International Summit on Organic Photovoltaic Stability (ISOS) protocols. This device is capable of controlling the temperature of the samples from 20 to 85 °C. The device also includes a custom sample holder (Figure 18b). The employed sample holder enables the measurement of 4 different 8-pixel samples, and it includes environmental sensors that allow the tracking of temperature and humidity in real-time. The thermal pads are incorporated into the system to achieve temperature uniformity. The instrument is operated via user-friendly software.

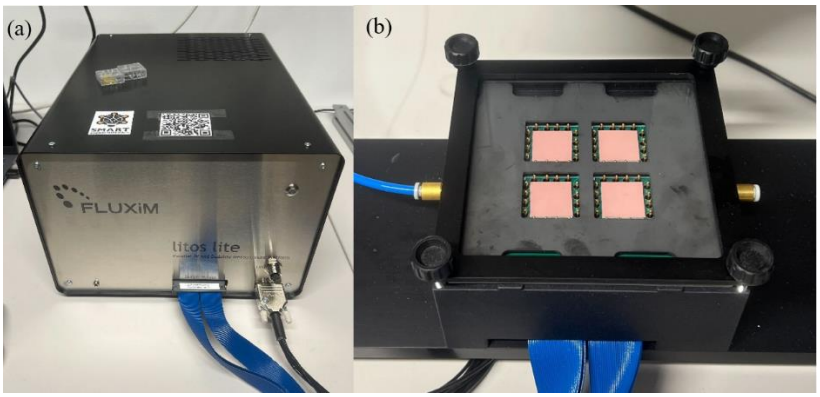


Figure 18. The Fluxim Litos Lite measurement platform. (a) The main device unit for parallel I-V and stability measurements. (b) Sample holder designed to accommodate 4 different 8-pixel samples.

Fluxim Litos Lite was connected to Wavelabs Sinus 70 LED-based solar simulator (Figure 19), with the ability to simulate the necessary solar spectrum for PV measurements. According to IEC 60904-9, this device is classified as A++AA+. The instrument leverages LED technology for the illumination source, which enables it to preserve a constant emission spectrum at the same level over time by regulating the output with an included photodiode and spectrometer. This is particularly advantageous for extended experiments, as it offers long-term stability and minimal maintenance in comparison with a regular xenon lamp simulator. This tool ensures high spectral accuracy and uniformity across a 5x5 $cm^2$ illumination area. The output of the solar simulator is stabilized by a PID controller, which, in turn, prevents the aging experiments

from being influenced by the changes in the illumination. These properties make this device an option for long-term stability and performance measurements of the PSCs. The users can utilize Litos Lite software to regulate this solar simulator. The light intensity and spectrum can be tuned by the user by using the Litos Lite software.


Figure 19. Setup integrating the Wavelabs Sinus 70 solar simulator with the Fluxim Litos Lite measurement platform.

### 3.3 Data Structure

To ensure efficient processing, the data structure for 2-pixel PSC devices was organized using an Excel template specifically designed to store the data (named ‘2-Pixel Measurement Template’). It is placed in the ‘2-Pixel Device’ folder under the ‘Data’ folder. The Excel file included multiple sheets, each referring to a particular measurement scan of a given side of the sample, allowing for comprehensive tracking of measurements. The naming convention of the sheets was developed based on a systematic pattern, which indicates the sample number, pixel location, and scan direction. The first sheet of the Excel template is ‘1-l-fw’, where ‘1’ corresponds to the first sample, ‘l’ represents the left pixel, and ‘fw’ means that the measurement was done in forward scan. ‘1-l-rv’ is the following sheet of the Excel template, which stores the data for the reverse scan for the left pixel of the first sample. The remaining sheets for the first sample were ‘1-r-fw’ and ‘1-r-rv’, capturing the data for forward and reverse scans for the right pixel of the sample, respectively. This method captures all four scan variations (left/right, forward/reverse) in a sequential order. The naming convention follows this pattern for other samples, with the second sample named ’2-l-fw’, ’2-l-rv’, ’2-r-fw’, and

’2-r-rv’, and so forth. The template includes 100 measurement sheets with 4 scans per sample, attaining a robust dataset to assess the stability and performance of the 2-pixel devices. If the measurements include samples more than 25, additional sheets should be manually generated based on the predefined naming conventions, including identical structures and formulas as previous sheets.

The I-V measurement data for 2-pixel PSC devices should be fit into the appropriate sheet based on the predefined naming conventions. For example, users should enter the data corresponding to the fourth sample’s right pixel under the reverse scan into the sheet named ‘4-r-rv’. The data for each sample, pixel, and scan direction is correctly organized for the following analysis by the software to maintain consistency and clarity across all sheets. The sheets possess multiple columns. ‘VOLTAGE (V)’ in the B column and ‘CURRENT (µA)’ in the C column are columns where the users should enter the data with the appropriate units – volts for voltage and microamperes for current. It is also required from the users to enter the cell area in the cell of N4, which refers to the active area of the measured pixel in square centimetres. The cell area value entered in cell N4 of the first sheet is copied to the identical cell in all remaining sheets, preventing the repetitive manual entry for cases where the cell area is the same across measurements. The value in cell N4 should be manually changed in the corresponding sheet if a particular test has a different cell area. The only inputs required from the researchers are voltage, current, and cell area. Essential I-V parameters, such as current density and power density, will be automatically calculated with built-in functions in the Excel template, once these parameters are entered. The explained process should be repeated for each P-V test. This ensures that data from all measurements is correctly placed across the forward and reverse scans for the left and right pixels. After entering all the necessary data, a copy of the Excel file under a different name should be saved to preserve the structure of the template, ensuring the continued accessibility of the Excel template. Once the file with test data is ready, it can be processed.

The software used to operate the Fluxim Litos Lite systematically organizes the output data structure for 8-pixel PSCs, facilitating the high-throughput analysis. A primary ‘devices’ folder is generated by the Litos Lite software once the measurement is completed. Multiple subfolders corresponding to a specific sample and pixel are created within this folder. The subfolders follow a standardized naming convention. The structure of the subfolder names can be indicated with ‘sample name[pixel number]’. Users are able to customize the sample names. The pixel numbers are enclosed in square brackets, ranging from 1 to 8, since the device is capable of

performing parallel measurements on 8 pixels. For instance, a folder named ‘sample 3[4]’ would indicate the subfolder that contains the data for the fourth pixel of the sample named ‘sample 3’. Users can easily identify the data for each pixel of a given sample due to the distinct separation of files based on this hierarchical organization.

The measurement data contained under each subfolder within the ‘devices’ directory is saved in CSV format. For each I-V measurement, the software generates two distinct CSV files per pixel. The naming of the CSV files indicates the measurement type, as different measurements are possible with Fluxim Litos Lite. For example, the ending of the CSV filenames is ‘Stressing’ for the stress testing measurements. The I-V measurements are indicated by the ending of ‘Perform Parallel JV’. The CSV files follow a naming convention that indicates the origin of the data. The used convention is ‘[sample name][pixel number]_(order number in the measurement sequence)_(number of the CSV file)_(Measurement type)’. For instance, results for the second pixel of the sample named ‘sample’ in the case where I-V test is the first measurement would be indicated with names ‘sample[2]_0_0_Perform Parallel JV’ and ‘sample[2]_0_1_Perform Parallel JV’. The first CSV, which has 0 before ‘Perform Parallel JV’ in the name, contains the raw I-V data and the sample area of the solar cell. This file also includes the metadata such as start voltage, stop voltage, scan rate, settling time, scan direction, light intensity, holder humidity, and temperature. Notably, if a measurement includes both forward and reverse scan directions, there will be a marker – NaN value – in both current and voltage columns around the middle of the dataset, indicating the change in scan direction. Alongside the metadata, a pre-calculated performance table is provided in the second CSV file, which is distinguished by a 1 before the measurement type in the naming. The performance table includes essential PV parameters, including $V_{mp}$, $I_{mp}$, MPP, $V_{oc}$, $I_{sc}$, FF, HI, and PCE. Although it is required to compute shunt and series resistance values separately, the parameter extraction effort is significantly reduced in the software with pre-calculation. Once PV measurements are performed with Fluxim Litos Lite, users are required to provide the file path to the ‘devices’ folder to enable the software to locate CSV files for each pixel across all samples.

## 3.4 Software Development

The Windows 11 Operating system was selected to develop the software for processing and analysing PSC data. Thanks to its rich ecosystem of scientific libraries, ease of integration with data handling workflows, and active community support in photovoltaic research, the primary

programming language was decided to be Python. The utilized Python version was 3.12.3, which includes modern features, improved performance, and stability. This version guarantees a robust development environment suitable for the complex requirements of PSC research. Due to its extensive support for Python development, Visual Studio Code was chosen as the primary text editor. This text editor offers a broad range of extensions to enhance code quality and productivity. To achieve a clean and isolated development setup, venv was utilized to create a virtual environment to manage project-specific dependencies.

The used Python libraries are grouped based on their primary purpose in the project (Table 2). Each library played a key role in building functionalities, including data processing, visualization, GUI development, and report generation.

Table 2. Python libraries categorized by their purpose in software development for PSC data analysis.

| **Purpose** | **Library/Module** | **Description** |
|---|---|---|
| GUI Development | messagebox, tkcalendar (DateEntry), tkinter (as tk), PIL (Image, ImageTk), filedialog | Libraries for building message pop-ups, date selection, graphical user interface, image handling for user interaction, and enabling file dialogs |
| File and Path Handling | os, platform, subprocess, openpyxl (load_workbook), pathlib (Path) | Libraries for file operations, system information, executing subprocesses, reading Excel files, and path manipulation |
| Data Processing and Analysis | numpy (np), pandas (pd), scipy (stats), re, io (StringIO), collections (default-dict), typing (List), dataclasses (dataclass) | Libraries for numerical computations, data manipulation, statistical analysis, and data structures |
| Plotting and Visualization | matplotlib.pyplot (plt), seaborn (sns) | Libraries for creating plots, involving I-V, P-V curves, and boxplots |
| PDF Report Generation | reportlab.pdfgen (canvas), reportlab.lib.pagesizes (letter, A4), reportlab.platypus (Table, TableStyle), reportlab.lib (colors) | Libraries for creating PDF reports, modifying pages sizes, creating tables, and customizing them with colors |
| Utility and Miscellaneous | Random, math, datetime | Libraries for acquiring random numbers, performing mathematical calculations, and handling date-time operations |

# 4 Software Architecture

## 4.1 Modular Breakdown

The software, named ‘R.U.S.L.A.N. PRO’ (Reporting Utility for Solar Logging and Analysis of Numerical data PRO), for analysing PV data was built with a modular design. Four key modules form the architecture, each addressing a distinct part of the workflow. These modules collectively facilitate the processing of 2-and 8-pixel data. The modular design boosts technical credibility, enabling independent development, testing, and refinement of each component.

The entry point for the solar cell measurement analysis software is the ‘main_algorithm.py’. It enables a straightforward initialization process. This script initializes a Tkinter root window to host the GUI. Subsequently, the module instantiates the ‘SolarAnalysisApp’ class, passing the root window as an argument to establish the application framework. Followingly, the Tkinter event loop is created with root.mainloop(), keeping the GUI responsive to user interactions. This module is purposefully designed to be minimal and focuses on starting the application.

The ‘solar_analysis_app.py’ stores the ‘SolarAnalysisApp’ class, which is a core element for managing the GUI of the "R.U.S.L.A.N. PRO". Multiple crucial functions are handled within this comprehensive class. The core responsibilities of this class are listed below.

- To provide a file selection interface for 2- and 8-pixel analyses.
- To collect experiment metadata, including:
    - The name of the experimenter
    - Measurement date (DD/MM/YYYY)
    - The value of scan rate (V/s)
    - The value of Sun intensity ($W/m^2$)
    - Temperature (°C)
- To confirm the structure of selected Excel files for 2-pixel data
- To coordinate PDF report generation for both devices
- To manage application state through dynamic UI section visibility

- To implement a user feedback system via dialog boxes for a robust user experience

The main application window is created once the class is instantiated (Figure 20). The following elements are included in the main application window:

1. Branding elements:
    - Application logo
    - Welcome message
2. Function buttons for:
    - Selecting device type (2-pixel/8-pixel)
    - Accessing the software instructions
    - Accessing the SMAT research group website link
3. Experimenter name field
4. Footer with organizational details

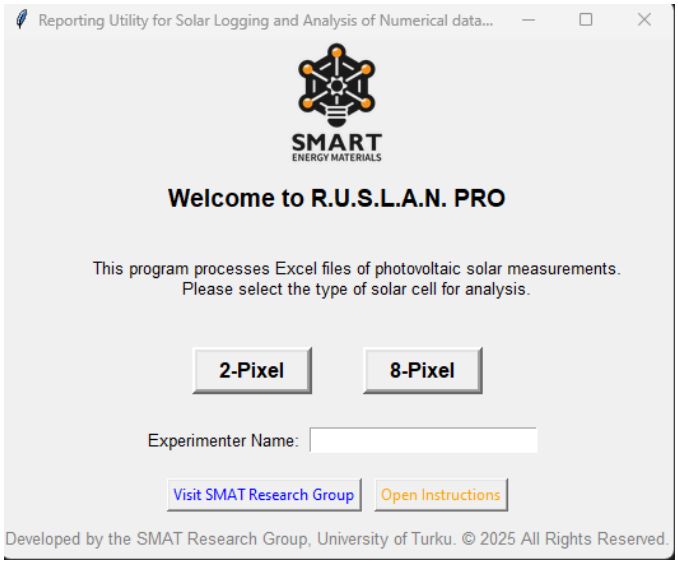


Figure 20. The default interface of the application upon launch

New interactive elements appear in the interface when a user presses a button to select a device type. For example, selecting the '2-Pixel' option reveals a metadata input section encompassing optional parameters that users may fill out according to their preferences. These parameters include measurement date, scan rate, Sun intensity, and temperature. To choose a file to analyze

2-pixel PSC data, the ‘Choose File’ button should be pressed. The system only accepts files with the .xlsx or .xlsm formats. A red 'No file selected' warning remains visible in the application window in the case of no selection. After choosing a file, the user is advised to check the file’s structure to confirm that it is suitable for the analysis. This verification process examines several important aspects: correct sheet names and order, presence of crucial columns ('VOLTAGE (V)', 'CURRENT (µA)', and 'POWER (µW)'), and proper cell formulas. The system provides immediate feedback, displaying either a success message for valid files or detailed error explanations for problematic ones. Following this, users can press the ‘Generate Report’ button to generate a PDF report for 2-pixel devices (Figure 21 displays the updated application window after the selection of the ‘2-Pixel’ button).

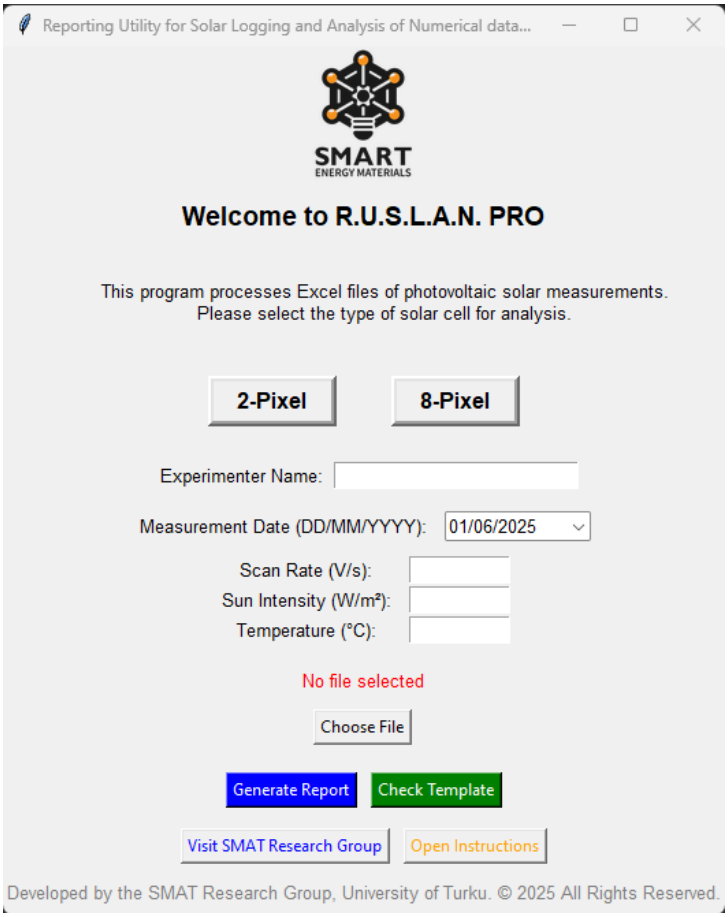


Figure 21. Application interface after selecting the ‘2-Pixel’ mode

Upon the selection of the ‘8-Pixel’ option, a single interactive element, which is the ‘Choose Folder’ button, emerges in the interface (illustrated in Figure 22). Contrary to the 2-pixel analysis, which requires Excel files, this mode expects selection of a root directory storing all 8-pixel data folders. Red ‘No folder selected’ text appears in the interface till users make a selection. The system executes automatic validation once a folder is selected. The appropriate

messages are displayed in the terminal to guide the users. The identified sample names and corresponding pixel counts are shown in the terminal for correct selections. An error message is shown in the terminal for invalid selections, providing details about the problem. After a successful folder choice, users can press the 'Generate Report' button to create comprehensive PDF reports for 8-pixel device data. The functions that constitute the 'SolarAnalysisApp' class are described for reference (Table 3).

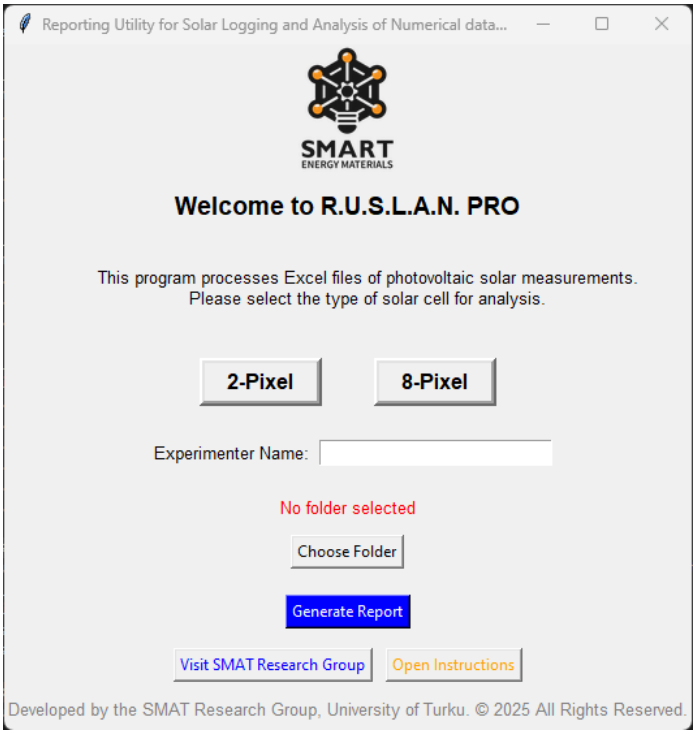


Figure 22. Application interface after selecting the '8-Pixel' mode

Table 3. Functional breakdown of the 'SolarAnalysisApp' class

| Component | Purpose | Dependencies |
|---|---|---|
| __init_() | To set up the main application window and GUI | tkinter |
| _setup_logo() | To set up the application logo | PIL.Image, pathlib |
| _setup_welcome_section() | To show the welcome message | tkinter.Label |
| _setup_selection_buttons() | To create 2-pixel/8-pixel mode buttons | tkinter.Frame, tkinter.Label, tkinter.Button |
| _setup_experimenter_info() | To add a text entry field for the experimenter's name | tkinter.Frame, tkinter.Label, tkinter.Entry |
| _setup_date_section() | To create a GUI section to enable the user to enter the measurement date via a date picker | tkinter.Frame, tkinter.Label, tkcalendar.DateEntry |

| Component | Purpose | Dependencies |
|---|---|---|
| _setup_metadata_section() | To create a GUI section to enable the user to enter the key experimental metadata: scan rate, Sun intensity, and temperature | tkinter.Frame, tkinter.Label, tkinter.Entry |
| _setup_file_section_2_pixel() | To create a GUI section to enable the user to select a measurement file for 2-pixel solar cell data analysis | tkinter.Frame, tkinter.Label, tkinter.Button, tkinter.StringVar, self.choose_file() |
| choose_file() | To open a file dialog for the user to choose an Excel file containing 2-pixel solar cell data. It accepts only .xlsx and .xlsm files, and updates the GUI with the selected file name | tkinter.filedialog.askopenfilename, tkinter.StringVar() |
| _setup_folder_section_8_pixel() | To build a GUI section for choosing a folder that contains I-V data files for 8-pixel PSC measurements | tkinter.Frame, tkinter.Label, tkinter.Button, tkinter.StringVar, self.choose_8_pixel_folder() |
| choose_8_pixel_folder() | To enable the user to select a directory containing 8-pixel measurement data. It updates the GUI with the selected folder path. | tkinter.filedialog.askdirectory, self.extract_sample_names(), self.collect_jv_file_paths() |
| extract_sample_names() | To identify and extract unique sample names and their pixel counts from subfolders within the selected 8-pixel measurement folder | os, re, collections.defaultdict |
| collect_jv_file_paths() | To scan through 8-pixel sample directories to find all CSV files named exactly 'Perform parallel JV.csv' for each pixel and map them for later data processing | os, re, messagebox |
| _setup_action_buttons() | To create three action buttons in the GUI. Two buttons are there to generate PDF reports for both device types. The third button is created to check the Excel structure for 2-pixel data. | tkinter.Frame, tkinter.Button, |
| check_template() | To validate the structure and content of the chosen Excel file against a template to ensure sheet naming, sheet order, column names, and formula integrity | pandas, openpyxl, re, messagebox |
| generate_report_2_pixel() | To start the process of creating a PDF report for 2- | random, messagebox, TwoPixelReportGenerator class |

| Component | Purpose | Dependencies |
|---|---|---|
| | pixel PSC devices with user-provided metadata | |
| generate_report_8_pixel() | To start the process of creating a PDF report for 8-pixel PSC devices. | random, messagebox, EightPixelReportGenerator class |
| _setup_footer() | Create a footer section in the GUI that includes copyright text, a button to access the SMAT Research Group's website, and a button to access software instructions | tkinter.Label, tkinter.Frame, tkinter.Button |
| hide_all_sections() | To clear the GUI view by removing all dynamic components, ensuring a clean navigation | - |
| show_2_pixel_section() | To display the GUI elements relevant to 2-pixel PSC processing | - |
| show_8_pixel_section() | To display the GUI elements relevant to 8-pixel PSC processing | - |

The module that is responsible for creating PDF reports from solar cell measurements is 'pdf_modifications.py'. This module consists of 2 main classes, 'TwoPixelReportGenerator' and 'EightPixelReportGenerator'. As the name suggests, the first one manages the report creation for 2-pixel data, while the second one is initiated if the user wants to create reports for 8-pixel PSC data. The main aim of these classes is to transform raw PSC data into structured and visually appealing reports that include graphs, tables, and metadata.

The 'TwoPixelReportGenerator' class is designed to generate structured PDF reports from Excel-based 2-pixel PSC measurement data. The class solely focuses on visual presentation instead of performing calculations. External analysers are employed to process the raw data before rendering. The file path to the Excel data, the experimenter's name, and an optional metadata dictionary of measurement conditions are three important inputs that this class takes upon initialization. A cover page generation is the first step in the report creation process, and it includes a title ('Solar Cell Measurement Results'), institutional logos, the experimenter's name, the experimentation and report generation date, and metadata (if provided). Subsequently, a list of sheets is extracted from the Excel file by the class. Each pair of sheets corresponds to forward and reverse scans of the identical pixel. The class iterates through these sheet pairs to verify the presence of valid data. If valid data is found in either scan direction, the class generates a dedicated page for the corresponding pixel. The generated sheet involves

a J-V curve for forward, reverse, or both scans based on data availability. The lines in the generated J-V curves are color-coded by scan direction, helping the researchers to easily identify the scan directions. Below the graph, a PV performance table is displayed. The table includes key PV parameters, including active area, $J_{sc}$, $V_{oc,}$ FF, PCE, $J_{mp}$, $V_{mp}$, $R_{s,}$ and $R_{sh}$. If there is valid data in both scan directions, HI is displayed below the performance table. When the generator encounters a sheet pair with no usable data, it stops data processing of the remaining sheets, ensuring that only valid data is included in the report. The report ends with a summary page that aggregates all analysed pixels, displaying box plots. The generated box plots compare the distribution of key parameters (PCE, FF, $J_{sc,}$ and $V_{oc}$) across all pixels, allowing for quick performance evaluation. The dots in the generated box plots are color-coded by the scan direction, allowing researchers to easily distinguish between forward and reverse scans. The class also performs dynamic page numbering to ensure easy navigation in the PDF reports. Once the report generation process completes, the generated PDF automatically opens. The functions included in the 'TwoPixelReportGenerator' are presented and explained for reference (Table 4).

Table 4. Functional breakdown of the 'TwoPixelReportGenerator' class

| Component | Purpose | Dependencies |
|---|---|---|
| __init_() | To initialize the report generator with the file path, input data, and PDF canvas | datetime, os, reportlab.pdfgen.canvas, repotlab.lib.pagesizes.A4 |
| _add_page_number() | To add dynamic page numbers to the bottom-right of each page | reportlab.lib.colors, reportlab.pdfgen.canvas |
| _add_icons() | To place institutional logos (UTU/SMAT logos) on pages with adjustable opacity and scale | PIL.Image, reportlab.lib.utils, os |
| _add_cover_page() | To create a cover page with title, experimenter name, report date, and logos | datetime, reportlab.pdfgen.canvas |
| _add_sheet_results() | To generate a result page based on Excel sheets of the same pixel of a 2-pixel device (forward /reverse scans) | TwoPixelDataAnalyzer, pandas, reportlab.platypus.Table |
| _add_final_page() | To create a final summary page with comparative box plots | TwoPixelMeasurementAnalyzer, reportlab.lib.colors |
| save_pdf() | To coordinate the full report generation workflow | pandas.ExcelFile, os, platform, subprocess |

The ’EightPixelReportGenerator’ class is designed to generate PDF reports for 8-pixel PSC data acquired via Fluxim Litos Lite equipment. Contrary to the ‘TwoPixelReportGenerator’ class, users are not required to manually enter data for experiment conditions, as the performance files include all the necessary measurement details, ranging from light intensity to temperature. The report generation begins with a cover page, which includes elements such as institutional logos, a title ("Photovoltaic Performance Report: 8-Pixel Device Analysis"), the experimenter’s name, and the report generation date, providing a professional introduction to the report. The input file paths are processed and organized by sample and pixel number by the class. Each pixel’s data is composed of a pair of files. The pair includes an I-V measurement data file and a performance data file of the same pixel. Details about the current-voltage measurement are contained in the I-V data file, while the performance data file stores PV parameters. A specific page is created for each valid file pair in the PDF report by the generator. The created dedicated pages include a J-V curve plot. Based on the I-V data, the plot is titled differently to distinguish between light and dark measurements. Below the J-V plot, a performance data table is included, showing the values for $J_{sc}$, $V_{oc}$, FF, PCE, $J_{mp}$, $V_{mp}$, $R_s$, and $R_{sh}$. The page also includes a value for HI if both scans include valid data. Each page also includes metadata acquired from the provided files, including start time, active area, voltage range, sweep speed, scan direction, and temperature. A summary page with box plots is added by the generator when all pixels of the same sample are analysed. The box plots enable users to compare the distribution of PCE, FF, $J_{sc}$, and $V_{oc}$ across all pixels in a given sample. The process repeats for the next sample, beginning with sheets showing J-V curves and performance data table, and ending with a summary page with box plots. The class also performs dynamic page numbering to ensure easy navigation. The created PDF report is automatically launched once the report generation is complete. Similar to the ‘TwoPixelReportGenerator’, this class concentrates on report rendering and leaves data processing to external analyzers. The functions included in each class are similar in name and purpose, except for the final function to generate a summary page with box plots. The reports for 2-pixel devices always include one final summary page, while the summary page count in reports for 8-pixel devices depends on the number of samples. The functions included in the ‘EightPixelReportGenerator’ are described for reference (Table 5).

Table 5. Functional breakdown of the ‘EightPixelReportGenerator’ class

| Component | Purpose | Dependencies |
|---|---|---|
| __init_() | To initialize the report generator with file paths, input data, and PDF canvas | datetime, os, reportlab.pdfgen.canvas, repotlab.lib.pagesizes.A4 |
| _add_page_number() | To add the current page number at the bottom of the page | reportlab.lib.colors, reportlab.pdfgen.canvas |
| _add_icons() | To place institutional logos (UTU/SMAT logos) on pages with adjustable opacity and scale | PIL.Image, reportlab.lib.utils, os |
| _add_cover_page() | To create a cover page with title, experimenter name, report date, and logos | datetime, reportlab.pdfgen.canvas |
| _add_sheet_results() | To generate a result page for an 8-pixel device based on a pair of Excel files | EightPixelDataAnalyzer, reportlab.platypus.Table, reportlab.lib.colors |
| _add_final_page() | To create a summary page with comparative box plots | TwoPixelMeasurementAnalyzer.plot_boxplot, reportlab.lib.colors |
| save_pdf() | To manage the full report generation process | reportlab.pdfgen.canvas, os, platform, subprocess |

The final integral component of the developed software tool is the ‘file_processing.py’ module. It was created to process and analyse PV measurement data from PSCs. The four main classes – ‘TwoPixelDataAnalyzer’, ‘TwoPixelMeasurementAnalyzer’, ‘EightPixelDataAnalyzer’, and ‘EightPixelSampleAnalyzer’ – form this module. While the ‘TwoPixelDataAnalyzer’ and ‘TwoPixelMeasurementAnalyzer’ focus on extracting parameters from 2-pixel PSCs, 8-pixel PSC data is processed via ‘EightPixelDataAnalyzer’ and ‘EightPixelSampleAnalyzer’.

The ‘TwoPixelDataAnalyze’ is initialized with three inputs. The inputs are the file path of the Excel file, the selected sheet name, and optionally the next sheet name, which is the paired scan direction. Depending on the availability of dual-scan data, the class processes data from one or both sheets. After receiving the inputs, the class validates the presence of valid data in the specified sheets. This step involves checking for essential columns that contain voltage and current density values and confirming that these columns store non-null values. This check prevents errors during analysis. The major responsibilities of this class are to generate a J-V graph, construct a table of performance parameters, and calculate HI if both scan directions have valid data. The ‘matplotlib’ library is employed to create a J-V graph. The generated graph possesses legends and color-coded lines, enabling users to differentiate between different scan directions. The parameters related to MPP are indicated with marks on the graph. The data to generate a J-V graph is extracted from the inputted Excel file, which includes formulas to

calculate current and power density before the software analysis. Based on the given Excel file, the class processes the data, generates a graph, which is subsequently saved in high-resolution format with a timestamp in the file name. The generated graph's file path is then passed to the 'TwoPixelReportGenerator' class for inclusion in a result sheet. The generated table displays the values of active area, PCE, FF, $J_{sc}$, $V_{oc}$, $V_{mp}$, $J_{mp}$, $R_s$ and $R_{sh}$. The active area is directly acquired from a user-inputted cell in the Excel file. Linear regression is employed to estimate the values for $J_{sc}$ and $V_{oc}$, if the Excel file does not include these values. Based on the acquired values, FF and PCE are calculated with equations 4 and 5, respectively. The slope of the J-V curve near $J_{sc}$ is analysed for the calculation of the $R_{sh}$. A linear regression is applied around the data points where the voltage is zero to identify the slope. Subsequently, the reciprocal of this slope is determined, as it is equal to $R_{sh}$. The slope near $V_{oc}$ is analysed to derive $R_s$. Linear regression is applied to data points with small current densities to estimate the slope. $R_s$ corresponds to the absolute value of the resulting slope. These resistance parameters are key to understanding the solar cell's efficiency losses. This class also calculates the HI with equation 7 when both forward and reverse scan data are provided. This metric is essential in quantifying the difference in performance between scan directions. The functions in 'TwoPixelDataAnalyzer' are detailed and explained for reference (Table 6).

Table 6. Functional breakdown of the 'TwoPixelDataAnalyzer' class

| Component | Purpose | Dependencies |
|---|---|---|
| __init_() | To initialize analyzer with Excel data. To load and validate primary and paired sheets | _load_data(), _validate_data() |
| _load_data() | To load Excel sheet data into a DataFrame | pandas.read_excel |
| _validate_data() | To check if DataFrame contains valid J-V data | pandas |
| generate_jv_graph() | To plot combined J-V and P-V curves with MPP markers for valid datasets. To save the plot as a PNG file | matplotlib.pyplot, datetime, os |
| calculate_hi() | To calculate the HI value based on PCE values from forward and reverse scans | - |
| extract_performance_data() | To extract PV parameters from a DataFrame | Pandas, numpy, scipy.stats.linregress |
| construct_table() | To build a parameter table for valid datasets | extract_performance_data() |

The 'TwoPixelMeasurementAnalyzer' class is another key component, designed to streamline the analysis of PV parameters from a 2-pixel Excel file. The primary aim of this class is to

organize $J_{sc}$, $V_{oc}$, FF, and PCE in a structure that their distribution can be visualized in box plots. The generated box plots incorporate color-coded dots to enable users to distinguish between scan directions. The class processes all sheets within a provided Excel file. Its sole input is the file path of the Excel file. Once it is received, the analysis begins by reading the Excel file and identifying all sheets. Subsequently, the key PV parameters are extracted from each sheet. Loading the data with the 'pandas' library is the first step in the parameter extraction process. Next, the class validates the presence of valid data in each sheet, confirming the valid and non-null data. If $J_{sc}$ and $V_{oc}$ values are present in the dataset, they are directly extracted. Otherwise, a linear extrapolation is applied. After identifying the MPP, the FF and PCE values are extracted. The class determines the scan type of the measurement from the sheet name. 'MeasurementResults' dataclass is used to store the extracted parameters into distinct lists based on the scan type. Three types of lists exist for each parameter: a list to store parameters from forward scans, a list to store parameters from reverse scans, and a combined list to store parameters from both directions. This structure allows for the easy manipulation of data and is ideal for generating box plots that highlight differences between scan types. The box plots are created with the static method, 'plot_boxplot', which leverages the seaborn library. After creating the plots, the class saves them as high-resolution images. The method returns the file paths of the generated box plots, which enable their inclusion in PDF reports. The functions and methods that form the 'TwoPixelMeasurementAnalyzer' are described for reference (Table 7).

Table 7. Functional breakdown of the 'TwoPixelMeasurementAnalyzer'

| Component | Purpose | Dependencies |
|---|---|---|
| __init_() | To initialize the analyzer, load the Excel file, and process all sheets to extract PV metrics | pandas.ExcelFile |
| _analyze_sheets() | To iterate over sheets, extract PV parameters, and store results in 'Measurement Results' objects | - |
| _has_required_columns() | To validate if the DataFrame contains the required columns with non-null data | pandas |
| _extract_jsc() | To calculate short-circuit current density at zero voltage via direct lookup or linear extrapolation | - |
| _extract_voc() | To calculate open-circuit voltage at zero current density via direct lookup or linear extrapolation | - |

| Component | Purpose | Dependencies |
|---|---|---|
| _extrapolate_zero_x() | To use linear regression to find the y=0 intercept when no exact x=0 point exists | Scipy.stats.linregress, numpy.argsort |
| _calculate_derived_parameters() | To compute FF and PCE from MPP and store them in scan direction-specific lists | extract_performance_data() |
| plot_boxplot() | To generate a boxplot with color-coded data points and save it as a PNG | seaborn.boxplot, seaborn.stripplot, matplotlib.pyplot, numpy, datetime |

The 'EightPixelDataAnalyzer' class is built to analyse PV measurement data from 8-pixel PSC devices. It has three main objectives: (1) to extract parameters from the input data, (2) to generate J-V graphs to visualize the behaviour of devices, and (3) to construct a table with key PV metrics. The class requires 4 different inputs: (1) a file path to raw I-V data, (2) a file path to performance data, (3) a string identifier of the sample being analysed, and (4) an integer specifying which pixel of the device is under examination. The class performs several essential steps during initialization. The first is file reading, in which data files are loaded and parsed into manageable structures. The next step involves the extraction of metadata, such as light intensity, sample area, and scan direction. The value of light intensity acquired from files enables the software to decide whether the measurement is a light or dark I-V study. Subsequently, the raw I-V data is validated, and current values are converted to current densities. The data is split into forward and reverse segments based on NaN markers for bidirectional scans. The final step includes the parameter extraction. Most P-V parameters are directly extracted from the performance file without processing. This significantly reduces the computational burden. $R_s$ and $R_{sh}$ are the only parameters that are not included in the performance file. They are calculated using linear regression on specific regions of the J-V curve, with a similar approach in the 'TwoPixelMeasurementAnalyzer' class. The curves in the generated graphs are color-coded to distinguish between the scan direction. The plots include markers to display MPP-related parameters in the curve. The generated tables present the parameters in separate columns for forward and reverse directions for bidirectional scans, enabling a side-by-side comparison. The functions used in the 'EightPixelDataAnalyzer' class are described for reference (Table 8).

Table 8. Functional breakdown of 'EightPixelDataAnalyzer'

| Component | Purpose | Dependencies |
|---|---|---|
| __init_() | To initialize analyzer for a pixel. To parse I-V and performance files, validate data, and compute PV metrics | _parse_file(), _validate_data(), _modify_data(), get_performance_data() |
| _clean_line() | To remove unwanted characters from raw file lines | re |
| _parse_file() | To read I-V data files | open(), _extract_metadata(), _extract_data() |
| _extract_metadata() | To parse metadata from header lines | re |
| _extract_data() | To identify the data block start, split bidirectional scans into separate DataFrames | pandas.read_csv(), io.StringIO |
| get_metadata() | To return the extracted metadata dictionary | - |
| get_dataframe() | To return parsed I-V DataFrames | - |
| get_performance_data() | To extract PV parameters from the performance CSV. To compute $R_{sh}$ and $R_s$ | pandas.read_csv(), scipy.stats.linregress |
| generate_jv_graph() | To plot J-V and P-V curves with markers for forward/reverse scans and save it as PNG | Matplotlib, random |
| construct_table() | To build a parameter table for valid scans | Get_performance_data() |
| calculate_hi() | To return HI in the case of a bidirectional scan | - |
| _validate_data() | To validate the DataFrames | - |
| _modify_data() | To convert raw current to current density | - |

The 'EightPixelSampleAnalyzer' is designed to aggregate and analyse performance metrics across all pixels of an 8-pixel PSC device. Its primary aim is to process performance files, classify them based on light intensity, acquire key PV performance metrics, and store them in a format that enables the generation of the box plot. The class requires a single input – a list of file paths pointing to the performance CSV files. The class undertakes several critical steps during initialization. The classification of performance files is the first step, where the provided CSV files are classified into light and dark measurement sets depending on the light intensity metadata obtained from each file, followed by the parameter extraction. The box plot generation is only required in light measurements, as they are more significant compared to dark measurements. Therefore, the parameter extraction is performed only for light studies in this class and stored in the 'MeasurementResults' containers. The functions in the 'EightPixelSampleAnalyzer' class are described for reference (Table 9).

Table 9. Functional Breakdown of 'EighPixelSampleAnalyzer' class

| Component | Purpose | Dependencies |
|---|---|---|
| __init_() | To initialize the analyzer with CSV paths. To classify files and start PV metric extraction | _self.classify_performance_files_by_light_intensity(), analyze_sample() |
| classify_performance_files_by_light_intensity() | To split CSV files into light_files and dark_files using metadata | pandas.read_csv(), re |
| _analyze_sample() | To process light I-V measurement files | pandas.read_csv(), re, extract_parameters(), store_values() |
| extract_parameters() | To split a comma-separated metadata line into a cleaned parameter list | - |
| store_values() | To map parsed parameters into 'MeasurementResults' container by scan type | re |

## 4.2 Software Processing Pipeline

This section presents the software processing pipeline, showing the sequential flow of data and operations within the developed application. The pipeline connects the classes in the modules into an automated software built to process I-V data from the 2- and 8-pixel PSC devices. The pipeline starts with the initialization of Tkinter-based GUI defined in the 'main_application.py' module, which serves as the entry point. In the module, 'SolarAnalysisApp' class is instantiated within the main Tkinter window. Two buttons with corresponding text are included in the main window to enable the user to select the type of device that has been measured.

1. Input File Selection

    - **2-pixel devices**: The user chooses a correctly formatted Excel file containing the I-V data of the measurement. The Excel file includes multiple measurements, each corresponding to a measurement scan (forward or reverse). For the generation of the report, the user is required to enter the experimenter's name. The metadata section, including scan rate, Sun intensity, temperature, and experiment date, allows the user to input the measurement conditions of the experiment. The user can press the 'Generate Report' button to generate reports, initializing the 'TwoPixelReportGenerator' class. This class starts by creating a cover page with organizational icons and title text before proceeding to I-V data processing.

- **8-pixel devices**: The user chooses the directory that contains the folders of the 8-pixel device measurements from Fluxim Litos Lite equipment. As the files include information about the measurement conditions, the user is only required to enter the experimenter's name as metadata. The user can press the 'Generate Report' button to generate reports, initializing the 'EightPixelReportGenerator' class. This class starts by creating a cover page with organizational icons and title text before proceeding to I-V data processing.

2. Data Loading and Validation

- **2-pixel devices: '**TwoPixelReportGenerator' loads the Excel files and retrieves all the sheet names. Each sheet represents the I-V scan of a pixel in a specific direction (forward or reverse). The sheets are organized in pairs, with each pair corresponding to a single pixel (either left or right) of a sample, scanned in both directions. The code iterates over the prepared pairs and initializes 'TwoPixelDataAnalyzer' for each pair. 'TwoPixelDataAnalyzer' validates the - presence of required columns and ensures non-null data in the given pair.

- **8-pixel devices:** Once the file paths are provided, 'EightPixelReportGenerator' loops through each sample, processing its pixels. For each pixel, the function iterates through a list of files, where the files are arranged in pairs: one for I-V curve data, and one for the performance data. Each pair represents a single measurement. Then, 'EighPixelDataAnalyer' class is initiated for the measurement of each pixel. Subsequently, this class checks the presence of valid data in the provided files and handles inconsistent formatting of the data.

3. Parameter Extraction and Plot Generation

- **2-pixel devices:** The 'TwoPixelDataAnalyzer' extracts parameters from each sheet. It uses a linear regression for $J_{sc}$ and $V_{oc}$ if exact zero points are missing. It performs the calculation of HI when both scans are available. The class is capable of generating I-V and P-V graphs using the 'matplotlib' library, with distinct colours for scan directions, including markers to indicate MPP-related parameters. The generated graphs are saved as high-resolution images, which will be used by 'TwoPixelReportGenerator' to be placed in the report. This class also generates tables, summarizing critical parameters, organized by scan

direction for easy comparison. After analysing every valid sheet in the Excel file, ‘TwoPixelReportGenerator’ generates a summary page and initializes ‘TwoPixelMeasurementAnalyzer’, which structures the extracted parameters for boxplot visualization. The data points are color-coded based on the scan direction**.**

- **8-pixel devices:** The ‘EightPixelDataAnalyzer’ extracts pre-calculated parameters from performance files. It uses linear regression to compute $R_s$ and $R_{sh}$. It also generates I-V and P-V plots via the ‘matplotlib’ library, saving them as a PNG file to be later used in report rendering. After analysing all valid pixels in a sample, the class aggregates parameters across all pixels, classifying files as light or dark based on metadata and storing results in the ‘MeasurementResults’ container. The stored results are then displayed in the boxplot generation to compare the parameters within a sample.

4. Report Generation

    - The PDFs are generated via the ‘ReportLab’ library in both classes responsible for report creation. The report generation happens as the analysis of the pixels progresses further. Cover, result, and summary pages are the constituting elements of the report for both types of devices. The cover page includes a title, the experimenter’s name, metadata, and institutional icons. For the 8-pixel reports, the metadata is included in the result sheets, directly extracted from the provided files. The content of the result sheets is almost identical for both configurations, including a J-V plot and performance table. The only difference is that the metadata is displayed on the cover page for the reports generated for 2-pixel devices. The summary page includes a 2x2 grid of box plots visualising aggregated parameters. The report generated for 2-pixel solar cells includes a single summary page that compares the PV parameters across all valid sheets in the Excel file. In contrast, the report for 8-pixel devices may include multiple summary pages, each providing a comparative overview of PV parameters for a specific sample.

The operation logic was carefully designed for this software (illustrated in Figure 23).

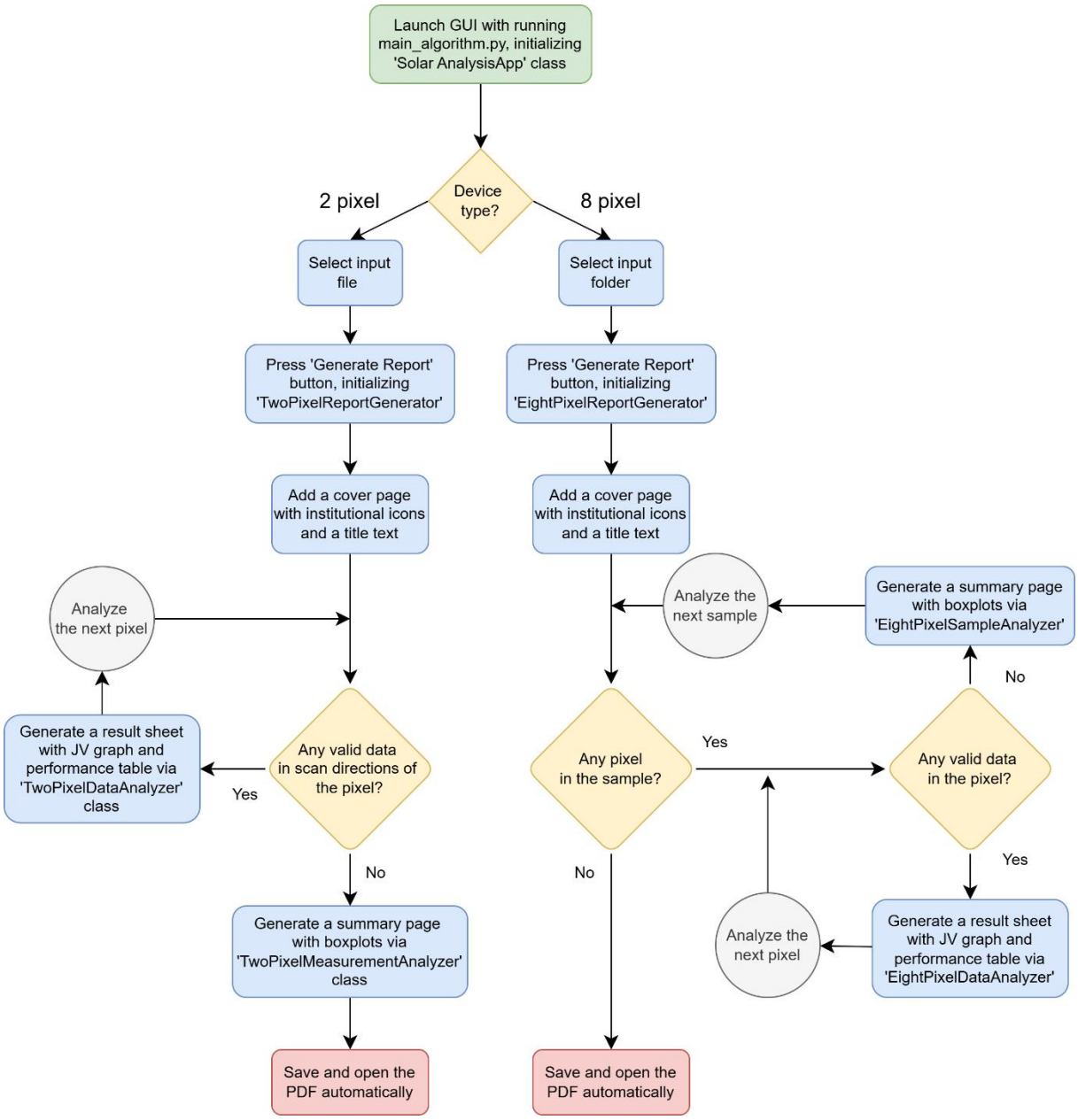


Figure 23. The flowchart of the report generation process within the developed software tool

# 5 Results and Discussion

The main objective of the thesis was to develop a software tool to streamline the analysis of optoelectronic measurement data of PSCs with 2-and 8-pixel device structures. The presented software addresses the time-consuming challenge of processing multiple measurements. The software greatly reduces the burden on researchers by automating calculations and report generation. It allows for the analysis and visualization of key performance parameters of PSCs. The text size and font are carefully selected to ensure high readability of the report.

The generated report consists of 3 types of pages. First is the cover page, which includes the report title, the experimenter's name, and organizational logos (Figure 24). The metadata is also illustrated on the cover page of reports generated for 2-pixel devices, with the assumption that the measurement conditions are the same for the provided measurements. In the case of 8-pixel solar cells, the metadata is displayed on the result pages, being directly extracted from files rather than being manually entered by the user. The next sheet of the report is the result page. The structure of the results pages for devices with both configurations is almost identical. The sole difference is that the result pages for 8-pixel devices include metadata for each measurement. The title of the result page gives information about the pixel under analysis. For 8-pixel devices, it identifies the sample name and the specific pixel number, while for 2-pixel devices, it indicates whether the right or left pixel is analysed. The page also includes institutional logos with faded opacity. Each result page encompasses a graph and a table. Both I-V and P-V curves are displayed in the graph. A solid line is selected to represent the I-V curve, while a dashed line is used to show the P-V curve to facilitate differentiation. Furthermore, different scan directions are indicated with color-coded lines. MPP-related parameters, such as $J_{mp}$ and $V_{mp}$ are highlighted by the markers on the graph. The accompanying table below the graph lists important parameters, including active area, $J_{sc}$, $V_{oc}$, FF, PCE, $J_{mp}$, $V_{mp}$, $R_{sh,}$ and $R_s$. The parameters are placed in rows organized by scan direction for clarity. Both the graphs and tables have clear captions, meeting the clarity and documentation standards expected in research environments. The software tool calculates and includes HI in the result page when data for both scan directions is available. The result pages also include page numbering (Figure 25).

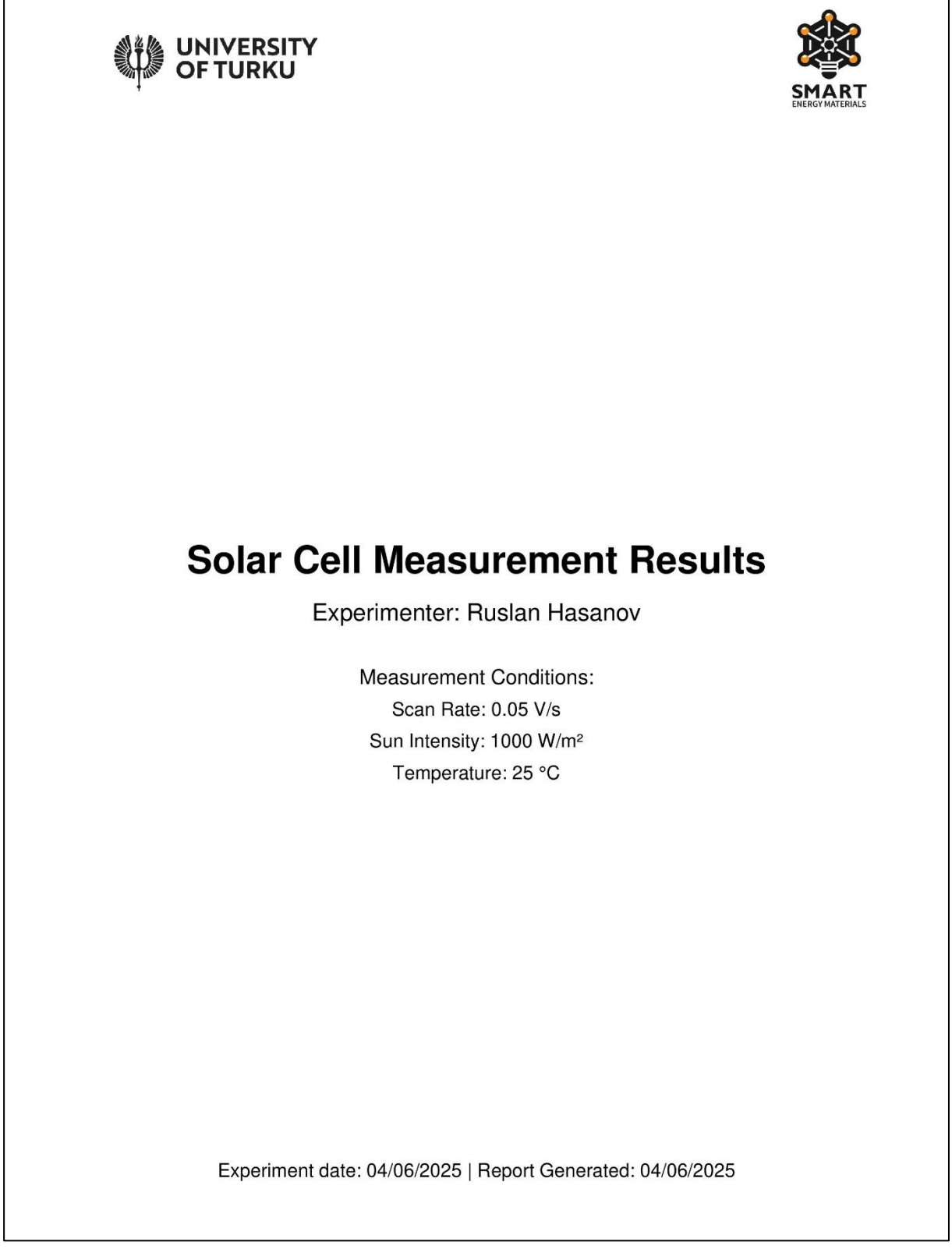


Figure 24. A cover page of the report generated for 2-pixel PSCs

## Results of Sample 1: Right Pixel

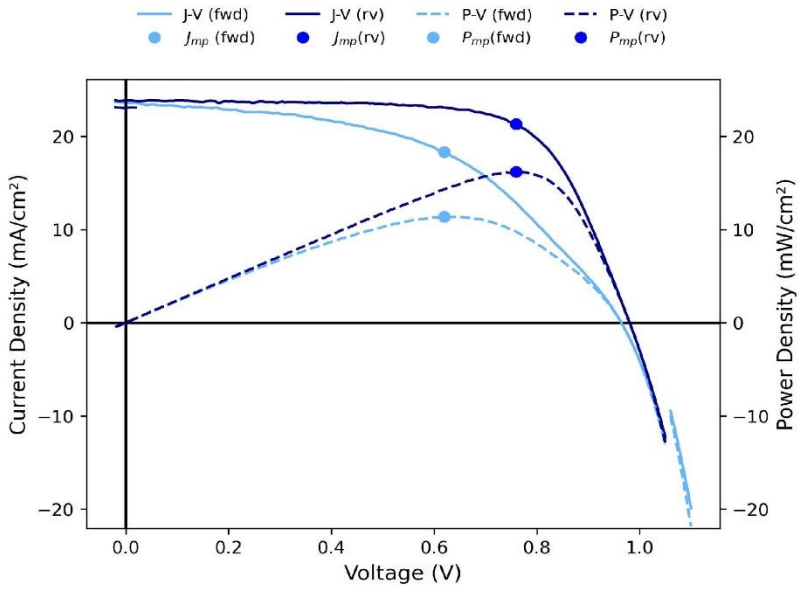


Figure 2. J-V Curve of Sample 2: Right Pixel

Table 2. Performance Data of Sample 2: Right Pixel

| Parameter | Active Area | Jsc | Voc | Fill Factor | PCE | Jmp | Vmp | Rsh | Rs |
|---|---|---|---|---|---|---|---|---|---|
| Units | cm² | mA/cm² | V | - | % | mA/cm² | V | Ω·cm² | Ω·cm² |
| Forward Scan | 0.1008 | 23.641 | 0.965 | 0.498 | 11.361 | 18.323 | 0.62 | 512.542 | 10.552 |
| Reverse Scan | 0.1008 | 23.829 | 0.981 | 0.692 | 16.188 | 21.3 | 0.76 | 6048.0 | 6.794 |

The calculated Hysteresis Index (HI) for Right Pixel is 0.298



Figure 25. A result page of the report generated for 2-pixel PSCs

As previously mentioned, the report also includes a summary page, which displays a 2×2 grid of box plots visualising aggregated parameters. The structure of the summary page is identical for devices with both configurations. The box plots provide a visual representation of the distributions of key PV parameters – PCE, FF, $J_{sc}$, and $V_{oc}$. The plots depict the median, interquartile range, and outliers. This allows for the quick assessment of the central tendency and variability of parameters without the need to examine raw data tables. Outliers serve as indicators of anomalous measurements that may require further investigation. Users can observe the exact values within the dataset, with individual data points shown in box plots. Furthermore, the plots offer an easy performance comparison between scan directions with the color-coded data points. Overall, the provided box plots effectively condense large datasets into a single and interpretable graphic. This approach greatly streamlines the process, reducing the burden of manual data examination (Figure 26 illustrates an example of a summary page).

Significant benefits are offered in the 'R.U.S.L.A.N. PRO' software tool to support researchers analysing PV performance data from PSCs. The developed software is an open-source tool and is available for researchers. Researchers can access the software via the Github repository without any cost, making it accessible to a global audience (Hasanov, 2025). Users are allowed to view, modify, and redistribute the source code according to the GPL-3.0 license. Researchers can tailor the tool to their preference. For example, it could be modified to incorporate advanced statistical methods or support new data formats. This flexibility enables the tool to stay relevant as experimental procedures evolve. The software's user interface is built to be simple and intuitive. This characteristic allows users with no coding background to easily navigate file selection, input experiment metadata, and start data analysis. The tool includes a button that could be pressed to view the 'SMAT' research group at the University of Turku. There is also a dedicated button for users to view the software instructions. User experience is highly enhanced with these functionalities, which enable users to quickly adapt to the software's capabilities. The software also reduces a significant amount of manual workload in data processing and analysis. Researchers typically spend a considerable amount of time on manual parameter extraction, plotting, and report generation in the conventional analysis of I-V data. These lab-intensive tasks are eliminated by the software, which automates these processes, helping researchers to save time.

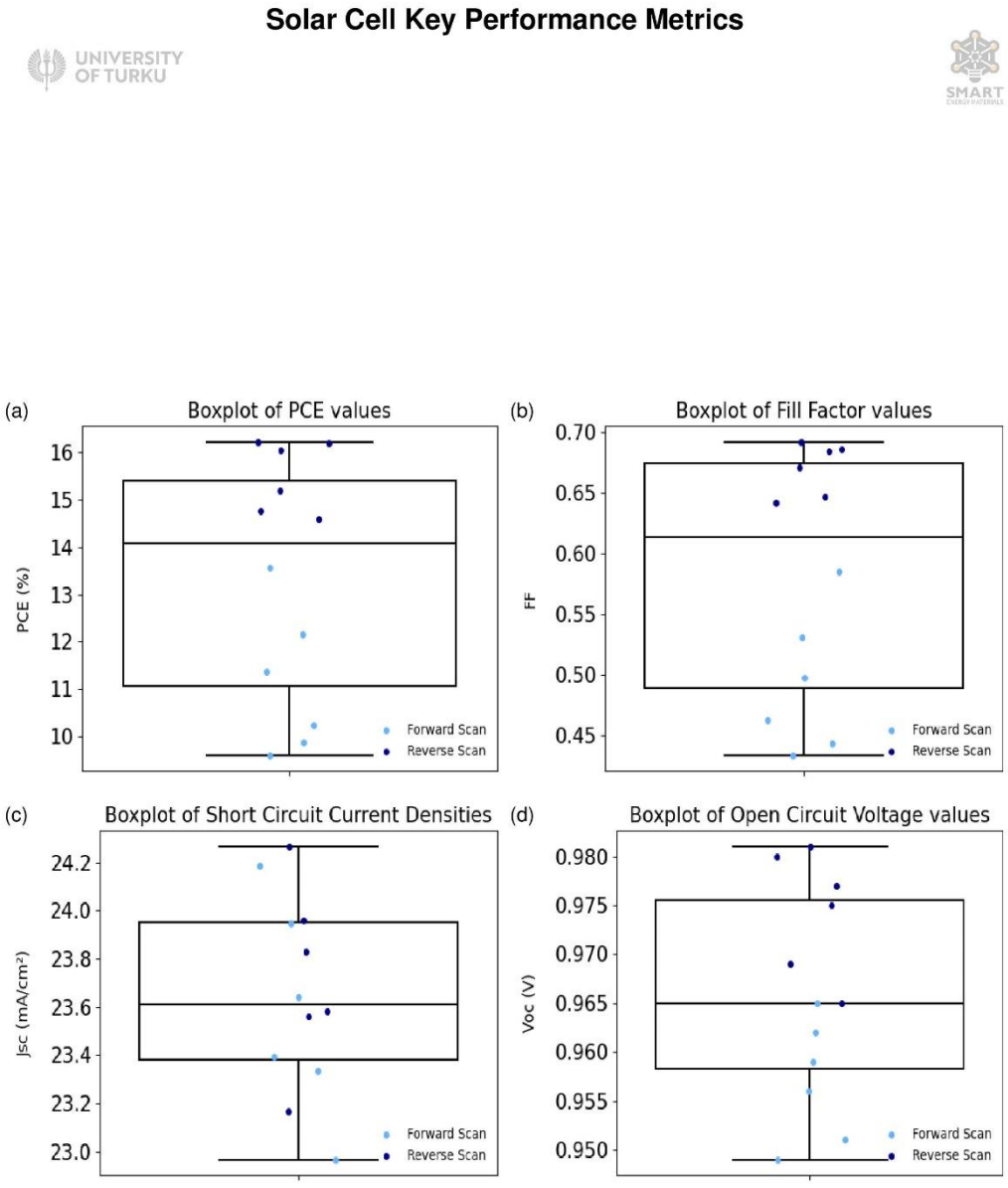


Figure 7. (a) PCE, (b) FF, (c) Jsc, (d) Voc of the samples

Figure 26. An example of a summary page in the generated report

This software tool is also subject to several limitations that users should be aware of. Its reliance on a strict structure for Excel files utilized in 2-pixel device analysis is one of the significant downsides of the software. A consistent sheet layout, involving predefined column names, is key to the operation of the software. The software will fail to extract key PV parameters and produce errors and incomplete reports when an Excel file without the predefined structure is fed into the program. This drawback necessitates users to double-check their Excel files' structures to ensure that they do not deviate from the explained structure. Although the structure of the Excel file can be validated by the 'Check Template' button in the software, the software is unable to address the structural issues in the Excel file, requiring the user to manually fix it. Renamed columns and misplacement of data are common problems. The strict naming convention for Excel sheets is another important limitation of the tool for 2-pixel PSC analysis. This convention dictates how the software interprets scan data. The sheet names follow a specific pattern (e.g., '3-l-rv' for third sample, left pixel, reverse scan). If users mistakenly place data, such as entering the data for the second sample's right pixel reverse scan in a sheet named '3-l-fw', the tool will incorrectly treat and interpret the data, leading to mislabelled results in plots and reports. It is required to place voltage and current data in their corresponding columns with attention to the units. Voltage values should be entered in volts, while the current should be inputted in microamperes. Users are required to enter the active area in square centimetres; the entry of data in swapped columns, or with different units, will lead to flawed reports with erroneous calculations. These details necessitate the researchers leveraging this software tool to be careful of data entry to avoid such issues.

There is also a strict limit on the volume of the 2-pixel data that could be analysed. The software is capable of handling a maximum of 300 rows of I-V data for 2-pixel devices. Although this is adequate for typical I-V measurements, which generally contain around 240 rows, the analysis of datasets exceeding this threshold will lead to incomplete analysis and missed data points. The software's applicability for high-resolution scans or experiments involving extended voltage ranges is hindered by this drawback embedded in the data processing logic of the software. The larger datasets than the set limit should be pre-processed to fit within this limit.

The developed software is specifically tailored to process the 8-pixel data acquired with the measurements done via Fluxim Litos Lite. As the tool is unable to parse alternative file structures and formats, the software can appear less useful to researchers employing different equipment. The software structures the given files in pairs, and it always approaches the first file in the pair as a raw I-V data file, while the second file in the pair is assumed to be the file

that contains performance parameters according to the default output of Fluxim Litos Lite. The data will not be successfully processed if this order is altered. Furthermore, the software identifies the 8-pixel measurement files based on the file name, as such files always have the ending of ‘Perform parallel JV.csv’. If the endings of the file names are altered, the software will not be able to locate measurement files. Moreover, the software’s dependency on specific patterns, such as ‘NaN’ markers for bidirectional scans, requires the default structure of CSV files to remain unchanged. The tool’s versatility is impacted by this equipment-specific need.

There are other disadvantages beyond the user-specified constraints that can be addressed in the future. Despite the software’s robust error-handling mechanism, users may not receive detailed feedback for some unexpected issues. As the software has been released recently, the scope of these unforeseen scenarios is considerably narrow. Therefore, the error messages may lack specificity. This necessitates researchers to manually inspect their data for issues such as modified file structures and incorrect units. This could be particularly difficult for non-technical users relying on the simplicity of the GUI. While the developed tool is highly effective within its designed scope, users are encouraged to remain mindful of data preparation requirements and adhere to its predefined equipment and structural limitations.

Several potential improvements could enhance the software’s usability and extend its capabilities. The ‘Check Template’ button currently validates the structure of Excel files for 2-pixel devices by checking the sheet names, columns, and formulas. A next step could be to enable the software to correct automatically common errors, such as misplaced sheets and misnamed columns, simplifying the data preparation. Another major enhancement would be to make the software more versatile by adding functionalities to support alternative equipment for 8-pixel device analysis. Currently, the software can only handle 8-pixel data acquired with Fluxim Litos Lite. Another useful feature would be adding interpretive insights to the reports. For example, the software could analyse the I-V data and offer helpful comments on the origin of unusual patterns, explaining the reasons behind anomalies. Including a performance score based on key PV metrics and ranking devices in the summary report would also help users to quickly identify the best solar cells. Extending the tools’ capabilities to process the operational stability data, such as from MPP tracking and T80 measurements, would be another enhancement for both I-V and stability studies. Finally, the software’s analytical power can be taken to the next level with the inclusion of algorithms to calculate the ideality factor and process Incident Photon-to-Current Efficiency (IPCE) measurements. These improvements could be made to meet the evolving needs of PSC researchers.

# 6 Conclusion

Analysis of PSC measurement data can be labour-intensive, error-prone, and tedious, often culminating in inconsistent research outcomes and inefficiencies, as device architectures evolve toward multi-pixel layouts. Addressing this challenge would bring a significant advancement for PSC research, as rapid experimentation and quality data documentation are crucial for fabricating stable and high-performance solar cells. This thesis addresses this issue by introducing a Python-based software tool with the ability to process PSC data from 2- and 8-pixel device configurations. The tool offers structured input handling, automatic extraction of key performance parameters, generation of plots, and detailed PDF reports. The developed platform aims to reduce manual effort and ensure consistent results across datasets by streamlining the analytical processes. The parameters that could be extracted are $V_{oc}$, $J_{sc}$, FF, PCE, $V_{mp}$, $J_{mp}$, MPP, $R_s$, $R_{sh,}$ and HI, depending on the availability of scan direction data. The generated reports include I-V and P-V curves, where the lines are color-coded to distinguish between scan directions, including markers to indicate MPP-related parameters. The report also includes tables with PV metrics and summary pages of box plots to visualize the distribution of parameters, enabling researchers to compare the performance of various solar cells.

The software tool was tested on real PSC data, and it proved its ability to provide insightful and well-structured reports, making it an invaluable asset to researchers. While the introduced tool operates effectively within its designed scope, future enhancements of the software could include the extension of the tool to process the 8-pixel data from alternative measurement setups. Moreover, expanding the tool to analyse additional measurements, such as IPCE or operational stability data, would further strengthen its role in PSC research.

## References

Aamir Iqbal, M., Malik, M., Shahid, W., Zaheer Ud Din, S., Anwar, N., Ikram, M., Idrees, F., 2022. Materials for Photovoltaics: Overview, Generations, Recent Advancements and Future Prospects, in: Zaidi, B., Shekhar, C. (Eds.), Thin Films Photovoltaics. IntechOpen. https://doi.org/10.5772/intechopen.101449

Abzieher, T., Moore, D.T., Roß, M., Albrecht, S., Silvia, J., Tan, H., Jeangros, Q., Ballif, C., Hoerantner, M.T., Kim, B.-S., Bolink, H.J., Pistor, P., Goldschmidt, J.C., Chiang, Y.-H., Stranks, S.D., Borchert, J., McGehee, M.D., Morales-Masis, M., Patel, J.B., Bruno, A., Paetzold, U.W., 2024. Vapor phase deposition of perovskite photovoltaics: short track to commercialization? Energy Environ. Sci. 17, 1645–1663. https://doi.org/10.1039/D3EE03273F

Afre, R.A., Pugliese, D., 2024. Perovskite Solar Cells: A Review of the Latest Advances in Materials, Fabrication Techniques, and Stability Enhancement Strategies. Micromachines 15, 192. https://doi.org/10.3390/mi15020192

Afroz, M., Ratnesh, R.K., Srivastava, S., Singh, J., 2025. Perovskite solar cells: Progress, challenges, and future avenues to clean energy. Solar Energy 287, 113205. https://doi.org/10.1016/j.solener.2024.113205

Al-Ashouri, A., Magomedov, A., Roß, M., Jošt, M., Talaikis, M., Chistiakova, G., Bertram, T., Márquez, J.A., Köhnen, E., Kasparavičius, E., Levcenco, S., Gil-Escrig, L., Hages, C.J., Schlatmann, R., Rech, B., Malinauskas, T., Unold, T., Kaufmann, C.A., Korte, L., Niaura, G., Getautis, V., Albrecht, S., 2019. Conformal monolayer contacts with lossless interfaces for perovskite single junction and monolithic tandem solar cells. Energy Environ. Sci. 12, 3356–3369. https://doi.org/10.1039/C9EE02268F

Ali, Sh.S., Mohamed, W.S., Mohamed, H.A., 2025. Effect of series and shunt resistance on the performance of CZTSe thin film solar cell. Sohag Journal of Sciences 10, 75–79. https://doi.org/10.21608/sjsci.2024.335014.1232

Ansari, M.I.H., Qurashi, A., Nazeeruddin, M.K., 2018. Frontiers, opportunities, and challenges in perovskite solar cells: A critical review. Journal of Photochemistry and Photobiology C: Photochemistry Reviews 35, 1–24. https://doi.org/10.1016/j.jphotochemrev.2017.11.002

Augusta Heavens Ikevuje, Jephta Mensah Kwakye, Darlington Eze Ekechukwu, Olorunshogo Benjamin Ogundipe, Andrew Emuobosa Esiri, 2024. Optimizing the energy mix:

Strategies for reducing energy dependence. Open Access Res. J. Multidiscip. Stud. 8, 094–104. https://doi.org/10.53022/oarjms.2024.8.1.0051

Babayigit, A., Ethirajan, A., Muller, M., Conings, B., 2016. Toxicity of organometal halide perovskite solar cells. Nature Mater 15, 247–251. https://doi.org/10.1038/nmat4572

Bae, S.-R., Heo, D.Y., Kim, S.Y., 2022. Recent progress of perovskite devices fabricated using thermal evaporation method: Perspective and outlook. Materials Today Advances 14, 100232. https://doi.org/10.1016/j.mtadv.2022.100232

Baig, H., Kanda, H., Asiri, A.M., Nazeeruddin, M.K., Mallick, T., 2020. Increasing efficiency of perovskite solar cells using low concentrating photovoltaic systems. Sustainable Energy Fuels 4, 528–537. https://doi.org/10.1039/C9SE00550A

Becker, M., Wark, M., 2018. Recent Progress in the Solution-Based Sequential Deposition of Planar Perovskite Solar Cells. Crystal Growth & Design 18, 4790–4806. https://doi.org/10.1021/acs.cgd.8b00686

Best Research-Cell Efficiency Chart [WWW Document], 2025. . National Renewable Energy Laboratory. URL https://www.nrel.gov/pv/cell-efficiency (accessed 6.28.25).

Bhandari, S., Roy, A., Ghosh, A., Mallick, T.K., Sundaram, S., 2020a. Performance of $WO_3$ - Incorporated Carbon Electrodes for Ambient Mesoscopic Perovskite Solar Cells. ACS Omega 5, 422–429. https://doi.org/10.1021/acsomega.9b02934

Bhandari, S., Roy, A., Ghosh, A., Mallick, T.K., Sundaram, S., 2020b. Perceiving the temperature coefficients of carbon-based perovskite solar cells. Sustainable Energy Fuels 4, 6283–6298. https://doi.org/10.1039/D0SE00782J

Brenner, T.M., Egger, D.A., Kronik, L., Hodes, G., Cahen, D., 2016. Hybrid organic—inorganic perovskites: low-cost semiconductors with intriguing charge-transport properties. Nat Rev Mater 1, 15007. https://doi.org/10.1038/natrevmats.2015.7

Bulloch, A., Wang, S., Ghosh, P., Jagadamma, L.K., 2022. Hysteresis in hybrid perovskite indoor photovoltaics. Phil. Trans. R. Soc. A. 380, 20210144. https://doi.org/10.1098/rsta.2021.0144

Chen, M., Ju, M.-G., Garces, H.F., Carl, A.D., Ono, L.K., Hawash, Z., Zhang, Y., Shen, T., Qi, Y., Grimm, R.L., Pacifici, D., Zeng, X.C., Zhou, Y., Padture, N.P., 2019. Highly stable and efficient all-inorganic lead-free perovskite solar cells with native-oxide passivation. Nat Commun 10, 16. https://doi.org/10.1038/s41467-018-07951-y

Clarke, W., Bennett, L.J., Grudeva, Y., Foster, J.M., Richardson, G., Courtier, N.E., 2022. IonMonger 2.0: software for free, fast and versatile simulation of current, voltage and

impedance response of planar perovskite solar cells. J Comput Electron. https://doi.org/10.1007/s10825-022-01988-5

Dave, K., Fang, M.H., Bao, Z., Fu, H.T., Liu, R.S., 2020. Recent Developments in Lead-Free Double Perovskites: Structure, Doping, and Applications. Chemistry An Asian Journal 15, 242–252. https://doi.org/10.1002/asia.201901510

Di Sabatino, M., Hendawi, R., Garcia, A.S., 2024. Silicon Solar Cells: Trends, Manufacturing Challenges, and AI Perspectives. Crystals 14, 167. https://doi.org/10.3390/cryst14020167

Dixit, H., Boro, B., Ghosh, S., Paul, M., Kumar, A., Singh, T., 2022. Assessment of Lead-Free Tin Halide Perovskite Solar Cells Using *J–V* Hysteresis. Physica Status Solidi (a) 219, 2100823. https://doi.org/10.1002/pssa.202100823

Eguchi, N., Fukazawa, T., Kanda, H., Yamamoto, K., Miyake, T., Murakami, T.N., 2025. Performance optimization of perovskite solar cells with an automated spin coating system and artificial intelligence technologies. EES Sol. 10.1039.D5EL00007F. https://doi.org/10.1039/D5EL00007F

Elangovan, N.K., Kannadasan, R., Beenarani, B.B., Alsharif, M.H., Kim, M.-K., Hasan Inamul, Z., 2024. Recent developments in perovskite materials, fabrication techniques, band gap engineering, and the stability of perovskite solar cells. Energy Reports 11, 1171–1190. https://doi.org/10.1016/j.egyr.2023.12.068

El-Mellouhi, F., Marzouk, A., Bentria, E.T., Rashkeev, S.N., Kais, S., Alharbi, F.H., 2016. Hydrogen Bonding and Stability of Hybrid Organic–Inorganic Perovskites. ChemSusChem 9, 2648–2655. https://doi.org/10.1002/cssc.201600864

Ema, K., Umeda, K., Toda, M., Yajima, C., Arai, Y., Kunugita, H., Wolverson, D., Davies, J.J., 2006. Huge exchange energy and fine structure of excitons in an organic-inorganic quantum well material. Phys. Rev. B 73, 241310. https://doi.org/10.1103/PhysRevB.73.241310

Excel specifications and limits [WWW Document], 2025. . Microsoft Support. URL https://support.microsoft.com/en-us/office/excel-specifications-and-limits-1672b34d-7043-467e-8e27-269d656771c3 (accessed 6.28.25).

Fu, H., 2019. Review of lead-free halide perovskites as light-absorbers for photovoltaic applications: From materials to solar cells. Solar Energy Materials and Solar Cells 193, 107–132. https://doi.org/10.1016/j.solmat.2018.12.038

Galve-Lahoz, S., Sánchez-Diaz, J., Echeverría-Arrondo, C., Simancas, J., Rodriguez-Pereira, J., Turren-Cruz, S.-H., Martinez-Pastor, J.P., Mora-Seró, I., Delgado, J.L., 2024.

Addressing ambient stability challenges in pure $FASnI_3$ perovskite solar cells through organic additive engineering. J. Mater. Chem. A 12, 21933–21943. https://doi.org/10.1039/D4TA03291H

Ganose, A.M., Savory, C.N., Scanlon, D.O., 2017. Beyond methylammonium lead iodide: prospects for the emergent field of $ns^2$ containing solar absorbers. Chem. Commun. 53, 20–44. https://doi.org/10.1039/C6CC06475B

Gao, W., Wang, T., Xu, J., Zeng, P., Zhang, W., Yao, Y., Chen, C., Li, M., Yu, S.F., 2021. Robust and Flexible Random Lasers Using Perovskite Quantum Dots Coated Nickel Foam for Speckle-Free Laser Imaging. Small 17, 2103065. https://doi.org/10.1002/smll.202103065

Gerber, G.B., Léonard, A., 1997. Mutagenicity, carcinogenicity and teratogenicity of germanium compounds. Mutation Research/Reviews in Mutation Research 387, 141–146. https://doi.org/10.1016/S1383-5742(97)00034-3

Graham, E., Fulghum, N., Altieri, K., 2025. Global Electricity Review 2025 (Annual Review or Energy Report). Ember.

Habisreutinger, S.N., Noel, N.K., Snaith, H.J., 2018. Hysteresis Index: A Figure without Merit for Quantifying Hysteresis in Perovskite Solar Cells. ACS Energy Lett. 3, 2472–2476. https://doi.org/10.1021/acsenergylett.8b01627

Hamukwaya, S.L., Hao, H., Zhao, Z., Dong, J., Zhong, T., Xing, J., Hao, L., Mashingaidze, M.M., 2022. A Review of Recent Developments in Preparation Methods for Large-Area Perovskite Solar Cells. Coatings 12, 252. https://doi.org/10.3390/coatings12020252

Hanif, M.S., Qasim, I., Malik, M.I., Nasir, M.F., Ahmad, O., Rashid, A., 2024. Development of low-cost and high-efficiency solar modules based on perovskite solar cells for large-scale applications. Heliyon 10, e25703. https://doi.org/10.1016/j.heliyon.2024.e25703

Hasanov, R., 2025. R.U.S.L.A.N PRO. https://doi.org/10.5281/ZENODO.15390040

Hayat, M.B., Ali, D., Monyake, K.C., Alagha, L., Ahmed, N., 2019. Solar energy-A look into power generation, challenges, and a solar-powered future. Int J Energy Res 43, 1049–1067. https://doi.org/10.1002/er.4252

He, D., Chen, P., Steele, J.A., Wang, Z., Xu, Hongyi, Zhang, M., Ding, S., Zhang, C., Lin, T., Kremer, F., Xu, Hongzhe, Hao, M., Wang, L., 2025. Homogeneous 2D/3D heterostructured tin halide perovskite photovoltaics. Nat. Nanotechnol. https://doi.org/10.1038/s41565-025-01905-4

He, H., Yang, Z., Xu, Y., Smith, A.T., Yang, G., Sun, L., 2020. Perovskite oxides as transparent semiconductors: a review. Nano Convergence 7, 32. https://doi.org/10.1186/s40580-020-00242-7

Hu, M., Bi, C., Yuan, Y., Bai, Y., Huang, J., 2016. Stabilized Wide Bandgap $MAPbBr_xI_{3-x}$ Perovskite by Enhanced Grain Size and Improved Crystallinity. Advanced Science 3, 1500301. https://doi.org/10.1002/advs.201500301

Huang, J.-Y., Yang, Y.-W., Hsu, W.-H., Chang, E.-W., Chen, M.-H., Wu, Y.-R., 2022. Influences of dielectric constant and scan rate on hysteresis effect in perovskite solar cell with simulation and experimental analyses. Sci Rep 12. https://doi.org/10.1038/s41598-022-11899-x

Hussain, I., Tran, H.P., Jaksik, J., Moore, J., Islam, N., Uddin, M.J., 2018. Functional materials, device architecture, and flexibility of perovskite solar cell. emergent mater. 1, 133–154. https://doi.org/10.1007/s42247-018-0013-1

International Energy Agency, 2023. Finland 2023 Energy Policy Review, IEA Energy Policy Reviews. OECD. https://doi.org/10.1787/d435fa51-en

Jacobs, D.A., Wu, Y., Shen, H., Barugkin, C., Beck, F.J., White, T.P., Weber, K., Catchpole, K.R., 2017. Hysteresis phenomena in perovskite solar cells: the many and varied effects of ionic accumulation. Phys. Chem. Chem. Phys. 19, 3094–3103. https://doi.org/10.1039/c6cp06989d

Jacobsson, T.J., Hultqvist, A., García-Fernández, A., Anand, A., Al-Ashouri, A., Hagfeldt, A., Crovetto, A., Abate, A., Ricciardulli, A.G., Vijayan, A., Kulkarni, A., Anderson, A.Y., Darwich, B.P., Yang, B., Coles, B.L., Perini, C.A.R., Rehermann, C., Ramirez, D., Fairen-Jimenez, D., Di Girolamo, D., Jia, D., Avila, E., Juarez-Perez, E.J., Baumann, F., Mathies, F., González, G.S.A., Boschloo, G., Nasti, G., Paramasivam, G., Martínez-Denegri, G., Näsström, H., Michaels, H., Köbler, H., Wu, H., Benesperi, I., Dar, M.I., Bayrak Pehlivan, I., Gould, I.E., Vagott, J.N., Dagar, J., Kettle, J., Yang, J., Li, J., Smith, J.A., Pascual, J., Jerónimo-Rendón, J.J., Montoya, J.F., Correa-Baena, J.-P., Qiu, J., Wang, J., Sveinbjörnsson, K., Hirselandt, K., Dey, K., Frohna, K., Mathies, L., Castriotta, L.A., Aldamasy, Mahmoud.H., Vasquez-Montoya, M., Ruiz-Preciado, M.A., Flatken, M.A., Khenkin, M.V., Grischek, M., Kedia, M., Saliba, M., Anaya, M., Veldhoen, M., Arora, N., Shargaieva, O., Maus, O., Game, O.S., Yudilevich, O., Fassl, P., Zhou, Q., Betancur, R., Munir, R., Patidar, R., Stranks, S.D., Alam, S., Kar, S., Unold, T., Abzieher, T., Edvinsson, T., David, T.W., Paetzold, U.W., Zia, W., Fu, W., Zuo, W., Schröder, V.R.F., Tress, W., Zhang, X., Chiang, Y.-H., Iqbal, Z., Xie, Z.,

Unger, E., 2021. An open-access database and analysis tool for perovskite solar cells based on the FAIR data principles. Nat Energy 7, 107–115. https://doi.org/10.1038/s41560-021-00941-3

Jena, A.K., Kulkarni, A., Miyasaka, T., 2019. Halide Perovskite Photovoltaics: Background, Status, and Future Prospects. Chem. Rev. 119, 3036–3103. https://doi.org/10.1021/acs.chemrev.8b00539

Jeng, J., Chiang, Y., Lee, M., Peng, S., Guo, T., Chen, P., Wen, T., 2013. $CH_3 NH_3 PbI_3$ Perovskite/Fullerene Planar-Heterojunction Hybrid Solar Cells. Advanced Materials 25, 3727–3732. https://doi.org/10.1002/adma.201301327

Kant, N., Singh, P., 2022. Review of next generation photovoltaic solar cell technology and comparative materialistic development. Materials Today: Proceedings 56, 3460–3470. https://doi.org/10.1016/j.matpr.2021.11.116

Katz, E.A., 2020. Perovskite: Name Puzzle and German-Russian Odyssey of Discovery. Helvetica Chimica Acta 103, e2000061. https://doi.org/10.1002/hlca.202000061

Khalfin, S., Bekenstein, Y., 2019. Advances in lead-free double perovskite nanocrystals, engineering band-gaps and enhancing stability through composition tunability. Nanoscale 11, 8665–8679. https://doi.org/10.1039/C9NR01031A

Khenkin, M.V., Katz, E.A., Abate, A., Bardizza, G., Berry, J.J., Brabec, C., Brunetti, F., Bulović, V., Burlingame, Q., Di Carlo, A., Cheacharoen, R., Cheng, Y.-B., Colsmann, A., Cros, S., Domanski, K., Dusza, M., Fell, C.J., Forrest, S.R., Galagan, Y., Di Girolamo, D., Grätzel, M., Hagfeldt, A., Von Hauff, E., Hoppe, H., Kettle, J., Köbler, H., Leite, M.S., Liu, S., Loo, Y.-L., Luther, J.M., Ma, C.-Q., Madsen, M., Manceau, M., Matheron, M., McGehee, M., Meitzner, R., Nazeeruddin, M.K., Nogueira, A.F., Odabaşı, Ç., Osherov, A., Park, N.-G., Reese, M.O., De Rossi, F., Saliba, M., Schubert, U.S., Snaith, H.J., Stranks, S.D., Tress, W., Troshin, P.A., Turkovic, V., Veenstra, S., Visoly-Fisher, I., Walsh, A., Watson, T., Xie, H., Yıldırım, R., Zakeeruddin, S.M., Zhu, K., Lira-Cantu, M., 2020. Consensus statement for stability assessment and reporting for perovskite photovoltaics based on ISOS procedures. Nat Energy 5, 35–49. https://doi.org/10.1038/s41560-019-0529-5

Khunchan, S., Wiengmoon, B., 2018. Method to determine the single curve IV characteristic parameter of solar cell. J. Phys.: Conf. Ser. 1144, 012012. https://doi.org/10.1088/1742-6596/1144/1/012012

Kim, G., Kim, K., Kim, H.J., Jung, H.S., Jeon, I., Lee, J., 2023. Sustainable and environmentally viable perovskite solar cells. EcoMat 5, e12319. https://doi.org/10.1002/eom2.12319

Kim, Y., Yang, Z., Jain, A., Voznyy, O., Kim, G., Liu, M., Quan, L.N., García de Arquer, F.P., Comin, R., Fan, J.Z., Sargent, E.H., 2016. Pure Cubic-Phase Hybrid Iodobismuthates $AgBi_2 I_7$ for Thin-Film Photovoltaics. Angewandte Chemie 128, 9738–9742. https://doi.org/10.1002/ange.201603608

Kim, Y.C., Yang, T.-Y., Jeon, N.J., Im, J., Jang, S., Shin, T.J., Shin, H.-W., Kim, S., Lee, E., Kim, S., Noh, J.H., Seok, S.I., Seo, J., 2017. Engineering interface structures between lead halide perovskite and copper phthalocyanine for efficient and stable perovskite solar cells. Energy Environ. Sci. 10, 2109–2116. https://doi.org/10.1039/c7ee01931a

Kojima, A., Teshima, K., Shirai, Y., Miyasaka, T., 2009. Organometal Halide Perovskites as Visible-Light Sensitizers for Photovoltaic Cells. J. Am. Chem. Soc. 131, 6050–6051. https://doi.org/10.1021/ja809598r

Kong, J., Wang, H., Röhr, J.A., Fishman, Z.S., Zhou, Y., Li, M., Cotlet, M., Kim, G., Karpovich, C., Antonio, F., Padture, N.P., Taylor, A.D., 2020. Perovskite Solar Cells with Enhanced Fill Factors Using Polymer-Capped Solvent Annealing. ACS Appl. Energy Mater. 3, 7231–7238. https://doi.org/10.1021/acsaem.0c00854

Konstantakou, M., Stergiopoulos, T., 2017. A critical review on tin halide perovskite solar cells. J. Mater. Chem. A 5, 11518–11549. https://doi.org/10.1039/C7TA00929A

Kopacic, I., Friesenbichler, B., Hoefler, S.F., Kunert, B., Plank, H., Rath, T., Trimmel, G., 2018. Enhanced Performance of Germanium Halide Perovskite Solar Cells through Compositional Engineering. ACS Appl. Energy Mater. 1, 343–347. https://doi.org/10.1021/acsaem.8b00007

Kosasih, F.U., Erdenebileg, E., Mathews, N., Mhaisalkar, S.G., Bruno, A., 2022. Thermal evaporation and hybrid deposition of perovskite solar cells and mini-modules. Joule 6, 2692–2734. https://doi.org/10.1016/j.joule.2022.11.004

Kulovesi, K., Oberthür, S., 2020. Assessing the EU's 2030 Climate and Energy Policy Framework: Incremental change toward radical transformation? Rev Euro Comp Intl Enviro 29, 151–166. https://doi.org/10.1111/reel.12358

Kumar, R., Rajoria, C.S., Sharma, A., Suhag, S., 2021. Design and simulation of standalone solar PV system using PVsyst Software: A case study. Materials Today: Proceedings 46, 5322–5328. https://doi.org/10.1016/j.matpr.2020.08.785

Lambert, J.R., 1991. Pharmacology of Bismuth-Containing Compounds. Clinical Infectious Diseases 13, S691–S695. https://doi.org/10.1093/clinids/13.Supplement_8.S691

Lavagna, L., Syrrokostas, G., Fagiolari, L., Amici, J., Francia, C., Bodoardo, S., Leftheriotis, G., Bella, F., 2021. Platinum-free photoelectrochromic devices working with copper-based electrolytes for ultrastable smart windows. J. Mater. Chem. A 9, 19687–19691. https://doi.org/10.1039/D1TA03544D

Lee, M.M., Teuscher, J., Miyasaka, T., Murakami, T.N., Snaith, H.J., 2012. Efficient Hybrid Solar Cells Based on Meso-Superstructured Organometal Halide Perovskites. Science 338, 643–647. https://doi.org/10.1126/science.1228604

Li, H., Li, F., Shen, Z., Han, S.-T., Chen, J., Dong, C., Chen, C., Zhou, Y., Wang, M., 2021. Photoferroelectric perovskite solar cells: Principles, advances and insights. Nano Today 37, 101062. https://doi.org/10.1016/j.nantod.2020.101062

Li, H., Zuo, C., Scully, A.D., Angmo, D., Yang, J., Gao, M., 2020. Recent progress towards roll-to-roll manufacturing of perovskite solar cells using slot-die processing. Flex. Print. Electron. 5, 014006. https://doi.org/10.1088/2058-8585/ab639e

Li, N., Niu, X., Chen, Q., Zhou, H., 2020. Towards commercialization: the operational stability of perovskite solar cells. Chem. Soc. Rev. 49, 8235–8286. https://doi.org/10.1039/D0CS00573H

Lin, H., Yang, M., Ru, X., Wang, G., Yin, S., Peng, F., Hong, C., Qu, M., Lu, J., Fang, L., Han, C., Procel, P., Isabella, O., Gao, P., Li, Z., Xu, X., 2023. Silicon heterojunction solar cells with up to 26.81% efficiency achieved by electrically optimized nanocrystalline-silicon hole contact layers. Nat Energy 8, 789–799. https://doi.org/10.1038/s41560-023-01255-2

Liu, M., Johnston, M.B., Snaith, H.J., 2013. Efficient planar heterojunction perovskite solar cells by vapour deposition. Nature 501, 395–398. https://doi.org/10.1038/nature12509

Liu, P., Wang, W., Liu, S., Yang, H., Shao, Z., 2019. Fundamental Understanding of Photocurrent Hysteresis in Perovskite Solar Cells. Advanced Energy Materials 9, 1803017. https://doi.org/10.1002/aenm.201803017

Liu, X., Wu, T., Chen, J.-Y., Meng, X., He, X., Noda, T., Chen, H., Yang, X., Segawa, H., Wang, Y., Han, L., 2020. Templated growth of $FASnI_3$ crystals for efficient tin perovskite solar cells. Energy Environ. Sci. 13, 2896–2902. https://doi.org/10.1039/D0EE01845G

Liu, Z., Liu, P., Li, M., He, T., Liu, T., Yu, L., Yuan, M., 2022. Efficient and Stable FA-Rich Perovskite Photovoltaics: From Material Properties to Device Optimization. Advanced Energy Materials 12, 2200111. https://doi.org/10.1002/aenm.202200111

Magdalin, A.E., Nixon, P.D., Jayaseelan, E., Sivakumar, M., Devi, S.K.N., Subathra, M.S.P., Kumar, N.M., Ananthi, N., 2023. Development of lead-free perovskite solar cells: Opportunities, challenges, and future technologies. Results in Engineering 20, 101438. https://doi.org/10.1016/j.rineng.2023.101438

Marimuthu, T., Yuvakkumar, R., Kumar, P.S., Vo, D.-V.N., Xu, X., Xu, G., 2022. Two-dimensional hybrid perovskite solar cells: a review. Environ Chem Lett 20, 189–210. https://doi.org/10.1007/s10311-021-01306-8

Martins, F., Felgueiras, C., Smitkova, M., Caetano, N., 2019. Analysis of Fossil Fuel Energy Consumption and Environmental Impacts in European Countries. Energies 12, 964. https://doi.org/10.3390/en12060964

Miah, Md.H., Khandaker, M.U., Rahman, Md.B., Nur-E-Alam, M., Islam, M.A., 2024. Band gap tuning of perovskite solar cells for enhancing the efficiency and stability: issues and prospects. RSC Adv. 14, 15876–15906. https://doi.org/10.1039/D4RA01640H

Minbashi, M., Yazdani, E., 2022. Comprehensive study of anomalous hysteresis behavior in perovskite-based solar cells. Sci Rep 12. https://doi.org/10.1038/s41598-022-19194-5

Minemoto, T., Murata, M., 2015. Theoretical analysis on effect of band offsets in perovskite solar cells. Solar Energy Materials and Solar Cells 133, 8–14. https://doi.org/10.1016/j.solmat.2014.10.036

Mirseraji, M., Shahraki, M.G., 2018. DFT study of the polarization behaviors of various distorted barium titanate crystals: The role of atomic displacements. Physica B: Condensed Matter 538, 120–130. https://doi.org/10.1016/j.physb.2018.03.032

Mishra, P.R., Rathore, S., Jain, V., 2024. PVSyst enabled real time evaluation of grid connected solar photovoltaic system. Int. j. inf. tecnol. 16, 745–752. https://doi.org/10.1007/s41870-023-01677-x

Miyasaka, T., 2015. Perovskite Photovoltaics: Rare Functions of Organo Lead Halide in Solar Cells and Optoelectronic Devices. Chemistry Letters 44, 720–729. https://doi.org/10.1246/cl.150175

Miyata, A., Mitioglu, A., Plochocka, P., Portugall, O., Wang, J.T.-W., Stranks, S.D., Snaith, H.J., Nicholas, R.J., 2015. Direct measurement of the exciton binding energy and effective masses for charge carriers in organic–inorganic tri-halide perovskites. Nature Phys 11, 582–587. https://doi.org/10.1038/nphys3357

Momblona, C., Gil-Escrig, L., Bandiello, E., Hutter, E.M., Sessolo, M., Lederer, K., Blochwitz-Nimoth, J., Bolink, H.J., 2016. Efficient vacuum deposited p-i-n and n-i-p perovskite solar cells employing doped charge transport layers. Energy Environ. Sci. 9, 3456–3463. https://doi.org/10.1039/C6EE02100J

Montes-Romero, J., Torres-Ramírez, M., De la Casa, J., Firman, A., Cáceres, M., 2016. Software tool for the extrapolation to Standard Test Conditions (STC) from experimental curves of photovoltaic modules, in: 2016 Technologies Applied to Electronics Teaching (TAEE). IEEE, pp. 1–7.

Morales-Aragonés, J.I., Alonso-García, M.D.C., Gallardo-Saavedra, S., Alonso-Gómez, V., Balenzategui, J.L., Redondo-Plaza, A., Hernández-Callejo, L., 2021. Online Distributed Measurement of Dark I-V Curves in Photovoltaic Plants. Applied Sciences 11, 1924. https://doi.org/10.3390/app11041924

Niu, G., Li, W., Meng, F., Wang, L., Dong, H., Qiu, Y., 2014. Study on the stability of $CH_3NH_3PbI_3$ films and the effect of post-modification by aluminum oxide in all-solid-state hybrid solar cells. J. Mater. Chem. A 2, 705–710. https://doi.org/10.1039/C3TA13606J

Nur-E-Alam, M., Islam, M.S., Abedin, T., Islam, M.A., Yap, B.K., Kiong, T.S., Das, N., Rahman, M.R., Khandaker, M.U., 2025. Current scenario and future trends on stability issues of perovskite solar cells: A mini review. Current Opinion in Colloid & Interface Science 76, 101895. https://doi.org/10.1016/j.cocis.2025.101895

Pan, J., Chen, Z., Zhang, T., Hu, B., Ning, H., Meng, Z., Su, Z., Nodari, D., Xu, W., Min, G., Chen, M., Liu, X., Gasparini, N., Haque, S.A., Barnes, P.R.F., Gao, F., Bakulin, A.A., 2023. Operando dynamics of trapped carriers in perovskite solar cells observed via infrared optical activation spectroscopy. Nat Commun 14, 8000. https://doi.org/10.1038/s41467-023-43852-5

Park, N.-G., 2018. Halide perovskite photovoltaics: History, progress, and perspectives. MRS Bull. 43, 527–533. https://doi.org/10.1557/mrs.2018.152

Park, N.-G., 2015. Perovskite solar cells: an emerging photovoltaic technology. Materials Today 18, 65–72. https://doi.org/10.1016/j.mattod.2014.07.007

Raj, A., Kumar, M., Anshul, A., 2021. Recent advancement in inorganic-organic electron transport layers in perovskite solar cell: current status and future outlook. Materials Today Chemistry 22, 100595. https://doi.org/10.1016/j.mtchem.2021.100595

Ran, C., Wu, Z., Xi, J., Yuan, F., Dong, H., Lei, T., He, X., Hou, X., 2017. Construction of Compact Methylammonium Bismuth Iodide Film Promoting Lead-Free Inverted

Planar Heterojunction Organohalide Solar Cells with Open-Circuit Voltage over 0.8 V. J. Phys. Chem. Lett. 8, 394–400. https://doi.org/10.1021/acs.jpclett.6b02578

Riordan, C., Hulstron, R., 1990. What is an air mass 1.5 spectrum?(solar cell performance calculations), in: IEEE Conference on Photovoltaic Specialists. IEEE, pp. 1085–1088.

Rong, Y., Hu, Y., Ravishankar, S., Liu, H., Hou, X., Sheng, Y., Mei, A., Wang, Q., Li, D., Xu, M., Bisquert, J., Han, H., 2017. Tunable hysteresis effect for perovskite solar cells. Energy Environ. Sci. 10, 2383–2391. https://doi.org/10.1039/c7ee02048a

Roy, P., Ghosh, A., Barclay, F., Khare, A., Cuce, E., 2022a. Perovskite Solar Cells: A Review of the Recent Advances. Coatings 12, 1089. https://doi.org/10.3390/coatings12081089

Roy, P., Khare, A., 2022. Understanding the strategies to attain the best performance of all inorganic lead-free perovskite solar cells: Theoretical insights. Intl J of Energy Research 46, 15881–15899. https://doi.org/10.1002/er.8287

Roy, P., Raoui, Y., Khare, A., 2022b. Design and simulation of efficient tin based perovskite solar cells through optimization of selective layers: Theoretical insights. Optical Materials 125, 112057. https://doi.org/10.1016/j.optmat.2022.112057

Saha-Dasgupta, T., 2020. Double perovskites with 3d and 4d/5d transition metals: compounds with promises. Mater. Res. Express 7, 014003. https://doi.org/10.1088/2053-1591/ab6293

Schileo, G., Grancini, G., 2021. Lead or no lead? Availability, toxicity, sustainability and environmental impact of lead-free perovskite solar cells. J. Mater. Chem. C 9, 67–76. https://doi.org/10.1039/D0TC04552G

Setfos: Simulation Software for OLEDs and Perovskite Solar Cells [WWW Document], 2025. . Fluxim. URL https://www.fluxim.com/setfos-intro (accessed 6.29.25).

Sha, H., Han, J., Wang, F., Huang, W., Ma, X., Jia, C., Chen, Y., 2023. Probing carrier trapping and hysteresis at perovskite grain boundaries via in situ characterization. Optical Materials 139, 113817. https://doi.org/10.1016/j.optmat.2023.113817

Shah, N., Shah, A.A., Leung, P.K., Khan, S., Sun, K., Zhu, X., Liao, Q., 2023. A Review of Third Generation Solar Cells. Processes 11, 1852. https://doi.org/10.3390/pr11061852

Shi, Y., Zhu, Z., Miao, D., Ding, Y., Mi, Q., 2024. Interfacial Dipoles Boost Open-Circuit Voltage of Tin Halide Perovskite Solar Cells. ACS Energy Lett. 9, 1895–1897. https://doi.org/10.1021/acsenergylett.4c00529

Shtangeeva, I., Bali, R., Harris, A., 2011. Bioavailability and toxicity of antimony. Journal of Geochemical Exploration 110, 40–45. https://doi.org/10.1016/j.gexplo.2010.07.003

Singh, P., Ravindra, N.M., 2012. Analysis of series and shunt resistance in silicon solar cells using single and double exponential models. Emerging Materials Research 1, 33–38. https://doi.org/10.1680/emr.11.00008

Singh, R., Parashar, M., 2020. Origin of Hysteresis in Perovskite Solar Cells, in: Ren, J., Kan, Z. (Eds.), Soft-Matter Thin Film Solar Cells. AIP Publishing LLCMelville, New York, pp. 1-1-1–42. https://doi.org/10.1063/9780735422414_001

Song, T.-B., Yokoyama, T., Aramaki, S., Kanatzidis, M.G., 2017. Performance Enhancement of Lead-Free Tin-Based Perovskite Solar Cells with Reducing Atmosphere-Assisted Dispersible Additive. ACS Energy Lett. 2, 897–903. https://doi.org/10.1021/acsenergylett.7b00171

Starkholm, A., Kloo, L., Svensson, P.H., 2023. Accelerated Discovery of Perovskite-Inspired Materials through Robotized Screening Including Solar Cell Characterization. ACS Appl. Energy Mater. 6, 12022–12031. https://doi.org/10.1021/acsaem.3c02242

Stolterfoht, M., Caprioglio, P., Wolff, C.M., Márquez, J.A., Nordmann, J., Zhang, S., Rothhardt, D., Hörmann, U., Amir, Y., Redinger, A., Kegelmann, L., Zu, F., Albrecht, S., Koch, N., Kirchartz, T., Saliba, M., Unold, T., Neher, D., 2019. The impact of energy alignment and interfacial recombination on the internal and external open-circuit voltage of perovskite solar cells. Energy Environ. Sci. 12, 2778–2788. https://doi.org/10.1039/C9EE02020A

Sun, P.-P., Li, Q.-S., Yang, L.-N., Li, Z.-S., 2016. Theoretical insights into a potential lead-free hybrid perovskite: substituting $Pb^{2+}$ with $Ge^{2+}$. Nanoscale 8, 1503–1512. https://doi.org/10.1039/C5NR05337D

Sun, S., Tiihonen, A., Oviedo, F., Liu, Z., Thapa, J., Zhao, Y., Hartono, N.T.P., Goyal, A., Heumueller, T., Batali, C., Encinas, A., Yoo, J.J., Li, R., Ren, Z., Peters, I.M., Brabec, C.J., Bawendi, M.G., Stevanovic, V., Fisher, J., Buonassisi, T., 2021. A data fusion approach to optimize compositional stability of halide perovskites. Matter 4, 1305–1322. https://doi.org/10.1016/j.matt.2021.01.008

Surmiak, M.A., Zhang, T., Lu, J., Rietwyk, K.J., Raga, S.R., McMeekin, D.P., Bach, U., 2020. High-Throughput Characterization of Perovskite Solar Cells for Rapid Combinatorial Screening. Solar RRL 4, 2000097. https://doi.org/10.1002/solr.202000097

Sze, S.M., Ng, K.K., 2006. Physics of Semiconductor Devices, 1st ed. Wiley. https://doi.org/10.1002/0470068329

Tong, J., Jiang, Q., Zhang, F., Kang, S.B., Kim, D.H., Zhu, K., 2021. Wide-Bandgap Metal Halide Perovskites for Tandem Solar Cells. ACS Energy Lett. 6, 232–248. https://doi.org/10.1021/acsenergylett.0c02105

Unger, E.L., Kegelmann, L., Suchan, K., Sörell, D., Korte, L., Albrecht, S., 2017. Roadmap and roadblocks for the band gap tunability of metal halide perovskites. J. Mater. Chem. A 5, 11401–11409. https://doi.org/10.1039/C7TA00404D

Valadi, K., Gharibi, S., Taheri-Ledari, R., Akin, S., Maleki, A., Shalan, A.E., 2021. Metal oxide electron transport materials for perovskite solar cells: a review. Environ Chem Lett 19, 2185–2207. https://doi.org/10.1007/s10311-020-01171-x

Veurman, W., Kern, J., Pflüger, L., Wagner-Mohnsen, H., Müller, M., Altermatt, P.P., Lou, Z., Stolterfoht, M., Haase, F., Kajari-Schröder, S., Peibst, R., 2024. Deciphering hysteresis in perovskite solar cells: Insights from device simulations distinguishing shallow traps from mobile ions. Solar Energy 284, 113037. https://doi.org/10.1016/j.solener.2024.113037

Victoria, M., Haegel, N., Peters, I.M., Sinton, R., Jäger-Waldau, A., Del Cañizo, C., Breyer, C., Stocks, M., Blakers, A., Kaizuka, I., Komoto, K., Smets, A., 2021. Solar photovoltaics is ready to power a sustainable future. Joule 5, 1041–1056. https://doi.org/10.1016/j.joule.2021.03.005

Vidani, A.C., 2025. Parallel JV and stability measurement platform for organic and perovskite solar cells — Fluxim [WWW Document]. URL https://www.fluxim.com/litos-lite (accessed 5.8.25).

Volonakis, G., Giustino, F., 2018. Surface properties of lead-free halide double perovskites: Possible visible-light photo-catalysts for water splitting. Applied Physics Letters 112, 243901. https://doi.org/10.1063/1.5035274

Wali, Q., Aamir, M., Ullah, A., Iftikhar, F.J., Khan, M.E., Akhtar, J., Yang, S., 2022. Fundamentals of Hysteresis in Perovskite Solar Cells: From Structure-Property Relationship to Neoteric Breakthroughs. The Chemical Record 22, e202100150. https://doi.org/10.1002/tcr.202100150

Wang, J., 2022. Open-circuit voltage, fill factor, and heterojunction band offset in semiconductor diode solar cells. EcoMat 4, e12263. https://doi.org/10.1002/eom2.12263

Wang, M., Wang, W., Ma, B., Shen, W., Liu, L., Cao, K., Chen, S., Huang, W., 2021. Lead-Free Perovskite Materials for Solar Cells. Nano-Micro Lett. 13, 62. https://doi.org/10.1007/s40820-020-00578-z

Wang, X., Yang, J., Zhong, J., Yu, J., Pan, X., 2024. Innovative Materials for High-Performance Tin-Based Perovskite Solar Cells: A Review. Polymers 16, 3053. https://doi.org/10.3390/polym16213053

Wang, X., Zhang, T., Lou, Y., Zhao, Y., 2019. All-inorganic lead-free perovskites for optoelectronic applications. Mater. Chem. Front. 3, 365–375. https://doi.org/10.1039/C8QM00611C

Wani, A.L., Ara, A., Usmani, J.A., 2015. Lead toxicity: a review. Interdisciplinary Toxicology 8, 55–64. https://doi.org/10.1515/intox-2015-0009

Warby, J., Zu, F., Zeiske, S., Gutierrez-Partida, E., Frohloff, L., Kahmann, S., Frohna, K., Mosconi, E., Radicchi, E., Lang, F., Shah, S., Peña-Camargo, F., Hempel, H., Unold, T., Koch, N., Armin, A., De Angelis, F., Stranks, S.D., Neher, D., Stolterfoht, M., 2022. Understanding Performance Limiting Interfacial Recombination in *pin* Perovskite Solar Cells. Advanced Energy Materials 12, 2103567. https://doi.org/10.1002/aenm.202103567

Will Holmgren, Kevin Anderson, Cliff Hansen, robwandrews, Adam R. Jensen, Mark Mikofski, RDaxini, Antonio Lorenzo, Echedey Luis, Uwe Krien, bmu, Anton Driesse, Cameron Stark, DaCoEx, Miguel Sánchez de León Peque, Taos Transue, Ioannis Sifnaios, kt, Kurt Rhee, Naman Priyadarshi, mayudong, Leland Boeman, Veronica Guo, Marc A. Anoma, Ed Miller, Heliolytics, Joshua Stein, Saurabh Aneja, Bernat Nicolau, Will Vining, 2025. pvlib/pvlib-python: v0.12.1-alpha.1. https://doi.org/10.5281/ZENODO.593284

Wong, J.H., Royapoor, M., Chan, C.W., 2016. Review of life cycle analyses and embodied energy requirements of single-crystalline and multi-crystalline silicon photovoltaic systems. Renewable and Sustainable Energy Reviews 58, 608–618. https://doi.org/10.1016/j.rser.2015.12.241

Wu, T., Liu, X., Luo, X., Lin, X., Cui, D., Wang, Y., Segawa, H., Zhang, Y., Han, L., 2021a. Lead-free tin perovskite solar cells. Joule 5, 863–886. https://doi.org/10.1016/j.joule.2021.03.001

Wu, T., Qin, Z., Wang, Y., Wu, Y., Chen, W., Zhang, S., Cai, M., Dai, S., Zhang, J., Liu, J., Zhou, Z., Liu, X., Segawa, H., Tan, H., Tang, Q., Fang, J., Li, Y., Ding, L., Ning, Z., Qi, Y., Zhang, Y., Han, L., 2021b. The Main Progress of Perovskite Solar Cells in 2020–2021. Nano-Micro Lett. 13, 152. https://doi.org/10.1007/s40820-021-00672-w

Xie, G., Xu, L., Sun, L., Xiong, Y., Wu, P., Hu, B., 2019. Insight into the reaction mechanism of water, oxygen and nitrogen molecules on a tin iodine perovskite surface. J. Mater. Chem. A 7, 5779–5793. https://doi.org/10.1039/C8TA11705E

Xu, C., Yao, Y., Wang, G., Dong, J., Xu, G., Zhong, Y., Lu, D., Zhao, X., Liu, D., Zhou, G., Yang, X., Li, P., Chen, L., Song, Q., 2022. Self-woven monolayer polyionic mesh to achieve highly efficient and stable inverted perovskite solar cells. Chemical Engineering Journal 428, 132074. https://doi.org/10.1016/j.cej.2021.132074

Xu, Y., Wang, J., Sun, L., Huang, Heng, Han, J., Huang, He, Zhai, L., Zou, C., 2021. Top transparent electrodes for fabricating semitransparent organic and perovskite solar cells. J. Mater. Chem. C 9, 9102–9123. https://doi.org/10.1039/D1TC02413B

Yang, C., Shan, X., Xie, T., 2020. Insights of Hysteresis Behaviors in Perovskite Solar Cells from a Mixed Drift-Diffusion Model Coupled with Recombination. Photonics 7, 47. https://doi.org/10.3390/photonics7030047

Yang, D., Zhang, G., Lai, R., Cheng, Y., Lian, Y., Rao, M., Huo, D., Lan, D., Zhao, B., Di, D., 2021. Germanium-lead perovskite light-emitting diodes. Nat Commun 12, 4295. https://doi.org/10.1038/s41467-021-24616-5

Yao, H., Zhou, F., Li, Z., Ci, Z., Ding, L., Jin, Z., 2020. Strategies for Improving the Stability of Tin-Based Perovskite ($ASnX_3$ ) Solar Cells. Advanced Science 7, 1903540. https://doi.org/10.1002/advs.201903540

You, P., Tang, G., Yan, F., 2019. Two-dimensional materials in perovskite solar cells. Materials Today Energy 11, 128–158. https://doi.org/10.1016/j.mtener.2018.11.006

Zeevy, R., Burmistrov, I., 2023. Perovskite Miner.

Zhan, X., Chen, X., Li, C., Jin, T., Wang, Y., Chen, Z.-N., Wu, T., Chen, J., Zhuang, W., 2023. Can Lead-Free Double Halide Perovskites Serve as Proper Photovoltaic Absorber? J. Phys. Chem. Lett. 14, 10784–10793. https://doi.org/10.1021/acs.jpclett.3c02663

Zhang, H., Park, N.-G., 2024a. Progress and issues in p-i-n type perovskite solar cells. DeCarbon 3, 100025. https://doi.org/10.1016/j.decarb.2023.100025

Zhang, H., Park, N.-G., 2024b. Progress and issues in p-i-n type perovskite solar cells. DeCarbon 3, 100025. https://doi.org/10.1016/j.decarb.2023.100025

Zhang, Q., Hao, F., Li, J., Zhou, Y., Wei, Y., Lin, H., 2018. Perovskite solar cells: must lead be replaced – and can it be done? Science and Technology of Advanced Materials 19, 425–442. https://doi.org/10.1080/14686996.2018.1460176

Zhang, Y., Ma, Y., Wang, Y., Zhang, X., Zuo, C., Shen, L., Ding, L., 2021. Lead-Free Perovskite Photodetectors: Progress, Challenges, and Opportunities. Advanced Materials 33, 2006691. https://doi.org/10.1002/adma.202006691

Zhang, Y.-Y., Chen, S., Xu, P., Xiang, H., Gong, X.-G., Walsh, A., Wei, S.-H., 2018. Intrinsic Instability of the Hybrid Halide Perovskite Semiconductor $CH_3 NH_3 PbI_3$*. Chinese Phys. Lett. 35, 036104. https://doi.org/10.1088/0256-307X/35/3/036104

Zhao, W., Lin, D., Guo, P., Jia, N., Wu, J., Ye, Q., Yan, F., Wang, H., 2025. Omnibearing Molecular-Locking of Perovskite Lattice Enables High-Performance Perovskite Solar Cells with Efficiency over 26%. Adv Funct Materials 35, 2423096. https://doi.org/10.1002/adfm.202423096